Nonlinear Kalman Filtering Based Damage Quantification for Civil Infrastructure

By

Esmaeil Ghorbani

A thesis submitted to the Faculty of Graduate Studies of
The University of Manitoba
in partial fulfilment of the requirements of the degree of

DOCTOR OF PHILOSOPHY

Department of Civil Engineering
University of Manitoba
Winnipeg, Manitoba, Canada

Abstract

Despite advancements in Kalman filtering and the dozens of published works on the subject, the performance of Kalman filtering in terms of structural damage quantification is limited to structural systems with low dimension state vectors. Furthermore, Kalman filters cannot accurately identify damage in structures with unknown excitations. Therefore, This dissertation introduced two methods to overcome these fundamental limitations.

The first method is called the iterated modified cubature unscented Kalman filter (IMUKF). It is developed by a careful combination of sigma points deriving from the unscented Kalman filter (UKF) and cubature points from the Cubature Kalman filter (CKF) and adding iterative convergence criterion to the algorithm. Extensive numerical analysis reveals that the IMUKF outperforms the traditional nonlinear Kalman filtering by increasing the number of unknown parameters.

The second method eliminates the uncertainties related to the unknown excitations by extracting the free vibration response of the underlying structure. This idea introduces an output-only damage quantification method. The free vibration response is fed into the UKF, which estimates the unknown states without any need to input information for damage quantification. This proposed output-only method, referred to as RD-UKF, is evaluated using numerical and full-scale experimental data.

Bridge scour is a leading cause of catastrophic bridge failures in North America. In order to accurately estimate the level of scour, a new numerical model for a bridge pier is derived based on the Euler beam theory. The new model is able to simultaneously consider soil-structure interaction, bridge bearings, deck mass, water force, and traffic loading. The model is then integrated with the proposed RD-UKF method for bridge scour quantification. In addition to the numerical simulation studies, the method is implemented on a real bridge in the province of Manitoba, Canada. The estimated soil height is verified with two different independent bathymetries in two different seasons.

Results of the numerical and experimental investigations indicated that eliminating input excitation from the measured response decreases the uncertainty in the estimation

process. Furthermore, it shows that the introduced RD-UKF method can be used for damage quantification in different structures without any information about the input excitation.

Co-authorship

This thesis has been prepared in accordance with the regulations for integrated-article format stipulated by the Faculty of Graduate Studies at the University of Manitoba. Substantial parts of this thesis were published or submitted to peer-reviewed technical journals for publication. The candidate's contribution to each paper are mentioned as below:

1) **E. Ghorbani** and Y. J. Cha, "*Iterated cubature unscented Kalman filter for large-DoF systems identification with noisy data*," Journal of Sound and Vibration, 420, 21-34, (2018), **[Chapter 3]**.

   - The candidate contributed to the paper idea, implemented the coding in MATLAB software, and performed numerical analysis. He also wrote the first draft of the article and responded to the reviewers' comments.

2) **E. Ghorbani**, O. Buyukozturk, and Y. J. Cha, "*Hybrid output-only structural system identification using random decrement and Kalman filter,"* Mechanical Systems and Signal Processing, 144 (2020): 106977, **[Chapter 4]**.

   - The candidate initiated the use of the RD, as he found it to be useful for output-only damage quantification. The candidate implemented the coding in MATLAB software and performed numerical analysis. The candidate wrote the first draft of the article and responded to the reviewers' comments.

3) **E. Ghorbani** and Y. J. Cha, "*Analyzing the robustness of the hybrid output-only Kalman filtering–based system identification method*," 10th European Workshop on Structural Health Monitoring, Palermo, Italy, 225, November 2020, **[Chapter 5]**.

   - The candidate contributed to the paper idea, implemented the coding in MATLAB software, and performed numerical analysis. He also wrote the first draft of the article and responded to the reviewers' comments.

4) **E. Ghorbani,** D. Svecova, D. J. Thomson, and Y. J. Cha, "*Bridge pier scour level quantification based on output-only Kalman filtering*," Journal Structural Health Monitoring, (under review), **[Chapter 6]**.

- The candidate developed the idea of using the RD-UKF for bridge scour monitoring, designed the experiment, attached the vibration sensors to the bridge pier, and measured vibration data monthly. He also developed the mathematical model, implemented the coding in MATLAB software, and performed numerical analysis. Additionally, The candidate conducted the river bathymetry in the summer and winter seasons and was solely responsible for the experimental data analysis. He wrote the first draft of the paper for submission.

Acknowledgements

This Ph.D. thesis represents the effort and support of several people to whom I am incredibly grateful. First and foremost, I would like to express my special thanks and appreciation to my supervisors, Professor Youngjin Cha and Professor Dagmar Svecova. It has been a privilege to work with. Dr. Cha was inspiring, trusting, supporting and guiding me through my unpredictable Ph.D. journey. I'm sincerely grateful for Dr. Svecova's presence and attention as she supported me not only by providing a research assistantship but also academically and emotionally. Many thanks for your generous support when I needed it most.

The work presented in this thesis has been critically assessed and approved by outstanding committee members. I wish to extend my sincere gratitude to Professor Wenxing Zhou, Professor Saman Muthukumarana, and Professor Ehab El-Salakawy, for generously offering their time, support, and insightful feedback.

Many people helped me during my experimental study on the Manitoba Infrastructure (MI) Morris bridge project. Mrs. Evangeline Murison welcomed me to MI and provided me with all the sensing equipment and required technical information about the Morris bridge. I also thank Mr. Alexander Wall for his cooperation in measuring the riverbed height using the survey rod and ADP system, and Mr. Geoffrey Gao for his help in attaching the accelerometer to the pier. I would like to acknowledge the KGS group for letting me use their Ansys software to implement modal analysis on the whole bridge.

This research has been partially supported by the Research Manitoba SIRI program (Collaborator: SIMTReC) from 9/01/2016 to 08/31/2018, NSERC Discovery Grant - number :RGPIN/5914-2014- from 5/01/2020 to 06/01/2020, and NSERC Discovery Grant - number: RGPIN-2016-05923- from 4/01/2021 to 07/01/2021. I would also like to extend my gratitude to the University of Manitoba Graduate Fellowship and Douglas Grime fellowship programs.

A very special thanks goes to Professor Pooneh Maghoul for her invaluable advice and feedback on my research and for always being so supportive. I am also very grateful to Professor Mohammad Jafari Jozani, who helped me in numerous ways during my Ph.D. studies. I would like to acknowledge Mrs. Antoanela Denchuk for help and guidance through

writing the thesis. I would also like to thank all my friends (too many to list here, but you know who you are!) for their support, encouragement and friendship.

Fortunately, I also have the privilege of having a lovely wife and parents who had a fundamental role in my successful completion of the Ph.D. process. My parents, Sadat and Ahmad, thanks for letting me experience my life choices. I would need more than an entire acknowledgement section to thank you for everything you have done for me during my whole life. I also want to thank my parents-in-law, Behnaz and Naser, for their support and positive inspiration through the good times and bad. My dear Khatereh, there is no way to thank you for everything you have done for me. Simply, thanks for always being present and doing the (im)possible to keep me going further.

Dedication

To my Lovely *Khatereh,*

For her patience and her faith.

Table of Contents

Abstract ii

Co-authorship iv

Acknowledgements vi

Dedication viii

Table of Contents ix

List of Tables xiii

List of Figures xiv

Chapter One: Introduction 1

1.1. Background 2

1.2. Problem definition 4

1.3. Scope of work 5

1.4. Objective of research 6

1.5. Methodology 7

1.6. Research contribution 9

1.7. Dissertation outline 11

Chapter Two: Mathematical Background 14

2.1. Linear Kalman filter 15

2.2. Nonlinear Kalman filter 19

2.3. Normality assumption 22

2.4. Conclusion 23

Chapter Three: An Iterated Cubature Unscented Kalman Filter for Large-DoF Systems Identification with Noisy Data 24

3.1. Introduction 25
3.2. UKF-based system identification methods 27
3.2.1. Original UKF 28
3.2.2. Modified UKF 31
3.2.3. Iterated MUKF 35
3.3. Numerical examples 37
3.3.1. Bouc–Wen hysteretic model 37
3.3.2. Linear 3-DoF system 42
3.3.3. Linear 10-DoF system 45
3.4. Conclusion 50
Chapter Four: Hybrid Output-only Structural System Identification Using Random Decrement and Kalman Filter 51
4.1. Introduction 52
4.2. Problem description 56
4.3. Methodology 57
4.3.1. Random decrement method 57
4.3.2. Kalman filtering 60
4.4. Implementation of the approach to numerical and real examples 65
4.4.1. Case 1: A 3-DoF system with white noise excitation 65
4.4.2. Case 2: Damage identification of the 3-DoF with white noise excitation 69
4.4.3. Case 3: A 3-DoF system with periodic excitation 71
4.4.4. Case 4: A 3-DoF system with earthquake excitation 76
4.4.5. Case 5: A 10-DoF system with earthquake excitation 78
4.4.6. Case 6: A seven-story residential load bearing wall building 81
4.5. Conclusion 92

Chapter Five: Analyzing the Robustness of Hybrid, Output-only Kalman Filtering–based System Identification Method 94
5.1. Introduction 95
5.2. RD-UKF 97
5.3. RD-UKF robustness studies 99
5.3.1. Case 1: 3-DoF system under different loading conditions 100
5.3.2. Case 2: RD-UKF robustness under Monte Carlo simulations 101
5.3.3. Case 3: Mass matrix sensitivity analysis 103
5.3.4. Case 4: Missing sensor sensitivity analysis 105
5.4. Conclusion 108
Chapter Six: Bridge Pier Scour Level Quantification Based on Output-only Kalman Filtering 109
6.1. Introduction 110
6.2. Proposed method 114
6.2.1. Random decrement method 114
6.2.2. Eulerian beam model for a bridge pier 115
6.2.3. Kalman filtering 118
6.3. Case studies 122
6.3.1. Numerical simulations 122
6.3.2. A full-scale study of a bridge pier 129
6.4. Conclusion 137
6.5. Acknowledgement 138
Chapter Seven: Conclusions and Future Work 139
7.1. Conclusions 140
7.2. Future work 144
References 145

Appendix A i
Appendix B iii
Appendix C v
Appendix D viii
Appendix E xii

List of Tables

Table 3-1 Predicted results of the single-DoF nonlinear system using the Bouc–Wen model..... 41
Table 4-1**:** List of the dynamic tests to induce damage and ones used in the identification process..... 83
Table 4-2: The building lumped seismic each floor mass and the web wall geometrical information..... 86
Table 4-3: Comparison of the extracted natural frequencies..... 90
Table 6-1: Initial and tuning parameters for different soil profiles 127

List of Figures

Figure 1-1: Bridge failures due to scour. a) the Bonnybrook bridge in Calgary in 2013 [21]; b) the I-10 bridge in Southern California in 2015 [22] 5
Figure 2-1: The linear Kalman filter algorithm 19
Figure 3-1: UKF algorithm (left) and a simple flowchart (right) 31
Figure 3-2: The UKF and CKF points' placement 33
Figure 3-3: MUKF algorithm (left) and a simple flowchart (right)..... 35
Figure 3-4: EI Centro earthquake ground motion: (a) clean and noisy signals (two different SNRs of 40 and 15) and (b) a detailed view of the signals. 38
Figure 3-5: Predicted hysteretic loops 40
Figure 3-6: Predicted stiffness value..... 41
Figure 3-7: Predicted damping coefficient 41
Figure 3-8: Predicted stiffness (k1–k3) values for the 3-DoF system with SNR = 15 44
Figure 3-9: Predicted damping coefficient (c1–c3) values for a 3-DoF system with SNR = 15 45
Figure 3-10: Predicted stiffness (k1–k10) values for a 10-DoF system with SNR = 15 47
Figure 3-11: Predicted damping coefficient (c1–c10) values for a 10-DoF system with SNR = 15 49
Figure 4-1: The proposed output-only method flowchart based on the nonlinear KF. 57
Figure 4-2: The Random decrement procedure 58
Figure 4-3: The RD-UKF algorithm 64
Figure 4-4: a) The acceleration response of the 1st DoF of the 3-DoF system, b) the RD processed response as the free vibration response of the 1st DoF of the system, c) Power spectral density (PSD) of free vibration response from the 1st DoF 66
Figure 4-5: Case 1: Estimated stiffness (k1–k3) values with white noise excitation. . 68
Figure 4-6: Case 1: Estimated damping (c1–c3) values with white noise excitation. . 69
Figure 4-7: Case 2: Estimated stiffness (k1–k3) values with white noise excitation. . 70
Figure 4-8: Case 2: Estimated damping (c1–c3) values with white noise excitation. . 71
Figure 4-9: a) The periodic excitation, and b) the system total response. 73

Figure 4-10: The free vibration response of the system after removing external forces using the RD method. 74
Figure 4-11: Case 3: Estimated stiffness (k1–k3) values with periodic excitation..... 75
Figure 4-12: Case 3: Estimated damping (c1–c3) values with periodic excitation. 75
Figure 4-13: EI-Centro earthquake acceleration time history..... 76
Figure 4-14: a) system response due to El-Centro earthquake excitation, and b) the system free vibration response using the RD method..... 77
Figure 4-15: Case 4: Estimated stiffness (k1–k3) values with earthquake excitation. 77
Figure 4-16: Case 4: Estimated damping (c1–c3) values with earthquake excitation. 78
Figure 4-17: The proposed output-only method flowchart based on the IMUKF. 79
Figure 4-18: Case 5: Estimated stiffness (k1–k10) values for the 10-DoF system. 80
Figure 4-19: Case 5: Estimated damping (c1–c10) values for the 10-DoF system. 81
Figure 4-20: The building test structure [89]. 83
Figure 4-21: The free vibration response of the building each story without any damage (D0). 84
Figure 4-22: Estimated stiffness (k1– k7) values of the building within all damage states. 88
Figure 4-23: Estimated damping (c1– c7) values of the building within all damage states..... 88
Figure 5-1: The RD-UKF algorithm 99
Figure 5-2: Estimated stiffness (left column) and damping values (right column) ... 100
Figure. 5-3: a) Stair-step graphs and b) box-and-whisker plots, of stiffness values for each floor with 100 tests (signal-to-noise ratio = 30). 102
Figure. 5-4: a) Stair-step graphs and b) box-and-whisker plots, of damping values for each floor with 100 tests (signal-to-noise ratio = 30). 103
Figure. 5-5: Estimated stiffness (left column) and damping values (right column) of the model under mass distribution uncertainty. 104
Figure. 5-6: Estimated stiffness (left column) and damping values (right column) of the model in missing-sensor situations. 107
Figure. 6-1: Overall procedure of the proposed method..... 114
Figure. 6-2: Schematic view of the RD method 115

Figure. 6-3: Schematic view of Euler beam model of a bridge pier with rocker bearings 116
Figure. 6-4: a) The excitation applied to the simulating structure; b) the total acceleration vibration response of the structure..... 123
Figure. 6-5: a) The free vibration response of the system; b) The FFT of the free vibration response 124
Figure. 6-6: a) The estimated stiffness and b) damping value of the soil..... 125
Figure. 6-7: The estimated a) stiffness and b) damping value of the soil with constant profile affected by scour 126
Figure. 6-8: Results of soil height estimations: 128
Figure. 6-9: a) The free vibration response under scour; b) The FFT of the free vibration response of the system under scour 129
Figure. 6-10: Side view of the large-scale bridge system drawing..... 130
Figure. 6-11: Views of the bridge and installed sensor and data acquisition system 130
Figure. 6-12:Ambient vibrations of Pier 5..... 131
Figure. 6-13: Free vibration responses of Pier 5..... 131
Figure. 6-14: The high type rocker bearing of Pier 5 and its detailed drawing 132
Figure. 6-15: Estimated soil stiffness around the bridge pier in different months 133
Figure. 6-16: Estimated soil height around the bridge pier in different months..... 134
Figure. 6-17: a) The survey used for the soil height around the Pier 5; b) and schematic of the height of the soil around the Pier 5..... 135
Figure. 6-18: An Acoustic Doppler Profiler (ADP) boat and measured soil height around the Pier 5 in August 2020..... 136
Figure. 6-19:FFT of the free responses of the Pier 5 in different months 137
Figure C-1: The free vibration response of the building within the damage state one (D1)..... v
Figure C-2: The free vibration response of the building within the damage state two (D2)..... vi
Figure C-3: The free vibration response of the building within the damage state three (D3-1)..... vi

Figure C-4: The free vibration response of the building within the damage state four (D3-2) vii
Figure C-5: The free vibration response of the building within the damage state five (D4) vii

Chapter One:

Introduction

This chapter begins with a short introduction to the concepts of structural identification and structural damage identification. Damage identification approaches are presented and categorized based on their capabilities. The current state of the field, the problem statement, the scope of the work, the research objective, the proposed methodology for achieving this objective, and the research contribution are also explained in this chapter. An outline of the thesis is presented at the end.

1.1. **Background**

According to a report from the American Road & Transportation Builders Association (ARTBA), almost 8.86% of the 612,000 total bridges in the USA are structurally deficient and rapidly approaching the limit of their design service life [1, 2]. The conditions in Canada are even worse; out of about 75,000 highway bridges, almost one-fourth have structural or functional deficiencies [3]. The newly constructed bridges are designed based on the Canadian Highway Bridge Design Code for a service life of 75 years [4], but about 40% of the bridges are under operation more than the designed life because of the lack of resources. Therefore, identification and quantification of any damage or deterioration state that might occur is necessary to prevent catastrophic failures.

The process of monitoring the conditions of and identifying damage in civil, mechanical, and aerospace engineering structures in order to evaluate the system's remaining life span is called structural health monitoring (SHM). Damage is defined as any change that could affect the current or future performance of the system, such as changes to the material or geometric properties, the boundary conditions, or the system connectivity. These damages change the stiffness, mass, or energy dissipation properties of a system, altering the system's measured dynamic response. This datum acts as the foundation for vibration-based damage identification methods [5, 6].

Vibration-based damage identification is the process that detects any change in the dynamic’s specification (stiffness, mass, and damping) of the structural responses over time to avoid catastrophic failures. The damage identification process generally consists of three steps. In the first step, the occurrence of the damage has to be acknowledged (damage detection), the location of the damage must then be identified (damage localization), and finally, the extent of the damage to the structure (damage quantification) must be evaluated [7].

There are two significant branches of vibration-based damage identification approaches; there are data-driven approaches, which only use the measured structural responses from sensors installed in a structure to identify the damages; and physics model-

based approaches, which use a mathematical model in addition to the measured structural responses for damage identification.

In the data-driven-based approaches, the measured responses are analyzed to identify damage-sensitive features either with or without input excitations. Different damage-sensitive features can be defined for structural damage identification. Natural frequency, damping ratio, and mode shape function (modal parameters) are the common features extracted from vibration data that are usually used for damage identification in structures [8-11]. However, these data-drive features can hardly reach the damage quantification step of a damage identification process. Physics model-based approaches are developed to cover the limitation of data-based approaches.

Physics model-based approaches are able to quantify the level of detected damage in a structure. There are two broad branches of this physic model-based approach. The first uses modal updating to solve an inverse problem using heuristic optimization techniques. The numerical model developed based on the structural drawing is then updated to get the same natural frequencies and mode shapes observed in the monitored structure. Factors such as stiffness matrix, mass matrix, and the location and extent of the damage can then be quantified based on the updated model. However, this model updating is based on heuristic optimization methods that usually require a high computational cost to optimize [12-14].

The other branch uses Bayesian-based recursive filters such as Kalman filters and particle filters. These methods require a numerical model of the structural system and their input excitations and output responses to estimate structural properties such as stiffness and mass. In these methods, the output responses predicted by the mathematical model and the corresponding measured outputs are compared with the goal of minimizing a specific loss function. This process updates the mathematical model parameters through a recursive process that converges the simulation response with the measured one. It requires relatively low computational cost compared to the inverse solving approaches using heuristic searches and can even make real-time processing possible depending on the dimension of the mathematical model [15].

1.2. **Problem definition**

The Kalman filtering-based methods use a mathematical model and the output responses due to input excitations to update the mathematical model parameters using an iterative process. These approaches were initially widely used for structural system identification purposes but, due to their fast-processing time, their applications have been extended to include damage identification problems [16-18]. However, the evidence (literature review and simulation study) shows that their estimation accuracy significantly decreases as the number of unknown parameters increases, thereby increasing the dimension of the mathematical model. Conversely, increasing the dimension of the mathematical model (number of DoF[1]) improves the accuracy of its response in terms of the actual system behaviour [19]. This trade-off, as one of the main weaknesses of these approaches, is addressed in this study.

In the process of Kalman filtering-based damage identification of real structures, such as a bridge in a routine operation or a building under seismic excitation, cannot generally measure the input excitation. The uncertainties related to these unknown excitations drastically decrease the performance of these methods. The literature review reveals that all previous research on this topic has tried to estimate or reconstruct input excitation in the estimation process. There are always uncertainties related to these input identification processes that eventually decrease the accuracy of the estimated parameters. An output-only Kalman filtering damage quantification method is introduced in this thesis in order to overcome this drawback.

For example, identifying the unknown input excitations acting on a structure like a bridge and developing an accurate mathematical model to represent bridge pier behaviour is one of the main challenges in the model-based bridge scour monitoring process. Bridge scouring, the excavation and removal of sediment around a bridge pier by the flowing water's erosive action, cause more than 50% of bridge failures in the U.S. [20]. In addition to the loss of human life, economic loss and disruption to transportation systems may also occur

1 Degree of freedom

because of bridge scour. The failure of the Bonnybrook Bridge in Calgary in 2013 and the I-10 bridge in southern California in 2015 are two recent notable cases of bridge failure in North America due to pier and abutment scour, as shown in Figure 1-1.

(a) (b)

Figure 1-1: Bridge failures due to scour. a) the Bonnybrook bridge in Calgary in 2013 [21]; b) the I-10 bridge in Southern California in 2015 [22]

The extensive literature review has revealed that no reliable model-based approach exists to quantify the scour level around a bridge pier in real-time. Developing a scour monitoring system that can provide the level of scour in a near real-time manner is critical to prevent catastrophic bridge failure.

1.3. **Scope of work**

The Kalman filter is an optimal Bayesian recursive filter that can be used to estimate a structure's dynamic specifications. The filter adjusts updateable variables (i.e., Kalman Gain) in a recursive scheme to reduce the difference between the predicted state vector in two time-steps [23]. The linear Kalman filter was initially developed to track a system state vector with noisy data in the 1960s by Kalman and Bucy [24]. It has shown accurate results in identifying a linear system with a small number of parameters; the measured data follows the Gaussian distribution.

The unscented Kalman filter (UKF), the ensemble Kalman filter (EnKF), and the cubature Kalman filter (CKF) are other forms of Kalman filters capable of identifying

nonlinear systems. Kalman filters are more efficient computationally than other model-based methods and have therefore received more attention. For example, the particle filter, another model-based method, which works based on the Markov chain Monte Carlo approach, has optimal estimation in terms of nonlinear and non-Gaussian environments. However, it is computationally extensive and slow in converging to the clean response [25]. Therefore, this study focuses on Kalman filtering methods.

In this work, the Kalman filtering methods are integrated with other methods (either model-based or data-based) to improve the Kalman filtering estimation performance for high-dimensional mathematical models. Each novel method is evaluated under extensive linear and nonlinear numerical models and full-scale experimental studies.

1.4. **Objective of research**

The main objective of this study is to improve the performance of traditional Kalman filtering and develop an output-only Kalman filtering that is capable of identifying a high-dimensional mathematical model with a large number of unknown parameters for damage quantification. This goal is divided into two steps:

1- Improving the performance of the Kalman filtering for damage quantification of structural systems with high dimensional state vectors (unknown parameters). It is assumed that enough information about the input excitation is available in this step.

2- Developing an output-only Kalman filtering-based damage quantification method and the proposed method performance is verified with experimental data with completely unknown input excitation.

Adopting the introduced output-only Kalman filtering method for bridge scour quantification is the next objective of this dissertation. A novel physics-based model representing pier behaviour is developed to consider the necessary boundary conditions at both ends of the pier, the soil effect, and induced vibrations due to crossing cars, pedestrians,

and the water beating the pier. The model is examined for output-only scour quantification of a bridge prone to scour located in Manitoba, Canada

1.5. **Methodology**

The UKF and CKF are the types of Kalman filtering most frequently used for structural damage identification. They are a derivative-free type of Kalman filtering algorithm that, instead of linearizing the transition and measurement functions, calculate the covariance matrix of the desired parameters using some predefined points called sigma points [26-28]. The UKF or CKF propagates these sigma points through the transition and measurement functions in each iteration.

The sigma points are calculated using prior information ($\mathbf{m}$, and $\mathbf{P}_0$) distributed around the mean of states in each iteration. The number of sigma points and their distribution is an essential parameter in the estimation process. The sigma points and their corresponding sigma weights are calculated using these three equations:

$$\sum_{i=0}^{2n} w_i = 1, \tag{1.1}$$

$$\sum_{i=0}^{2n} w_i \boldsymbol{\chi}_i = \mathbf{m}, \tag{1.2}$$

$$. \sum_{i=0}^{2n} w_i \left(\chi_i - \mathbf{m}\right)\left(\chi_i - \mathbf{m}\right)^T = \mathbf{P}_0, . \tag{1.3}$$

where $\boldsymbol{\chi}_i$, and w_i are sigma points and their corresponding sigma weights, respectively, and n represents the number of states. The two most popular solutions of these equations lead to the UKF sigma points [28] and the CKF sigma points [29].

The UKF or CKF can estimate the desired states of highly nonlinear systems but increasing the number of unknown states weakens their estimation accuracy. A new method called the Iterative Modified Unscented Kalman filter (IMUKF) is introduced to compensate for the weaknesses of the pure UKF or CKF in systems with a large number of unknown parameters. The IMUKF is developed by combining the sigma points of the UKF and CKF to achieve more precise information about the system in each iteration. Following that, the propagated states are distributed twice for more symmetric distribution of data around the mean vector in each iteration. The proposed method results are more accurate than pure UKF or CKF results for systems with 20 or more unknown parameters.

In the proposed IMUKF, as with any Kalman filtering process, the desired parameters are accumulated using a vector called a state vector. The state vector can contain either the system-desired parameters only or a combination of the system desired parameters and the system input excitation when the input excitation is non-informative. Accumulating both input parameters and desired parameters in the same state vector is an output-only Kalman filtering method known as the joint state-input estimation method [30]. This combination reduces estimation accuracy compared to a pure state vector that only contains the desired parameters. One possible solution involves eliminating the forced vibration response from the underlying system's total measured vibration. The remaining response is the system's free vibration response, which carries information about its dynamic specifications.

Random decrement (RD) is a method that extracts the free vibration response of a system from its corresponding total vibration response. The RD is categorized as a data-based method [31] that works by averaging a limited number of time segments in the total vibrational response. The free vibration response is extracted without any complicated or extensive mathematical operations. The RD technique was initially defined for white noise excitations but has recently been developed for use in systems with periodic, ambient, and non-stationary excitations [32]. It has also been developed for use with nonlinear systems [33]. Therefore, the RD and the Kalman filtering are integrated to identify unknown parameters of a structural model. This combination improves the performance of the Kalman filter in the identification of mathematical models with a large number of unknown parameters. The performance of the introduced method is examined by the data measured

from a seven-story building located at the University of California San Diego. The building was excited with different levels of earthquakes, and the vibration response of the building on each floor after each excitation is recorded. The introduced method was used to quantify the level of damage in each floor for each state of damage.

The RD method can extract the free vibration response of a bridge pier under routine operation. The extracted free vibration response is dependent on the boundary condition of the bridge pier, which is equivalent to soil height around the bridge pier. Therefore, developing an accurate mathematical model that represents bridge pier behaviour and employing that model in the introduced RD-UKF will quantify the soil height around the bridge pier. A continuous Euler beam theory is used to develop an accurate mathematical model for the bridge pier that considers all external boundary conditions affecting pier behaviour, such as soil effect, bearings, and river water beating the pier. The mathematical equations are derived and, after simplification and discretization, transformed into state-space forms that are compatible with Kalman filtering.

A 300-meter length mid-span bridge, named Morris bridge, was selected to quantify the level of scour around the bridge pier using the introduced continuous model and the RD-UKF method introduced in this dissertation. An accelerometer was attached to the top of the deepest pier of the bridge near the girder bearing. The vibration response was recorded monthly during the normal operation of the bridge. The data is used to estimate the soil height around the pier, and the estimated soil height during months are compared to identify scour in its early stages.

1.6. **Research contribution**

The first contribution of this dissertation is the introduction of IMUKF, which is developed through the combination of the UKF and CKF sigma points. Its convergence is assured by the addition of another convergence criterion, although this also increases computational cost as compared to using pure UKF or CKF. Different numerical models are employed to evaluate the performance of the introduced method as compared to pure UKF or CKF. A

nonlinear Bouc-Wen model, a three DoF linear system, and a ten DoF linear system with about 40 states are employed to compare the performances of the UKF, CKF, and IMUKF in systems with different DoFs. The results confirm that the proposed method is superior to pure UKF or CKF for state estimation of a system with 20 or more states. The mathematical background of the IMUKF, the details of the proposed method, and the simulation studies are explained in Chapter 3.

A novel output-only structural damage quantification method is introduced as the second contribution of this dissertation. The proposed method combines the RD, a data driven-based approach, and the UKF, a model-based approach into RD-UKF. This integration offers a new approach in terms of SHM called the hybrid damage detection approach. This hybrid RD-UKF takes advantage of both data-based and model-based approaches to define new methods of structural damage quantification. For example, the solo free vibration response analysis barely includes information on damage location and cannot reach the third step of the damage identification process (damage quantification). Therefore, as a novel idea, the extracted free vibration response (data-based result) refers to the UKF, or any other form of Kalman filter, to estimate the desired parameters in a model-based scheme. The estimated states are used for damage quantification of the underlying structure.

The proposed RD-UKF simplifies the transition and measurement functions in the filtering process because it does not require any stochastic parameter related to excitation in the transition and measurement functions. This both reduces the uncertainties associated with the identification process and decreases the size of the state vector in the identification process. The RD-UKF performance and estimation accuracy are evaluated in Chapter 4 using extensive numerical and experimental studies. Following that, various sensitivity analyses are carried out in Chapter 5 to assure the robustness of the method.

The next contribution of this dissertation involves using the RD-UKF method to develop a comprehensive scour quantification method. A suitable physical model is developed to represent pier behaviour; it assumes that the bridge bier is an Euler beam and considers the necessary boundary conditions at both ends of the beam model. The pier is excited using water beating the pier, a live traffic load, and some additional white noise as other unknown excitations. Therefore, the previously developed RD-UKF method is used to

eliminate unknown excitations and estimate the soil stiffness around the pier. A profile is also defined for the soil around the pier to estimate its height.

The performance of this method is then examined in a simulation study; the method is shown to be capable of scour quantification. The method is examined using data measured from a full-scale 300-meter bridge located in Morris, Manitoba, to show the effectiveness of the research on Canada's infrastructure system. An accelerometer is installed at the top of one of the bridge piers and the vibration data is recorded periodically. The soil stiffness and height around the pier are estimated.

As verification for the vibration-based results, the soil height around the pier is measured in both winter and summer using an independent bathymetry. The vibration-based result and the bathymetry results are in good agreement; each step is explained in detail in Chapter 6.

1.7. **Dissertation outline**

This dissertation is based on a group of papers; the candidate peer-reviewed papers in various stages of publication are enclosed in Chapters 3-6.

This chapter includes the framework of the research and the main ideas behind the work. Chapter 2 presented the mathematical background of the linear Kalman filter, which demonstrates the assumptions involved in the Kalman filtering derivation process. Following that, the main idea behind the nonlinear Kalman filtering is presented, eventually leading to the unscented Kalman filter and cubature Kalman filter. This chapter provides the background that will be used to develop the mathematical equations in the subsequent chapters.

Chapter 3 includes the first peer-reviewed paper published in the *Journal of Sound and Vibration*[1]. The paper focuses on improving the performance of the UKF for a system with a large number of states. This chapter reviews the basics of the unscented Kalman filter, cubature Kalman filter, and iterative Kalman filter in detail. It then discusses how these three filters are combined to achieve better accuracy in large-scale systems. The proposed method is evaluated using numerous simulation studies on linear and nonlinear models.

Chapter 4 includes a peer-reviewed paper published in the Journal *Mechanical Systems and Signal Processing* [2]that introduces the RD-UKF method for output-only system identification purposes. The method combines the random decrement (as a data-based method) and the unscented Kalman filter (as a model-based method) to quantify structural damage level. This method can be used for any structure with any kind of excitations and has been verified with data measured from a full-scale seven-story building located at the University of California, San Diego.

In Chapter 5, a conference paper, published and presented in the 10th *European Workshop on Structural Health Monitoring* (EWSHM 2020)[3], explains an extensive sensitivity analysis performed on the RD-UKF method to check its robustness under different uncertainties related to output-only system identification and damage identification. The RD-UKF is evaluated for the Monte Carlo simulation study, missing sensor, different excitations, and uncertainties related to the system's mass matrix. The analysis confirms the robustness of the RD-UKF under different uncertainties associated with a damage quantification process.

---

1 **E. Ghorbani**, and Y. J. Cha, "*Iterated cubature unscented Kalman filter for large-DoF systems identification with noisy data*", Journal of Sound and Vibration, 420, 21-34, (2018).

2 **E. Ghorbani**, O. Buyukozturk, and Y. J. Cha, "*Hybrid output-only structural system identification using random decrement and Kalman filter*", Mechanical Systems and Signal Processing, 144 (2020): 106977.

3 **E. Ghorbani** and Y. J. Cha, "*Analyzing the robustness of hybrid, output-only, Kalman filtering–based system identification method*", European Workshop on Structural Health Monitoring. EWSHM 2020. Lecture Notes in Civil Engineering, vol 127, pp 533-542. Springer.

This dissertation's potential positive impact on the safety of Canada's infrastructures is demonstrated in Chapter 6. A scour level quantification method is introduced and its performance is tested on data measured from a bridge prone to scour. The method also estimates the soil level around the pier. The estimated result was successfully verified with independent bathymetry measurements. The results from this chapter have been submitted to the peer-reviewed journal *Structural Health Monitoring*[1].

Chapter 7 includes a summary of the accomplishments of this research and suggestions for future work.

1 **E. Ghorbani**, D. Svecova, D. J. Thomson and Y. J. Cha, "*Bridge pier scour level quantification based on output-only Kalman filtering*", Journal Structural Health Monitoring, [Submitted, Dec. 22, 2020].

Chapter Two:

Mathematical Background

This chapter provides the mathematical basis for linear Kalman filtering and emphasizes its limitations. The ways that these limitations directed the studies to develop the extended Kalman filter and, following that, the unscented Kalman filter and the cubature Kalman filter will be discussed. These mathematical equations provide adequate background for the introduction of some solutions in the following chapters.

2.1. **Linear Kalman filter**

The Kalman filter, defined by Rudolf Kalman [24, 34], is a recursive algorithm that estimates the parameter of interest in a prediction and correction process, assuming the Gaussian distribution of measured data. The word filter, in this case, refers to an algorithm that infers a desired quantity at the time t using the data measured from time zero to t, including the time t itself [35].

The dynamic governing equation of a structural system in a discrete state-space domain has the form of

$$\begin{aligned} \mathbf{x}_{n+1} &= \mathrm{f}(\mathbf{x}_n, \mathbf{u}_n, \mathbf{v}_n) \quad \mathbf{v}_n : \mathbb{N}(0, \mathbf{Q}), \\ \mathbf{y}_n &= \mathrm{g}(\mathbf{x}_n, \mathbf{u}_n, \mathbf{w}_n) \quad \mathbf{w}_n : \mathbb{N}(0, \mathbf{R}), \end{aligned} \tag{2.1}$$

where n is a time step, $\mathbf{x}_n$ presents the state vector, $\mathbf{u}_n$ represents the input (driving force) vector, $\mathbf{v}_n$ and $\mathbf{w}_n$ define the process and measurement noises with $\mathbf{Q}$ and $\mathbf{R}$ as their respective covariance matrices. The term $\mathbb{N}$ represents the Gaussian distribution. The f and g can be any arbitrary functions representing the process and measurement functions in sequence. These functions can also be written as transition and measurement matrices in a linear system. The linear Kalman filter was initially developed based on linear state-space equations; Eq. (2.1) can be simplified for a linear system with deterministic excitation as follows:

$$\begin{aligned} \mathbf{x}_n &= \mathbf{F}_{n,n-1}\mathbf{x}_{n-1} + \mathbf{v}_{n-1}, \quad \mathbf{v}_n : \mathbb{N}(0, \mathrm{Q}), \\ \hat{\mathbf{y}}_n &= \mathbf{G}_n\mathbf{x}_n + \mathbf{w}_n, \qquad \mathbf{w}_n : \mathbb{N}(0, \mathrm{R}), \end{aligned} \tag{2.2}$$

where $\mathbf{F}_{n,n-1}$ and $\mathbf{G}_n$ are the transition and measurement matrices, respectively. The analytical filtering solution of Eq. (2.2) is called the Kalman filter, assuming Gaussian measured data [24]. It is assumed that the process and measurement noises components are independent under the Kalman filter derivation process ($\mathrm{E}[\mathbf{v}_n\mathbf{v}_m^{\mathrm{T}}] = \delta_{nm}\mathbf{Q}$, $\mathrm{E}[\mathbf{w}_n\mathbf{w}_m^{\mathrm{T}}] = \delta_{nm}\mathbf{R}$,) as are both the measurement and process noises and states ($\mathrm{E}[\mathbf{x}_n\mathbf{v}_m^{\mathrm{T}}] = 0$, $\mathrm{E}[\mathbf{x}_n\mathbf{w}_m^{\mathrm{T}}] = 0$) too

[35]. The Kalman filter primarily estimates the mean and covariance of a Gaussian posterior distribution as the distribution of desired parameters [35].

The Bayes rule is commonly used to estimate the posterior of the desired states using the measured data as follows:

$$p(\mathbf{x}_n \mid \mathbf{Y}_n) = \frac{p(\mathbf{Y}_n \mid \mathbf{x}_n)p(\mathbf{x}_n)}{p(\mathbf{Y}_n)}, \tag{2.3}$$

where $\mathbf{Y}_n = [\mathbf{y}_1, \mathbf{y}_2, \cdots, \mathbf{y}_n]$ is the measured data vector. Assuming the first Markov process for the measurements and some simplification, the Eq. (2.3) is rewritten as:

$$p(\mathbf{x}_n \mid \mathbf{Y}_n) = \frac{p(\mathbf{y}_n \mid \mathbf{Y}_{n-1}, \mathbf{x}_n)p(\mathbf{x}_n \mid \mathbf{Y}_{n-1})}{p(\mathbf{y}_n \mid \mathbf{Y}_{n-1})}, \tag{2.4}$$

where $p(\mathbf{y}_n \mid \mathbf{Y}_{n-1}, \mathbf{x}_n)$ represents the likelihood, $p(\mathbf{x}_n \mid \mathbf{Y}_{n-1})$ defines the prior information on the system, and $p(\mathbf{y}_n \mid \mathbf{Y}_{n-1})$ is the normalizing constant. Based on the initial assumption of white noise Gaussian distribution for process and measurement noises, the mean and covariance of the predicted states are calculated as follows:

$$\begin{aligned} &E\left[\mathbf{x}_n \mid \mathbf{Y}_{n-1}\right] = E\left[\mathbf{F}_{n,n-1}\mathbf{x}_{n|n-1} + \mathbf{v}_n\right] = \mathbf{F}_{n,n-1}\mathbf{x}_{n|n-1} = \hat{\mathbf{x}}_{n|n-1}, \\ &Cov\left[\mathbf{x}_n \mid \mathbf{Y}_{n-1}\right] = Cov\left[\mathbf{x}_n - \hat{\mathbf{x}}_{n|n-1}\right] = Cov\left[\mathbf{e}_{n|n-1}\right] = \mathbf{P}_{n|n-1}\ , \end{aligned} \tag{2.5}$$

where $\hat{\mathbf{x}}_{n|n-1}$ represents the state prediction at the time step n given all the observations up to the time step $n-1$, $\mathbf{e}_{n|n-1}$ defines the state error vector, and $\mathbf{P}_{n|n-1}$ corresponds to its covariance matrix. Therefore, the Gaussian distribution of the prior information is:

$$p(\mathbf{x}_n \mid \mathbf{Y}_{n-1}) = C_1 \exp[-\frac{1}{2}(\mathbf{x}_n - \hat{\mathbf{x}}_{n|n-1})^T \mathbf{P}_{n|n-1}^{-1}(\mathbf{x}_n - \hat{\mathbf{x}}_{n|n-1})], \tag{2.6}$$

where $C_1 = (2\pi)^{-N_x/2}\left|\mathbf{P}_{n|n-1}\right|^{-1/2}$. N_x is the size of the vector $\mathbf{x}_n$. The same steps will be followed to find the parameters of the Gaussian distribution of likelihood:

$$\begin{aligned} &\mathrm{E}[\mathbf{y}_n \mid \mathbf{x}_n] = \mathrm{E}[\mathbf{G}_n\mathbf{x}_n + \mathbf{w}_n] = \mathbf{G}_n\mathbf{x}_n \\ &\mathrm{Cov}[\mathbf{y}_n \mid \mathbf{x}_n] = \mathrm{Cov}[\mathbf{w}_n \mid \mathbf{x}_n] = \mathbf{R}. \end{aligned} \tag{2.7}$$

Therefore, the probability density function (pdf) of the likelihood is given by:

$$\mathrm{p}(\mathbf{y}_n \mid \mathbf{x}_n) = \mathrm{C}_2 \exp[-\frac{1}{2}(\mathbf{y}_n - \mathbf{G}_n\mathbf{x}_n)^{\mathrm{T}}\mathbf{R}^{-1}(\mathbf{y}_n - \mathbf{G}_n\mathbf{x}_n)], \tag{2.8}$$

where $\mathrm{C}_2 = (2\pi)^{-\mathrm{N_y}/2}|\mathbf{R}|^{-1/2}$ and $\mathrm{N_y}$ is the size of the vector $\mathbf{y}_n$. Substituting the Eq. (2.6) and Eq. (2.8) into the Bayes equation (2.4) results in the following:

$$\begin{aligned} \mathrm{p}(\mathbf{x}_n \mid \mathbf{Y}_n) \propto \tilde{\mathrm{C}} \exp[&-\frac{1}{2}(\mathbf{y}_n - \mathbf{G}_n\mathbf{x}_n)^{\mathrm{T}}\mathbf{R}^{-1}(\mathbf{y}_n - \mathbf{G}_n\mathbf{x}_n) \\ &-\frac{1}{2}(\mathbf{x}_n - \hat{\mathbf{x}}_{n|n-1})^{\mathrm{T}}\mathbf{P}_{n|n-1}^{-1}(\mathbf{x}_n - \hat{\mathbf{x}}_{n|n-1})], \end{aligned} \tag{2.9}$$

that $\tilde{\mathrm{C}} = \mathrm{C}_1\mathrm{C}_2$, and as the normalizing constant does not affect the optimal filtering process, it has been removed to simplify the future calculations. In the Bayesian inference, optimal filtering is achievable under different conditions like maximum likelihood (ML) and maximum a posterior (MAP) [35]. In this study, followed by the derivation presented by Chen [35], the MAP criteria is used to derive the linear Kalman filtering algorithm as below:

$$\frac{\partial \log \mathrm{p}(\mathbf{x}_n \mid \mathbf{Y}_n)}{\partial \mathbf{x}_n} \Big|_{\mathrm{x}_n = \hat{\mathrm{x}}_{\mathrm{MAP}}} = 0. \tag{2.10}$$

The Eq. (2.9) is substituted into Eq. (2.10), and after some simplification, the $\hat{\mathbf{x}}_{\mathrm{MAP}}$ is extracted as

$$\hat{\mathbf{x}}_n^{\mathrm{MAP}} = \hat{\mathbf{x}}_{n|n-1} + \mathbf{K}_n(\mathbf{y}_n - \mathbf{G}_n\hat{\mathbf{x}}_{n|n-1}), \tag{2.11}$$

where $\mathbf{K}_n$ is the Kalman Gain and is extracted as

$$\mathbf{K}_n = \mathbf{F}_{n|n-1}\mathbf{P}_{n|n-1}\mathbf{G}_n^T(\mathbf{G}_n\mathbf{P}_{n|n-1}\mathbf{G}_n^T + \mathbf{R})^{-1}, \tag{2.12}$$

that based on Eq. (2.5), $\mathbf{P}_{n|n-1} = \mathrm{Cov}\left[\mathbf{e}_{n|n-1}\right]$. The $\mathbf{e}_{n|n-1}$ is given by

$$\begin{aligned}\mathbf{e}_{n|n-1} &= \mathbf{x}_n - \hat{\mathbf{x}}_{n|n-1} = \mathbf{F}_{n,n-1}\mathbf{x}_{n-1} + \mathbf{v}_{n-1} - \mathbf{F}_{n,n-1}\hat{\mathbf{x}}_{n-1}^{MAP} \\ &= \mathbf{F}_{n,n-1}\mathbf{e}_{n-1}^{MAP} + \mathbf{v}_{n-1},\end{aligned} \tag{2.13}$$

Therefore,

$$\mathbf{P}_{n|n-1} = \mathrm{Cov}\left[\mathbf{e}_{n|n-1}\right] = \mathbf{F}_{n,n-1}\mathbf{P}_{n-1}\mathbf{F}_{n,n-1}^T + \mathbf{Q}, \tag{2.14}$$

and with the same terminology, the $\mathbf{P}_{n-1} = \mathrm{Cov}\left[\mathbf{e}_{n-1}^{MAP}\right]$ is given by

$$\mathbf{P}_n = \mathrm{Cov}[\mathbf{x}_n - \hat{\mathbf{x}}_n^{MAP}] = \mathbf{P}_{n|n-1} - \mathbf{F}_{n,n-1}\mathbf{K}_n\mathbf{G}_n\mathbf{P}_{n|n-1}. \tag{2.15}$$

Thus, the linear Gaussian Kalman filter has been derived based on MAP criteria for optimal filtering [35]. The algorithm is summarized in Figure 2-1. It should be noted that the updated state vector and covariance matrix will be used as the inputs for the next iteration. This process continues until the difference between two different iterations is less than a specific threshold.

Linear Kalman filter algorithm

define an initial $\mathbf{x}_0$, and $\mathbf{P}_0$,

set $\mathbf{R}$, $\mathbf{Q}$, Δt, and T_{end}

for $n = 1 : T_{end} / \Delta t$

prediction:

$$\hat{\mathbf{x}}_{n|n-1} = \mathbf{F}_{n,n-1}\mathbf{x}_{n-1}$$

$$\mathbf{P}_{n|n-1} = \mathbf{F}_{n,n-1}\mathbf{P}_{n-1}\mathbf{F}_{n,n-1}^{T} + \mathbf{Q},$$

$$\mathbf{K}_n = \mathbf{F}_{n|n-1}\mathbf{P}_{n|n-1}\mathbf{G}_n^{T}(\mathbf{G}_n\mathbf{P}_{n|n-1}\mathbf{G}_n^{T} + \mathbf{R})^{-1},$$

update:

$$\hat{\mathbf{x}}_n^{MAP} = \hat{\mathbf{x}}_{n|n-1} + \mathbf{K}_n(\mathbf{y}_n - \mathbf{G}_n\hat{\mathbf{x}}_{n|n-1}),$$

$$\mathbf{P}_n = \mathbf{P}_{n|n-1} - \mathbf{F}_{n,n-1}\mathbf{K}_n\mathbf{G}_n\mathbf{P}_{n|n-1}\ .$$

end

Figure 2-1: The linear Kalman filter algorithm

The algorithm above is developed based on MAP criteria. The same result is achievable under ML criteria as well [35, 36]. It should be noted that the algorithm can also be derived under minimizing mean square error (MMSE) criteria [37]. The MMSE is equivalent to ML for Gaussian distribution.

The linear Kalman filter is derived for linear systems under the Gaussian distribution assumption for the estimated states and measured data. Ignoring the linearity assumption causes a biased estimation and deviation from the exact answer. Several different experiments have been conducted to answer this limitation.

2.2. **Nonlinear Kalman filter**

The extended Kalman filter (EKF) is an improved version of the linear Kalman filter that is more suitable for nonlinear systems based on linearization using the Taylor series [38].

Referring to Eq. (2.1), the transition and measurement matrices for the EKF are calculated as below:

$$\mathbf{F} = \frac{\partial \mathrm{f}}{\partial \mathrm{x}}\Big|_{\mathrm{x}=\bar{\mathrm{x}}} = \begin{bmatrix} \frac{\partial \mathrm{f}_1}{\partial \mathrm{x}_1} & \frac{\partial \mathrm{f}_1}{\partial \mathrm{x}_2} & \cdots & \frac{\partial \mathrm{f}_1}{\partial \mathrm{x}_{\mathrm{N_x}}} \\ \frac{\partial \mathrm{f}_2}{\partial \mathrm{x}_1} & \frac{\partial \mathrm{f}_2}{\partial \mathrm{x}_2} & & \vdots \\ \vdots & & \ddots & \vdots \\ \frac{\partial \mathrm{f}_{\mathrm{N_x}}}{\partial \mathrm{x}_1} & \cdots & \cdots & \frac{\partial \mathrm{f}_{\mathrm{N_x}}}{\partial \mathrm{x}_{\mathrm{N_x}}} \end{bmatrix}, \tag{2.16}$$

$$\mathbf{G} = \frac{\partial \mathrm{g}}{\partial \mathrm{x}}\Big|_{\mathrm{x}=\bar{\mathrm{x}}} = \begin{bmatrix} \frac{\partial \mathrm{g}_1}{\partial \mathrm{x}_1} & \frac{\partial \mathrm{g}_1}{\partial \mathrm{x}_2} & \cdots & \frac{\partial \mathrm{g}_1}{\partial \mathrm{x}_{\mathrm{N_x}}} \\ \frac{\partial \mathrm{g}_2}{\partial \mathrm{x}_1} & \frac{\partial \mathrm{g}_2}{\partial \mathrm{x}_2} & & \vdots \\ \vdots & & \ddots & \vdots \\ \frac{\partial \mathrm{g}_{\mathrm{N_y}}}{\partial \mathrm{x}_1} & \cdots & \cdots & \frac{\partial \mathrm{g}_{\mathrm{N_y}}}{\partial \mathrm{x}_{\mathrm{N_x}}} \end{bmatrix}, \tag{2.17}$$

where $\mathrm{N_x}$, and $\mathrm{N_y}$ indicate the length of the state vector and the measurement vector, respectively. Considering the level of nonlinearity in the system, Eq. (2.16) and Eq. (2.17) can be derived for the second order of the Taylor series. The EKF algorithm is as same as the linear Kalman filter algorithm, the only difference is related to the extraction of the transition and measurement matrices from their corresponding nonlinear functions.

However, the EKF does not converge to a clean answer for highly nonlinear systems. Furthermore, the calculation of first or second derivatives is a difficult task for many systems [39]. The unscented Kalman filter (UKF) and the cubature Kalman filter (CKF) are derivative-free types of Kalman filtering developed to address the limitations of EKF [26-29]. The UKF and CKF focus on calculating the covariance matrices as opposed to linearizing the transition and measurement functions, a much more straightforward job. The main idea of these derivative-free Kalman filters is inspired by the linear Kalman filter

derivation process. Lets in Eq. (2.14) defines the covariance of the states ($\mathbf{P}_n^{\mathbf{XX}}$) in each iteration as shown below:

$$\mathbf{P}_{n|n-1} = \mathrm{Cov}\left[\mathbf{e}_{n|n-1}\right] = \mathbf{F}_{n,n-1}\mathbf{P}_{n-1}\mathbf{F}_{n,n-1}^{\mathrm{T}} + \mathbf{Q} = \mathbf{P}_n^{\mathbf{XX}}, \tag{2.18}$$

so the $\mathbf{P}_n^{\mathbf{YY}}$ and $\mathbf{P}_n^{\mathbf{XY}}$ is given as:

$$\begin{aligned}\mathbf{P}_n^{\mathbf{YY}} &= \mathrm{Cov}(\mathbf{y}_n - \mathrm{E}(\mathbf{y}_n)) = \mathrm{E}[(\mathbf{G}_n\mathbf{x}_n + \mathbf{w} - \mathbf{G}_n\hat{\mathbf{x}}_{n|n-1})(\mathbf{G}_n\mathbf{x}_n + \mathbf{w}_n - \mathbf{G}_n\hat{\mathbf{x}}_{n|n-1})^{\mathrm{T}}], \\ &= \mathbf{G}_n\mathbf{P}_{n|n-1}\mathbf{G}_n^{\mathrm{T}} + \mathbf{R}.\end{aligned} \tag{2.19}$$

$$\begin{aligned}\mathbf{P}_n^{\mathbf{XY}} &= \mathrm{E}[(\mathbf{x}_n - \mathrm{E}(\mathbf{x}_n))(\mathbf{y}_n - \mathrm{E}(\mathbf{y}_n))^{\mathrm{T}}] \\ &= [(\mathbf{F}_{n,n-1}\mathbf{x}_{n|n-1} + \mathbf{v}_n - \mathbf{F}_{n,n-1}\hat{\mathbf{x}}_{n|n-1})(\mathbf{G}_n\mathbf{x}_n + \mathbf{w}_n - \mathbf{G}_n\hat{\mathbf{x}}_{n|n-1})^{\mathrm{T}}], \\ &= \mathbf{F}_{n,n-1}\mathbf{P}_{n|n-1}\mathbf{G}_n^{\mathrm{T}}.\end{aligned} \tag{2.20}$$

Following that, the Kalman Gain in Eq. (2.12) is calculated as shown below:

$$\mathbf{K}_n = \mathbf{F}_{n,n-1}\mathbf{P}_{n|n-1}\mathbf{G}_n^{\mathrm{T}}(\mathbf{G}_n\mathbf{P}_{n|n-1}\mathbf{G}_n^{\mathrm{T}} + \mathbf{R})^{-1} = \mathbf{P}_n^{\mathbf{XY}}(\mathbf{P}_n^{\mathbf{YY}})^{-1}. \tag{2.21}$$

Additionally, Eq. (2.15) is rearranged as:

$$\begin{aligned}\mathbf{P}_n &= \mathrm{Cov}[\mathbf{x}_n - \hat{\mathbf{x}}_n^{\mathrm{MAP}}] = \mathbf{P}_{n|n-1} - \mathbf{F}_{n,n-1}\mathbf{K}_n\mathbf{G}_n\mathbf{P}_{n|n-1} \\ &= \mathbf{P}_n^{\mathbf{XX}} - \mathbf{K}_n\mathbf{P}_n^{\mathbf{YY}}\mathbf{K}_n^{\mathrm{T}}.\end{aligned} \tag{2.22}$$

Eq. (2.18), Eq. (2.21), and Eq. (2.22) show that $\mathbf{K}_n$, and $\mathbf{P}_n$ are calculated using the $\mathbf{P}_n^{\mathbf{XX}}$, $\mathbf{P}_n^{\mathbf{YY}}$, and $\mathbf{P}_n^{\mathbf{XY}}$ in each iteration. The $\mathbf{P}_n^{\mathbf{XX}}$, $\mathbf{P}_n^{\mathbf{YY}}$, and $\mathbf{P}_n^{\mathbf{XY}}$ can be calculated using the sigma points calculated from Eqs. (1.1) - (1.3) in each iteration of the Kalman filtering. The sigma points are propagated through the transition and measurement functions in each iteration. Therefore, the Kalman filtering process would be viable for any arbitrary nonlinear transition and measurement functions within a derivative-free process (UKF or CKF).

2.3. **Normality assumption**

This study assumed that the measured data, process noise, and measurement noise follow the normal distribution. Normality assumption improves the efficiency of the Kalman filtering process and simplifies the filtering algorithm. Furthermore, based on the central limit theorem, a large variety of statistical data can be approximated with a Gaussian distribution [29]. However, this assumption is not valid for many engineering problems. Some other methods have been developed to estimate desired parameters for non-Gaussian data.

For example, the particle filter is a Monte Carlo-based recursive Bayesian method that does not have a normality assumption and estimates posterior distribution with a group of weighted samples. Increasing the number of samples improves the convergence of the estimated parameters to the ground values. However, particle filter-based methods are computationally extensive, and they are not applicable for systems with a large number of states [35].

Another approach could be a general Bayesian method that considers any type of distribution. This approach does not generally lead to a closed-form distribution function, and different sampling methods should be used to estimate the desired parameters from posterior distribution [40]. Again, these approaches are computationally extensive and need many samples to pass the burn-in step and converge to a clean response.

Skewed Kalman filtering is an extension to the Kalman filtering-based method, which introduces a skewness to the measured data and noise incorporated in the state-space model. The skew-normal distribution assumption increases the applicability of the Kalman filtering methods for a broader range of systems. However, the skewed Kalman filtering has a complicated algorithm compared with the general Kalman filter [41].

In this dissertation, the UKF is widely used for damage quantification. The UKF can capture the mean and variance of the posterior distribution accurately up to the 3^{rd} order of the Taylor series expansion, assuming Normal distribution for any arbitrary nonlinear function. However, the estimation accuracy decreases to the 2^{nd} order of the Taylor series expansion for non-Gaussian distributions. Comparing the skewed UKF and general UKF

reveals that the two methods have almost the same accuracy in estimation for small sampling rate values [42]. As it has been tried to choose small values for the sampling rates of numerical and experimental case studies, the normality assumption is reasonable enough to catch a clean response.

2.4. **Conclusion**

The mathematical background of the linear Kalman filter and the initial assumptions involved in its derivation process are introduced in this chapter. Following that, the extended Kalman filter is presented, which works based on Taylor series linearization. Derivative-free Kalman filtering is developed to compensate for the drawbacks of the extended Kalman filter. The mathematical basics of derivative-free Kalman filtering are presented in this section as well. The unscented Kalman filter and the cubature Kalman filter are the two most frequently used derivative-free Kalman filters and are able to estimate the desired states of nonlinear systems, but increasing the number of unknown states weakens their estimation accuracy. Additionally, an unknown input (excitation) will make the situation worse. The challenges associated with these derivative-free estimation methods are the subject of interest in this study. Some information about the Normality assumption of the data is given, and the main reason associated with this assumption is explained.

Chapter Three:

An Iterated Cubature Unscented Kalman Filter for Large-DoF Systems Identification with Noisy Data

This chapter allocates to the paper published in the peer-reviewed *Journal of Sound and Vibration*[1] introduced in the Co-authorship section. The paper improves the performance of the UKF for systems with a large number of states. In the beginning, the mathematical basics of the UKF and the CKF are presented. Following that, it will be explained how the sigma points of the UKF and the CKF are combined to improve the performance of the solo UKF or CKF. The convergence of the proposed method is assured by additional convergence criteria. The method is verified with extensive numerical simulation studies using linear and nonlinear models. Followed by the paper abstract in the next paragraph, the paper's detailed explanations are presented in this chapter.

---

1 **E. Ghorbani**, and Y. J. Cha, "*Iterated cubature unscented Kalman filter for large-DoF systems identification with noisy data",* Journal of Sound and Vibration, 420, 21-34, (2018).

Abstract, Structural and mechanical system identification under dynamic loading has been an important research topic over the last three or four decades. Many Kalman-filtering-based approaches have been developed for linear and nonlinear systems. For example, to predict nonlinear systems, an unscented Kalman filter was applied. However, from extensive literature reviews, the unscented Kalman filter still showed weak performance on systems with large degrees of freedom. In this research, a modified unscented Kalman filter is proposed by the integration of a cubature Kalman filter to improve the system identification performance of systems with large degrees of freedom. The novelty of this work lies in conjugating the unscented transform with the cubature integration concept to find a more accurate output from the transformation of the state vector and its related covariance matrix. To evaluate the proposed method, three different numerical models (i.e., the single-degree-of-freedom Bouc–Wen model, the linear 3-degrees-of-freedom system, and the 10-degrees-of-freedom system) are investigated. To evaluate the robustness of the proposed method, high levels of noise in the measured response data are considered. The results show that the proposed method is significantly superior to the traditional UKF for noisy measured data in systems with large degrees of freedom.

3.1. **Introduction**

Many aerospace, civil, and mechanical engineering systems are used despite their ageing and the associated potential for damage accumulation. It is clear that degradation and the process of replacing infrastructure cost billions of dollars and has many other inevitable impacts. This presents a potential for research in this field to develop systems that detect damage in the initial stages. A linear Kalman filter was developed to track system states by compensating noisy data in the 1960s by Kalman and Kalman and Bucy [24]. It showed remarkable results in the identification of dynamic specifications when there is a linear assumption for a mathematical model, while the state vector dimension is limited.

The Kalman filter prediction accuracy decreases drastically when systems are assumed as linear by omitting their nonlinear nature. The extended Kalman filter (EKF) has been developed that works based on the first-order linearization of the mathematical model using

the Taylor series [17, 37, 38]. There are other techniques, such as the Monte Carlo method, which can be used for nonlinear systems, but they often require a large amount of data and are, therefore, computationally expensive [43]. The EKF as a standard local filter (using the standard linearization method) is a suitable technique that is used to identify mechanical systems [17, 44-46]. However, it has two significant problems that limit its applications in high nonlinear systems and systems with large degrees-of-freedom (DoF) systems and high loading [26, 29]. The first problem is that the EKF uses Taylor expansion for the first-order linearization. Therefore, the calculation of the Jacobian and Hessian matrix of the transition and measurement matrices is unavoidable, which is sometimes impossible or very complicated in some cases. Second, when the system has a high order of nonlinearity, the first-order linearization leads to divergence, and the accuracy of the predicted responses decreases significantly. To resolve these drawbacks, other kinds of filters are introduced that do not use the Taylor series expansion and are derivation free.

With the background knowledge of stochastic filtering, Bayesian statistics, and Monte Carlo techniques, the sequential Monte Carlo approach, also known as the particle filter (PF), is a useful technique for system identification [47]. This technique handles both nonlinearity in the posterior distribution of states as well as systems with non-Gaussian noises. To deal with unknown input systems, the PF is used for joint parameter and state estimation, and many developments are achieved using the PF in structural health monitoring [48]. Refer to [25], although PF techniques are more robust than the UKF, in real-time simulation, the UKF is significantly faster and more efficient.

The unscented Kalman filter (UKF) is a local derivation-free filter that transforms the posterior error covariance matrix of states instead of the transition and measurement matrix [28]. It can be shown that when data have a Gaussian distribution, the UKF prediction is equal to the third order of the Taylor series. The UKF uses symmetric points around the mean, which are named sigma points and are propagated with the nonlinear transition and measurement matrix function. They capture the true mean and covariance up to the second order for any level of nonlinearity. If the prior (initial distribution) distribution is Gaussian distribution, the posterior mean and covariance are accurate to the third order for any nonlinearity [23]. Considering the robustness of the UKF, several studies have focused on

system identification [49]. Some researchers have attempted to develop methods for worse cases (high order of nonlinearity and severe loading) to improve their convergence rate [50], for the parameter identification of materials in finite element models [51], for the identification of noise adaptive models in a joint state and parameter estimation scheme [52], for damage detection purposes [53], and when the input is unknown [54-57]. Further, the most recent studies have integrated the UKF with the computer vision technique [58]. An extensive review of the published papers shows that no comprehensive studies have proposed the UKF for large-DoF systems with high levels of noisy measured data.

The main purpose of this study is to develop an UKF-based system identification method for large-DoF systems with noisy measured acceleration. The contents of this paper are divided as follows. The central concept of the UKF is explained briefly in section 3.2.1, and a modified UKF is proposed in section 3.2.2, which uses another sigma point calculation step during the recursive process. The main concept of the proposed method is a combination of cubature integration and unscented transform in the sigma point calculation process. Further, the propagation of new sigma points over the transition and measurement matrix is integrated with the iterated UKF to improve the accuracy of state prediction, as discussed in section 3.2.3. Section 3.3 presents three different numerical models for evaluating the performance of the newly proposed methods with noisy data in contrast to the traditional UKF.

3.2. **UKF-based system identification methods**

In this section, a quick review of the UKF is presented with a flowchart of the algorithm given in section 3.2.1. This flowchart is useful for comparison with the newly proposed method introduced in section 3.2.2. The modified UKF is proposed by the integration of the UKF and cubature Kalman filter. It is also adapted with the iterated Kalman filter, leading to more accurate state prediction, as shown in section 3.2.3.

3.2.1. Original UKF

The UKF was initially developed to overcome the limitation of the EKF in the linearization process of the mathematical model of a system using derivation-free local filters by an unscented transform (UT). The UT is found based on the fact that it is easier to approximate a probability distribution than an arbitrary nonlinear function or transformation [28]. A set of deterministically weighted points, which have an identical sample mean and sample covariance, named sigma points, are chosen so that their posterior mean and covariance are calculated over the propagated nonlinear transition and measurement functions. To determine the sigma points and related weights, Eqs. (3.1) - (3.3) must be solved, considering that the initial states mean is $\mathbf{m}$ and its covariance error matrix is $\mathbf{P}_0$:

$$\sum_{i=0}^{2n} w_i = 1, \tag{3.1}$$

$$\sum_{i=0}^{2n} w_i \chi_i = \mathbf{m}, \tag{3.2}$$

$$\sum_{i=0}^{2n} w_i (\chi_i - \mathbf{m})(\chi_i - \mathbf{m})^T = \mathbf{P}_0, \tag{3.3}$$

where χ is a sigma point, w is the weight, and n is the number of states. The most common solution, sigma points, of the above three equations are given below.

$$\begin{aligned} \chi_0 &= \mathbf{m} \\ \chi_i &= \mathbf{m} + \sqrt{((n+\lambda)\mathbf{P}_0)}_i \qquad i = 1,2,....,n \\ \chi_i &= \mathbf{m} - \sqrt{((n+\lambda)\mathbf{P}_0)}_{i-n} \qquad i = n+1, n+2,....,2n \end{aligned} \tag{3.4}$$

where λ is a scaling parameter, and i index is a column vector number. To calculate the square root of the $\mathbf{P}$ matrix, based on linear algebra, there is a $\mathbf{V}$ as lower unit triangular (unit triangular) matrix and $\mathbf{D}$ a diagonal matrix, as shown below:

$$\mathbf{P}=\mathbf{VDV}^{-1}=\mathbf{V}\begin{bmatrix} D_1 & \cdots & \cdots & 0 \\ \vdots & \ddots & & \vdots \\ \vdots & & \ddots & \vdots \\ 0 & \cdots & \cdots & D_n \end{bmatrix}\mathbf{V}^{-1}=\mathbf{V}\begin{bmatrix} \sqrt{D_1} & \cdots & \cdots & 0 \\ \vdots & \ddots & & \vdots \\ \vdots & & \ddots & \vdots \\ 0 & \cdots & \cdots & \sqrt{D_n} \end{bmatrix}^2\mathbf{V}^{-1}, \tag{3.5}$$

where $\mathbf{S}$ can be defined as

$$\mathbf{S}=\mathbf{V}\begin{bmatrix} \sqrt{D_1} & \cdots & \cdots & 0 \\ \vdots & \ddots & & \vdots \\ \vdots & & \ddots & \vdots \\ 0 & \cdots & \cdots & \sqrt{D_n} \end{bmatrix}\mathbf{V}^{-1}, \tag{3.6}$$

and

$$\mathbf{SS}=(\mathbf{VD}^{\frac{1}{2}}\mathbf{V}^{-1})((\mathbf{VD}^{\frac{1}{2}}\mathbf{V}^{-1})=\mathbf{VDV}^{-1}=\mathbf{P}. \tag{3.7}$$

In sum, Cholesky decomposition is a stable numerical method that is used for UKF implementation, considering that the eigenvectors of the $\mathbf{P}$ and $\mathbf{S}$ matrices are the same. The weakness of this decomposition technique is that the $\mathbf{P}$ matrix must be positive definite. With the sigma points, the weighting functions can be calculated, as shown below:

$$\begin{aligned} w_0^m &= \frac{\lambda}{n+\lambda}, \\ w_0^c &= \frac{\lambda}{n+\lambda}+\left(1-\alpha^2+\beta\right), \\ w_i^m &= w_i^c = \frac{1}{2\left(n+\lambda\right)}, \quad i=1,\ldots,2n, \end{aligned} \tag{3.8}$$

$$\lambda=\alpha^2(n+\kappa)-n, \tag{3.9}$$

Where α determines the spread of sigma points and is a positive number $(0 \le \alpha \le 1)$, κ a secondary scaling parameter which is usually equals to $3-\mathrm{n}$. $\beta = 2$ is optimal for Gaussian distributions.

The transition function of a continuous system in a general form of a state-space model can be defined as follows:

$$\dot{\mathbf{X}} = \mathrm{f}(\mathbf{X}(\mathrm{t}), \mathbf{u}(\mathrm{t}), \mathbf{w}(\mathrm{t})), \tag{3.10}$$

and the measurement function is

$$\mathbf{Y}(\mathrm{t}) = \mathrm{h}(\mathbf{X}(\mathrm{t}), \mathbf{u}(\mathrm{t}), \mathbf{v}(\mathrm{t})), \tag{3.11}$$

where $\mathbf{u}(\mathrm{t})$ is the input, and $\mathbf{w}(\mathrm{t})$, and $\mathbf{v}(\mathrm{t})$ are the process noise vector and measurement noise vector, respectively. To implement the UKF, the above equations must be rewritten in discrete time with observation $\mathrm{t} = \mathrm{k}\Delta\mathrm{t}$,

$$\mathbf{X}_{\mathrm{k+1,k}} = \mathrm{F}(\mathbf{X}_{\mathrm{k}}, \mathbf{u}_{\mathrm{k}}, \mathbf{w}_{\mathrm{k}}), \tag{3.12}$$

$$\mathbf{Y}_{\mathrm{k}} = \mathrm{H}(\mathbf{X}_{\mathrm{k+1,k}}, \mathbf{u}_{\mathrm{k}}, \mathbf{v}_{\mathrm{k}}), \tag{3.13}$$

where k is a time step, $\mathbf{X}_{\mathrm{k}}$ is a state variable vector, $\mathbf{w}_{\mathrm{k}}$ is a discrete process white noise, $\mathbf{Q}$ is its covariance matrix, $\mathbf{Y}_{\mathrm{k}}$ is the measurement vector, $\mathbf{v}_{\mathrm{k}}$ is a discrete measurement process noise vector, and $\mathbf{R}$ is its covariance value, and

$$\mathrm{F}(\mathbf{X}_{\mathrm{k}}, \mathbf{u}_{\mathrm{k}}, \mathbf{w}_{\mathrm{k}}) = \mathbf{X}_{\mathrm{k}} + \int_{\mathrm{k}\Delta\mathrm{t}}^{(\mathrm{k}+1)\Delta\mathrm{t}} \mathrm{f}(\mathbf{X}(\mathrm{t}), \mathbf{u}(\mathrm{t}), \mathbf{w}(\mathrm{t}))\mathrm{dt}\ , \tag{3.14}$$

where F is the transition matrix function in the discrete domain, and $\mathbf{X}$ is the state variable vector. The above integral can be solved using numerical methods, and here is solved using the Euler method. For each time step k, the UKF procedure is presented in Figure 3-1 below, and more details can be found in [28].

$$\boldsymbol{\chi}_{k+1|k} = \mathrm{F}\left(\boldsymbol{\chi}_k, \mathbf{u}_k\right) \quad (3.15)$$

$$\hat{\mathbf{X}}_{k+1}^{-} = \sum_{i=0}^{2n} w_i^m \boldsymbol{\chi}_{i,k+1|k} \quad (3.16)$$

$$\mathbf{P}_{k+1}^{XX} = \sum_{i=0}^{2n} w_i^c \left[\boldsymbol{\chi}_{i,k+1|k} - \hat{\mathbf{X}}_{k+1}^{-}\right]\left[\boldsymbol{\chi}_{i,k+1|k} - \hat{\mathbf{X}}_{k+1}^{-}\right]^T + \mathbf{Q}_k \quad (3.17)$$

$$\mathbf{i}_{k+1|k} = \mathrm{H}\left(\boldsymbol{\chi}_{k+1|k}, w_k\right) \quad (3.18)$$

$$\mathbf{Y}_{k+1}^{-} = \sum_{i=0}^{N} w_i^m \Upsilon_{i,k+1|k} \quad (3.19)$$

$$\mathbf{P}_{k+1}^{YY} = \sum_{i=0}^{2n} w_i^c \left[\Upsilon_{i,k+1|k} - \hat{\mathbf{Y}}_{k+1}^{-}\right]\left[\Upsilon_{i,k+1|k} - \hat{\mathbf{Y}}_{k+1}^{-}\right]^T + \mathbf{R}_k \quad (3.20)$$

$$\mathbf{P}_{k+1}^{XY} = \sum_{i=0}^{2n} w_i^c \left[\boldsymbol{\chi}_{i,k+1|k} - \hat{\mathbf{X}}_{k+1}^{-}\right]\left[\Upsilon_{i,k+1|k} - \hat{\mathbf{Y}}_{k+1}^{-}\right]^T \quad (3.21)$$

$$\mathbf{K}_{k+1} = \mathbf{P}_{k+1}^{XY}\left(\mathbf{P}_{k+1}^{YY}\right)^{-1} \quad (3.22)$$

$$\hat{\mathbf{X}}_{k+1} = \hat{\mathbf{X}}_{k+1}^{-} + \mathbf{K}_{k+1}\left(\mathbf{y}_{k+1} - \hat{\mathbf{Y}}_{k+1}^{-}\right) \quad (3.23)$$

$$\mathbf{P}_{k+1} = \mathbf{P}_{k+1}^{XX} - \mathbf{K}_{k+1}\mathbf{P}_{k+1}^{YY}\mathbf{K}_{k+1}^T \quad (3.24)$$

$\mathbf{P}_{k+1}$ and $\hat{\mathbf{X}}_{k+1}$ will be used for the next iteration to calculated new sigma points.

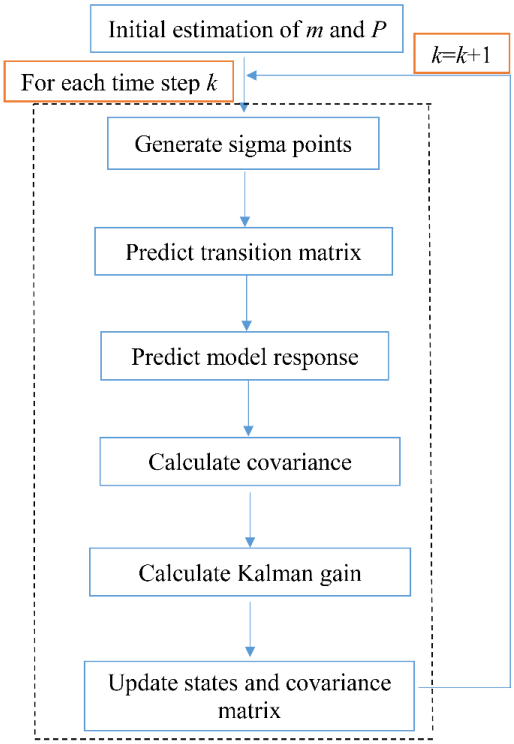

Figure 3-1: UKF algorithm (left) and a simple flowchart (right)

3.2.2. Modified UKF

In section 3.2.1, the original UKF algorithm and its concept were explained with its flowchart. This section mainly presents the improvement of the UKF to obtain more accurate results for large-DoF systems while noisy data are measured.

In this paper, the original UKF approach is integrated with the cubature Kalman filter (CKF) [29] in the sigma point calculation step, and the transformed sigma points from the transition matrix function are rearranged by another scaling parameter in the process to improve the performance of the UKF for large-DoF systems with noisy measured acceleration response. CKF is a nonlinear filter that can be applied to solve a wide range (from low to large dimensions) of nonlinear systems. It is a non-product rule (i.e., uses equals

weights for specific points to carry out numerical integration) that yields reasonable accuracy and is easily extendable to arbitrarily large-dimensional systems [29]. In the cubature integration, 2*n* equal weight spherical points (*n* is the number of function variables) are used for the numerical calculation of $\int f(y)dy$, in which $f(y)$ is an arbitrary function. These constant weights, which are independent of $f(y)$, reduce the computational cost and also provide more accurate numerical results than the UKF due to the lower rand-off error for large-DoF systems [59]. However, in the UKF, there is no guarantee of consistently having positive weights, which can lead to negative covariance matrix; this can lead to some instability in the filter while the CKF weights are always positive.

In the CKF, the fully symmetric spherical-radial cubature points and non-negative weights are selected in a way that yields the required accuracy for the first and second momentum of the posterior. The placement of the UKF sigma points and the CKF predefined points are shown in Figure 3-2. There are more points distributed around the mean point, whilst the CKF points are closer to it. In addition, as mentioned above, the CKF weights are always positive, and considering that its points are also closer to the mean point, the probability of convergence increases, as negative weights can be a reason for divergence. Using the advantages of the both techniques at the same time is the main reason for merging of these two techniques, which leads to a higher convergence rate.

Therefore, in this paper, using the advantages of the CKF to improve the performance of the UKF, an efficient cubature unscented filter is derived to have more sigma points, which are employed in the propagation of the transition function. These transformed sigma points are rearranged again to have a more symmetric distribution of the propagated data. To realize this, the modification process contains two parts: the first is the addition of CKF points to the UKF sigma points, and the next one is the rearrangement of the transformed sigma points by another scaling factor within the transition matrix. The conditions mentioned in section 3.2.1 in Eqs. (3.1)–(3.3) must be satisfied with these new sigma points as well.

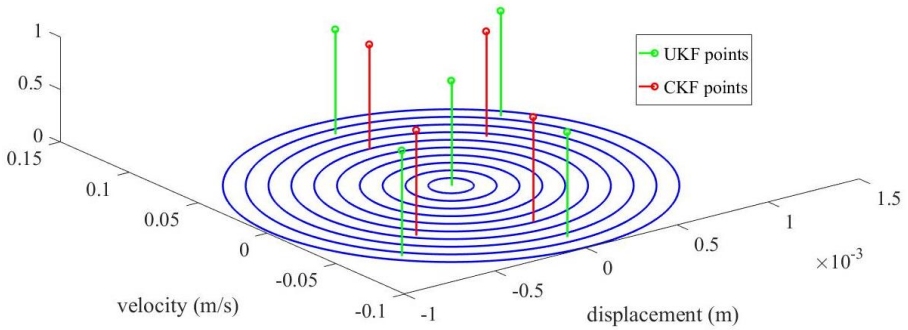

Figure 3-2: The UKF and CKF points' placement

The cubature points are defined in below, considering that $\mathbf{I}$ is a unit $n \times n$ matrix [29], and n is the number of states. First, the matrix $\mathbf{E}$ is defined as shown below:

$$\begin{aligned} \mathbf{E}_i &= \sqrt{(n)} \times \mathbf{I}_i, \qquad i = 1, 2, \cdots, n, \\ \mathbf{E}_i &= -\sqrt{(n)} \times \mathbf{I}_{i-n}, \qquad i = n+1, n+2, \cdots, 2n, \end{aligned} \tag{3.25}$$

where *i* is the column vector index. By using the above $\mathbf{E}$ matrix, the CKF points can be defined as:

$$\chi_i = \mathbf{m} + \sqrt{\mathbf{P}}^{T} \times \mathbf{E}_i, \qquad i = 1, 2, 3, \cdots, 2n, \tag{3.26}$$

where $\mathbf{m}$ and $\mathbf{P}$ are the state matrix and the covariance matrix, respectively. The related weights of each sigma point are:

$$w_i = \frac{1}{2(n)}, \qquad i = 1, 2, 3, \cdots 2n. \tag{3.27}$$

In the modification process, the UKF and CKF points are used together to have more predetermined points. This means that there will be $4n+1$ points (i.e., $2n+1$ from UKF and $2n$ from CKF) as sigma points, which leads to more points for the calculation of the means and covariance of states. In addition, for the new method, the summation of weighting functions and the weighted means must equal one and the predicted mean from the previous step, respectively. To achieve these conditions, some modifications of the cubature points

are required when they are mixed with the UKF sigma points to satisfy Eqs. (3.1)–(3.3); then, the new sigma points can be defined as

$$\begin{aligned}
&\boldsymbol{\chi}_0 = \mathbf{m}, \\
&\boldsymbol{\chi}_i = \mathbf{m} + \sqrt{\left((n+\lambda)\mathbf{P}_0\right)}_i, && i = 1, 2, ..., n, \\
&\boldsymbol{\chi}_i = \mathbf{m} - \sqrt{\left((n+\lambda)\mathbf{P}_0\right)}_{i-n}, && i = n+1,\ n+2, ...,\ 2n, \\
&\boldsymbol{\chi}_i = \mathbf{m} + \sqrt{\mathbf{P}_0}^{T} \times \mathbf{E}_i^c, && i = 2n+1,\ 2n+2, \cdots,\ 4n+1,
\end{aligned} \tag{3.28}$$

where $\mathbf{E}^c$ is defined as

$$\begin{aligned}
&\mathbf{E}_i^c = \sqrt{(n)} \times \mathbf{I}_i, && i = 2n+1, 2, \cdots, 3n, \\
&\mathbf{E}_i^c = -\sqrt{(n)} \times \mathbf{I}_i, && i = 3n+1, n+2, \cdots, 4n+1,
\end{aligned} \tag{3.29}$$

and the corresponding weighting functions are given as

$$\begin{aligned}
&w_0^m = \frac{\lambda}{(n+\lambda)}, \\
&w_0^c = \frac{\lambda}{(n+\lambda)} + \left(1 - \alpha^2 + \beta\right), \\
&w_i^m = w_i^c = \frac{1}{4(n+\lambda)}, \quad i = 1, \ldots, 2n, \\
&w^{c,m}{}_i = \frac{1}{4(n+\lambda)}, && i = 2n+1,\ 2n+2,\ 2n+3, \cdots,\ 4n+1,
\end{aligned} \tag{3.30}$$

$$\lambda = \alpha^2 (n + \kappa) - n. \tag{3.31}$$

This modified UKF (MUKF) is explained in Figure 3-3 through both formulation and a flowchart.

$$\boldsymbol{\chi}_{k+1|k} = \mathrm{F}\left(\boldsymbol{\chi}_k, \mathbf{u}_k\right) \quad (3.32)$$

$$\hat{\mathbf{X}}_{k+1}^{-} = \sum_{i=0}^{4n} \mathrm{w}_i^{m} \boldsymbol{\chi}_{i,k+1|k} \quad (3.33)$$

$$\mathbf{P}_{k+1}^{XX} = \sum_{i=0}^{4n} \mathrm{w}_i^{c} \left[\boldsymbol{\chi}_{i,k+1|k} - \hat{\mathbf{X}}_{k+1}^{-}\right]\left[\boldsymbol{\chi}_{i,k+1|k} - \hat{\mathbf{X}}_{k+1}^{-}\right]^{T} + \mathbf{Q}_k \quad (3.34)$$

Put $\hat{\mathbf{X}}_{k+1}^{-}$ and $\mathbf{P}_{k+1}^{XX}$ with new λ for the sigma point calculation to achieve rearranged transition matrix points, which are $\boldsymbol{\chi}_{k+1|k}^{'}$ and $\mathrm{w}_i^{'}$

$$\Upsilon_{k+1|k} = \mathrm{H}\left(\boldsymbol{\chi}_{k+1|k}^{'}, \mathrm{w}_k^{'}\right) \quad (3.35)$$

$$\mathbf{Y}_{k+1}^{-} = \sum_{i=0}^{N} \left(\mathrm{w}_i^{m}\right)^{'} \Upsilon_{i,k+1|k} \quad (3.36)$$

$$\mathbf{P}_{k+1}^{YY} = \sum_{i=0}^{4n} \left(\mathrm{w}_i^{c}\right)^{'} \left[\Upsilon_{i,k+1|k} - \hat{\mathbf{Y}}_{k+1}^{-}\right]\left[\Upsilon_{i,k+1|k} - \hat{\mathbf{Y}}_{k+1}^{-}\right]^{T} + \mathbf{R}_k \quad (3.37)$$

$$\mathbf{P}_{k+1}^{XY} = \sum_{i=0}^{4n} \left(\mathrm{w}_i^{c}\right)^{'} \left[\boldsymbol{\chi}_{i,k+1|k}^{'} - \hat{\mathbf{X}}_{k+1}^{-}\right]\left[\Upsilon_{i,k+1|k} - \hat{\mathbf{Y}}_{k+1}^{-}\right]^{T} \quad (3.38)$$

$$\mathbf{K}_{k+1} = \mathbf{P}_{k+1}^{XY}\left(\mathbf{P}_{k+1}^{YY}\right)^{-1} \quad (3.39)$$

$$\hat{\mathbf{X}}_{k+1} = \hat{\mathbf{X}}_{k+1}^{-} + \mathbf{K}_{k+1}\left(\mathbf{y}_{k+1} - \hat{\mathbf{Y}}_{k+1}^{-}\right) \quad (3.40)$$

$$\mathbf{P}_{k+1} = \mathbf{P}_{k+1}^{XX} - \mathbf{K}_{k+1}\mathbf{P}_{k+1}^{YY}\mathbf{K}_{k+1}^{T} \quad (3.41)$$

$\mathbf{P}_{k+1}$ and $\hat{\mathbf{X}}_{k+1}$ will be used for the next iteration to calculate the new sigma points.

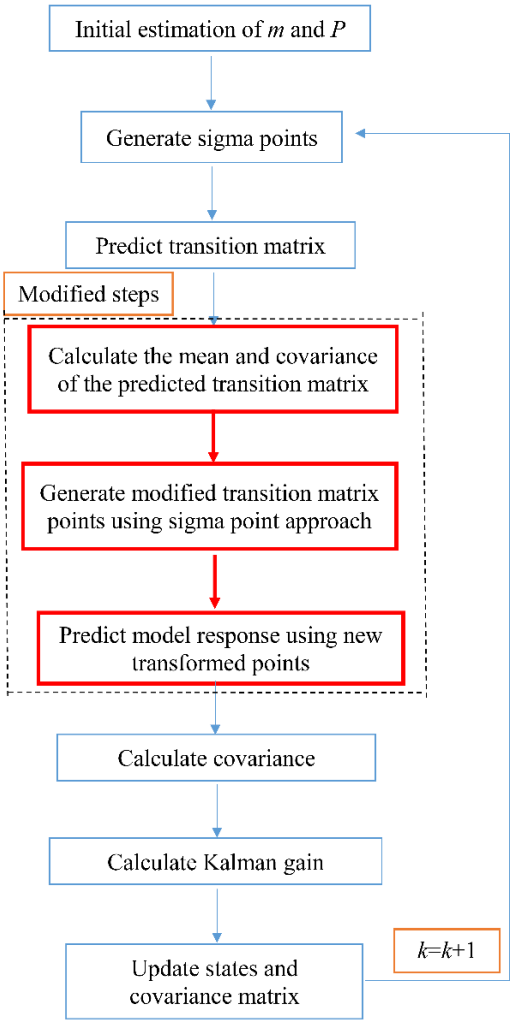

Figure 3-3: MUKF algorithm (left) and a simple flowchart (right)

3.2.3. Iterated MUKF

As explained in section 3.2.2, the UKF and CKF were integrated to reduce the divergence probability. This MUKF can be improved by the iteration of the Kalman filtering process [50]. To iterate the algorithm, an j index is defined for the parameters as follows [50]:

$$\begin{aligned}
&\bar{\mathbf{x}}_{k+1,j-1} = \hat{\mathbf{X}}_{K+1},\\
&\bar{\mathbf{x}}_{k+1,j} = \hat{\mathbf{X}}_{k+1},\\
&\mathbf{P}_{k+1,j-1} = \mathbf{P}^{xx}_{k+1},\\
&\mathbf{P}_{k+1,j} = \mathbf{P}_{k+1}.
\end{aligned} \tag{3.42}$$

For $j = 2$ to N, i.e., the number of iterations, a new iteration-based MUKF is defined as:

1. For Eq. (3.28), $\mathbf{m} = \bar{\mathbf{x}}_{k+1,j-1}$ and $\mathbf{P}_0 = \mathbf{P}_{k+1,j-1}$ sigma points are calculated.

2. Eqs. (3.32)-(3.39) are recalculated.

3. The new state vector in this iteration is calculated as: $\bar{\mathbf{x}}_{k+1,j} = \hat{\mathbf{X}}^{-}_{k+1,j-1} + G \times \mathbf{K}_{k+1}\left(\mathbf{y}_{k+1} - \hat{\mathbf{Y}}^{-}_{k+1,j-1}\right)$ instead of Eq. (3.40), where G is equal to one in the first iteration and is reduced based on η in each iteration and η is the reduced rate, which is $0 < \eta < 1$.

4. The following parameters are calculated to check the inequality:

$$\begin{aligned}
&\hat{\mathbf{y}}_{k+1,j} = h(\bar{\mathbf{x}}_{k+1,j}),\\
&\tilde{\mathbf{x}}_{k+1,j} = \bar{\mathbf{x}}_{k+1,j} - \bar{\mathbf{x}}_{k+1,j-1},\\
&\tilde{\mathbf{y}}_{k+1,j} = \mathbf{y}_{k+1,j} - \hat{\mathbf{y}}_{k+1,j},
\end{aligned} \tag{3.43}$$

5. The following inequality is defined:

$$\tilde{\mathbf{x}}^{T}_{k+1,j}\mathbf{P}^{-1}_{k+1,j-1}\tilde{\mathbf{x}}_{k+1,j} + \tilde{\mathbf{y}}^{T}_{k+1,j}\mathbf{R}^{-1}_{k+1,j}\tilde{\mathbf{y}}_{k+1,j} < \tilde{\mathbf{y}}^{T}_{k,j-1}\mathbf{R}^{-1}_{k+1,j}\tilde{\mathbf{y}}_{k,j-1}. \tag{3.44}$$

6. For each iteration $j = j+1$, and $G = \eta G$. The iteration continues until the above inequality is satisfied and $j \le N$.

3.3. **Numerical examples**

The UKF was presented in the previous section with its limitations. To overcome the drawbacks, this paper proposed a modified UKF integrated with the CKF, referred to as MUKF, and the IMUKF method was also proposed to improve the MUKF approaches when dealing with large-DoF systems and noisy measured data. The main idea of the MUKF is that it uses symmetrical points calculated from the UKF and CKF and rearranges the covariance cloud around the mean value of the state vector. The proposed MUKF was also combined with the iterated Kalman filtering process to improve the accuracy of the state prediction.

To test the proposed method, three different system models are used to compare the results between the proposed methods along with the original UKF approach for predicting the system states. For the first problem, a nonlinear system model using a Bouc–Wen hysteretic formulation is employed with a high level of noise, and then linear 3-DoF and 10-DoF systems with a high level of noise are used to evaluate the proposed method. To validate the performance of the proposed method, the methods are first compared when there is a low level of noise and are then tested with a high level of noise.

3.3.1. Bouc–Wen hysteretic model

The proposed method, including the traditional UKF, is tested on a single-DoF Bouc–Wen model subject to EI Centro earthquake ground motion with a high level of noise in the measured acceleration response. The Bouc–Wen mathematical model is written below:

$$m\ddot{x}(t) + c\dot{x}(t) + r(t) = -ma_g, \tag{3.45}$$

where m, c, and a_g are the mass, damping coefficient, and earthquake ground acceleration, respectively, and $r(t)$ is the Bouc–Wen hysteretic component expressed as

$$r(t) = \alpha k_e x(t) + (1-\alpha) k_e x_y z_{BW}(t), \tag{3.46}$$

Further,

$$\dot{z}_{BW}(t) = \frac{1}{x_y}(-\gamma |\dot{x}(t)||z_{BW}|^{n-1} z_{BW}(t) - \beta \dot{x}(t)|z_{BW}(t)|^n + A\dot{x}(t)). \tag{3.47}$$

where $k = 50000$ N/m, $c = 300$ N.s/m, $m = 500$ kg, $\alpha = 0.1$, $x_y = 0.01$, $\gamma = 0.45$, $\beta = 0.55$, $n = 2$, and $A = 1$ are chosen for the simulations. A duration of 50 s of the EI Centro earthquake acceleration record, as shown in Figure 4, is used in this example.

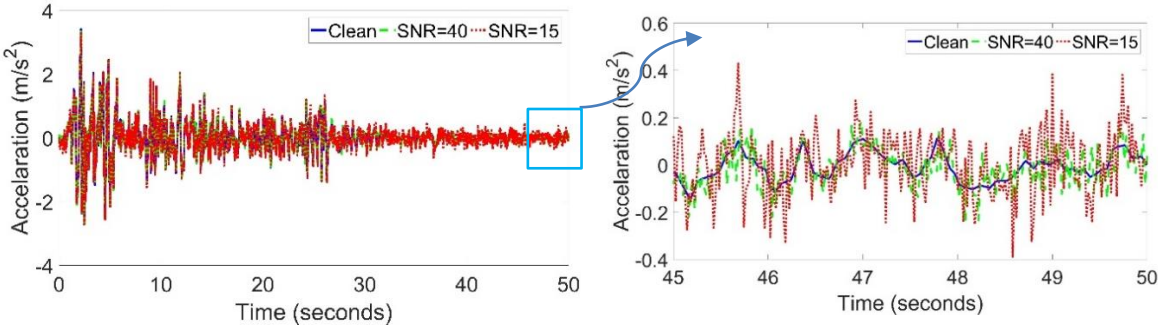

Figure 3-4: EI Centro earthquake ground motion: (a) clean and noisy signals (two different SNRs of 40 and 15) and (b) a detailed view of the signals.

The state vector is defined as follows:

$$\mathbf{X} = \{x_1 \quad x_2 \quad x_3 \quad x_4 \quad x_5 \quad x_6 \quad x_7 \quad x_8\}^T = \{x \quad \dot{x} \quad \ddot{x} \quad z \quad k \quad c \quad \gamma \quad \beta\}^T \tag{3.48}$$

where x, $\dot{x}$, and $\ddot{x}$ are the displacement, velocity, and acceleration responses, respectively. The system transition and measurement matrix are defined as shown below in the continuous form:

$$\dot{\mathbf{X}} = \begin{bmatrix} x_2 \\ x_3 \\ 0 \\ \left(\left(\frac{1}{x_y}\right)\cdot x_7 |x_2||x_4|^{n-1} x_4 - x_8 x_2 |x_4|^n + A x_2\right) \\ 0 \\ 0 \\ 0 \\ 0 \end{bmatrix} = f(x,t) + \boldsymbol{\omega}(t), \tag{3.49}$$

$$y = h(x,t) + v(t) = -a_g - \frac{1}{m}(x_6 x_2 + \alpha \cdot x_1 x_5 + (1-\alpha) x_5 \cdot x_y \cdot x_4) + v(t). \tag{3.50}$$

To express the robustness of the proposed method for noisy data, white noise with SNR 40 and 15 is added to the measured acceleration. The *SNR* is defined as $\mathrm{SNR} = \frac{P_{signal}}{P_{noise}} = \frac{A^2_{signal}}{A^2_{noise}}$ where $P_x = \int_0^t A^2(t)dt,$ and A is the root mean square (RMS) of the amplitude. The EI Centro ground motion accelerations with two white noise levels (i.e., SNRs of 40 and 15) from seconds 45 to 50 are shown in Figure 3-4.

Considering the above equations, the system is simulated in the MATLAB Simulink Toolbox and the system response is recorded using the fourth-order Runge-Kutta numerical technique with initial values $m = 500$ kg, $k = 30000$ N/m, $c = 200$ N.s/m, $\alpha = 0$, $x_y = 0$, $\gamma = 0,$ and $\beta = 0,$ and the predicted parameters by the UKF and IMUKF are shown in Figure 3-5–Figure 3-7. In Table 3-1 the prediction results of stiffness, damping, γ, β, and hysteresis loop by the UKF and IMUKF are presented and compared. To examine the robustness of the proposed method, two different levels of noise are compared (i.e., SNRs of 40 and 15). In each case, the percentage of measurement and process noise level are the same, but to obtain the best prediction for each filter, the initial covariance matrix estimates are different whilst the initial value of parameters (state vector mean) are the same for both techniques, and the

sampling frequency is set to 500 Hz. The duration for the IMUKF identification is approximately 119 s on a core i7 6700K 4.00 GHz processor.

When SNR = 40, as shown in Figure 3-5(a), there is no noticeable difference between the UKF and IMUKF. However, when SNR = 15, there is a significant difference between the proposed method and the traditional UKF, as shown in Figure 3-5(b). As mentioned above, the initial covariance matrix estimate is different for both techniques to obtain the best prediction for each case.

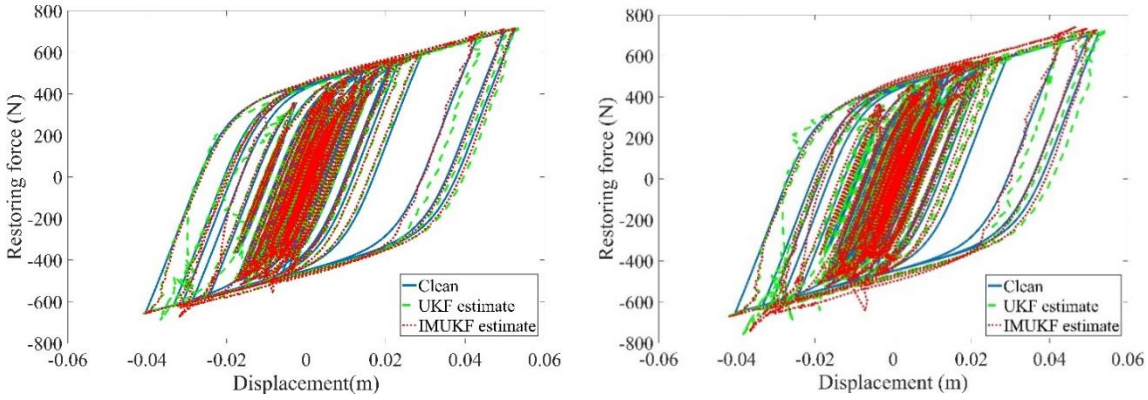

(a) SNR = 40 (b) SNR=15

Figure 3-5: Predicted hysteretic loops

Similar to the case of the hysteresis loop, comparisons are made for the stiffness values between the UKF and IMUKF. No considerable difference can be seen between the two methods in Figure 3-6(a) for SNR = 40, but the discrepancy is significant for SNR = 15, as seen in Figure 3-6(b). Figure 3-7(a) and (b) are related to the prediction of the damping value by the UKF and IMUKF for SNRs of 40 and 15, respectively. The results show that the proposed method provides a more accurate prediction than the traditional UKF at the two different noise levels. A summary of all the predicted parameters of the model is presented in Table 1.

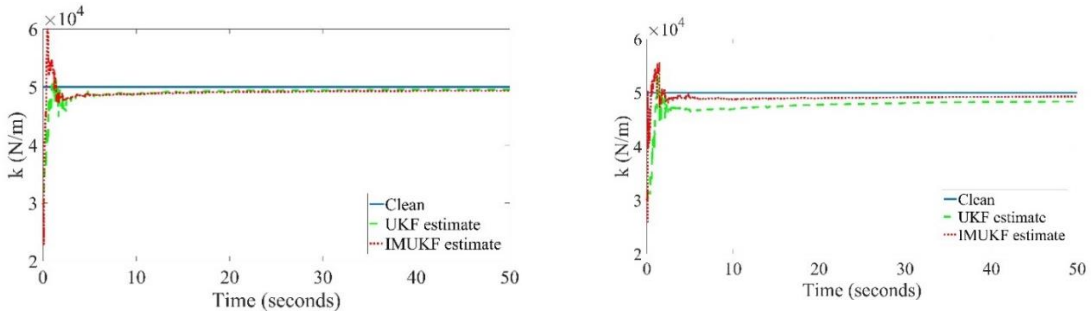

(a) SNR=40 (b) SNR=15

Figure 3-6: Predicted stiffness value

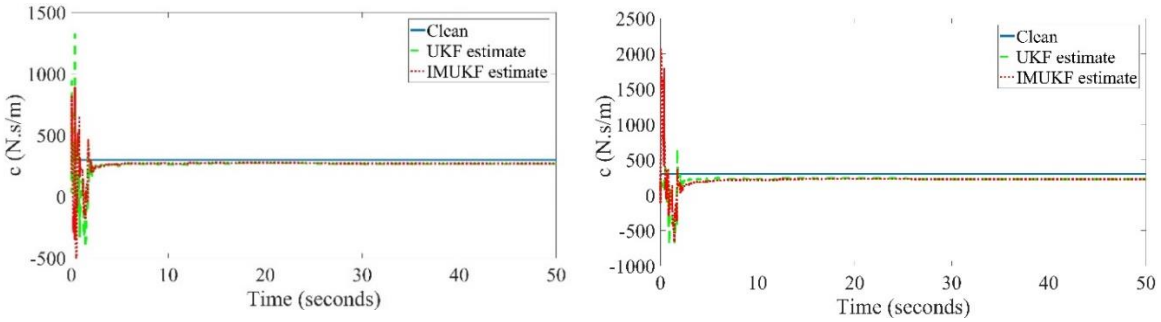

(a) SNR=40 (b) SNR=15

Figure 3-7: Predicted damping coefficient

Table 3-1 Predicted results of the single-DoF nonlinear system using the Bouc–Wen model

	Parameter		m	c	k	β	γ
SNR	Exact values		500	300	50000	0.55	0.45
	Initial values		500	200	30000	1	2
40	UKF	Predicted		265	49500	0.5	0.48
		Error (%)		11%	1%	9%	6%
	IMUKF	Predicted		270	49500	0.49	0.48
		Error (%)		10%	1%	10%	6%

15	UKF	Predicted	230	48200	0.39	0.51
		Error (%)	23%	3%	29%	13%
	IMUKF	Predicted	230	49300	0.43	0.53
		Error (%)	23%	1%	18%	14%

3.3.2. Linear 3-DoF system

In this section, the results of the proposed IMUKF and traditional UKF are compared for a linear 3-DoF system. The 3-DoF state vector $\mathbf{X}$ is expressed as

$$\mathbf{X} = \left\{ x_1 \quad x_2 \quad x_3 \quad x_4 \quad \dot{x}_1 \quad \dot{x}_2 \quad \dot{x}_3 \quad \dot{x}_4 \quad k_1 \quad k_2 \quad k_3 \quad k_4 \quad c_1 \quad c_2 \quad c_3 \quad c_4 \right\}^{\mathrm{T}}.$$

With the known $\mathbf{M}$, and $\mathbf{a}_g$, the governing equation of motion is

$$\mathbf{M}\ddot{\mathbf{x}} + \mathbf{C}\dot{\mathbf{x}} + \mathbf{K}\mathbf{x} = -\mathbf{M}\mathbf{a}_g. \tag{3.51}$$

The governing equation is expressed in a state-space form:

$$\dot{\mathbf{X}} = \begin{Bmatrix} \dot{x}_1 \\ \dot{x}_2 \\ \dot{x}_3 \\ \ddot{x}_1 \\ \ddot{x}_2 \\ \ddot{x}_3 \\ \dot{k}_1 \\ \dot{k}_2 \\ \dot{k}_3 \\ \dot{c}_1 \\ \dot{c}_2 \\ \dot{c}_3 \end{Bmatrix} = \begin{bmatrix} x_4 \\ x_5 \\ x_6 \\ -a_g + [-(x_7 + x_8)x_1 + x_8 x_2 - (x_{10} + x_{11})x_4 + x_{11}x_5]/m_1 \\ -a_g + [x_8 x_1 - (x_8 + x_9)x_2 + x_9 x_3 + x_{11}x_4 - (x_{11} + x_{12})x_5 + x_{12}x_6]/m_2 \\ -a_g + [x_9 x_2 + x_{12}x_5 - (x_{12}x_6 + x_9 x_3)]/m_3 \\ 0 \\ 0 \\ 0 \\ 0 \\ 0 \\ 0 \end{bmatrix} + \boldsymbol{\omega}(t)$$

$$= f(x,t) + \boldsymbol{\omega}(t), \tag{3.52}$$

$$\mathbf{y} = \begin{Bmatrix} \ddot{x}_1 \\ \ddot{x}_3 \end{Bmatrix} = \begin{bmatrix} -a_g + [-(x_7 + x_8)x_1 + x_8 x_2 - (x_{10} + x_{11})x_4 + x_{11}x_5]/m_1 \\ -a_g + [x_9 x_2 + x_{12}x_5 - (x_{12}x_6 + x_9 x_3)]/m_3 \end{bmatrix} + \mathbf{v}(t)$$

$$= h(x,t) + \mathbf{v}(t). \tag{3.53}$$

As measured responses, the absolute accelerations in floors 1 and 3 of the system are used. The sampling frequency of EI Centro ground motion acceleration and the acceleration response measured from the floors are 100 Hz. The duration for the IMUKF identification is approximately 125 s on a core i7 6700K 4.00 GHz processor.

Considering the above equations, the system is simulated in MATLAB with values $m_1 = m_2 = m_3 = 500\,\text{kg}$, $k_1 = k_2 = k_3 = 50000\,\text{N/m}$, and $c_1 = c_2 = c_3 = 300\,\text{N.s/m}$. The initial values for the structural identification are $m = 500$ kg, $k = 30000$ N/m, $c = 200$ N.s/m, and $x = \dot{x} = \ddot{x} = 0$. The simulation results are presented in Figure 3-8 and Figure 3-9.

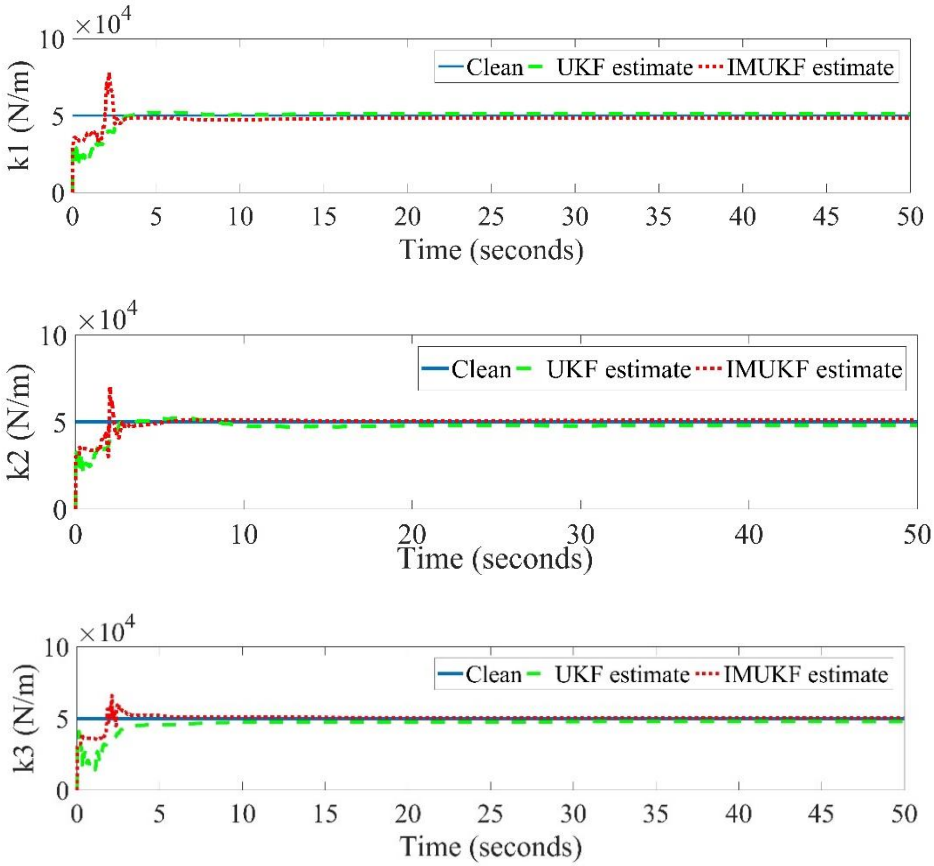

Figure 3-8: Predicted stiffness (k1–k3) values for the 3-DoF system with SNR = 15

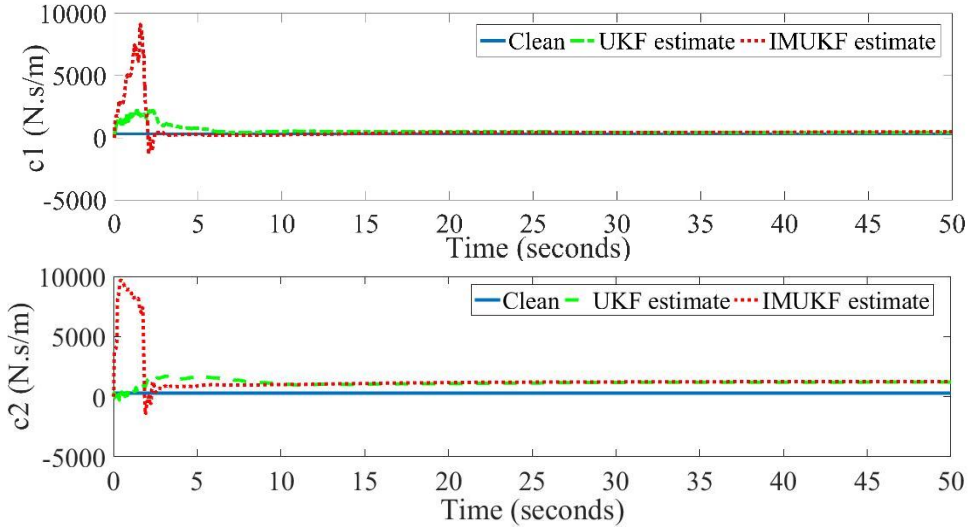

Figure 3-9: Predicted damping coefficient (c1–c3) values for a 3-DoF system with SNR = 15

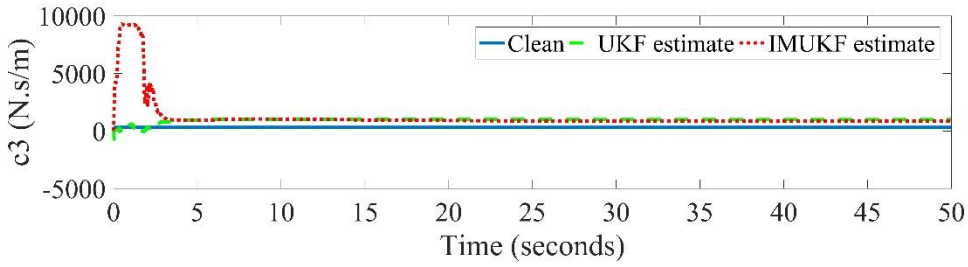

Figure 3-9: Predicted damping coefficient (c1–c3) values for a 3-DoF system with SNR = 15

As can be seen from Figure 3-8 and Figure 3-9, for the 3-DoF system, there is no considerable discrepancy between the results of the proposed method and the traditional UKF. The main reason is that UKF is a strong filter for identification purposes when there is a finite number of states [23, 25, 49, 53]. This example is thus used to compare the results of the UKF when there are different numbers of states (i.e., 12 states for the 3-DoF system and 40 states for the 10-DoF system as the next example) with noisy measured responses.

3.3.3. Linear 10-DoF system

The proposed method is examined for a 10-DoF system with 40 states predicted, which a relatively large DoF system with large states is. The frequency sampling is 100 Hz for both the earthquake ground motion and measured acceleration. The simulation constant values are $m_1 = m_2 \cdots m_{10} = 500$ kg, $k_1 = k_2 \cdots k_{10} = 50000$ N/m, and $c_1 = c_2 \cdots c_{10} = 300$ N.s/m. The predicted values of the stiffness and damping are shown in Figure 3-10 and Figure 3-11, respectively.

The duration for the IMUKF identification is approximately 560 s on a core i7 6700K 4.00 GHz processor. Tuning parameters and initial values are expressed in Appendix A. As mentioned previously, all the parameters are the same except the initial covariance matrices, which are selected in a way that ensures the best prediction for each one.

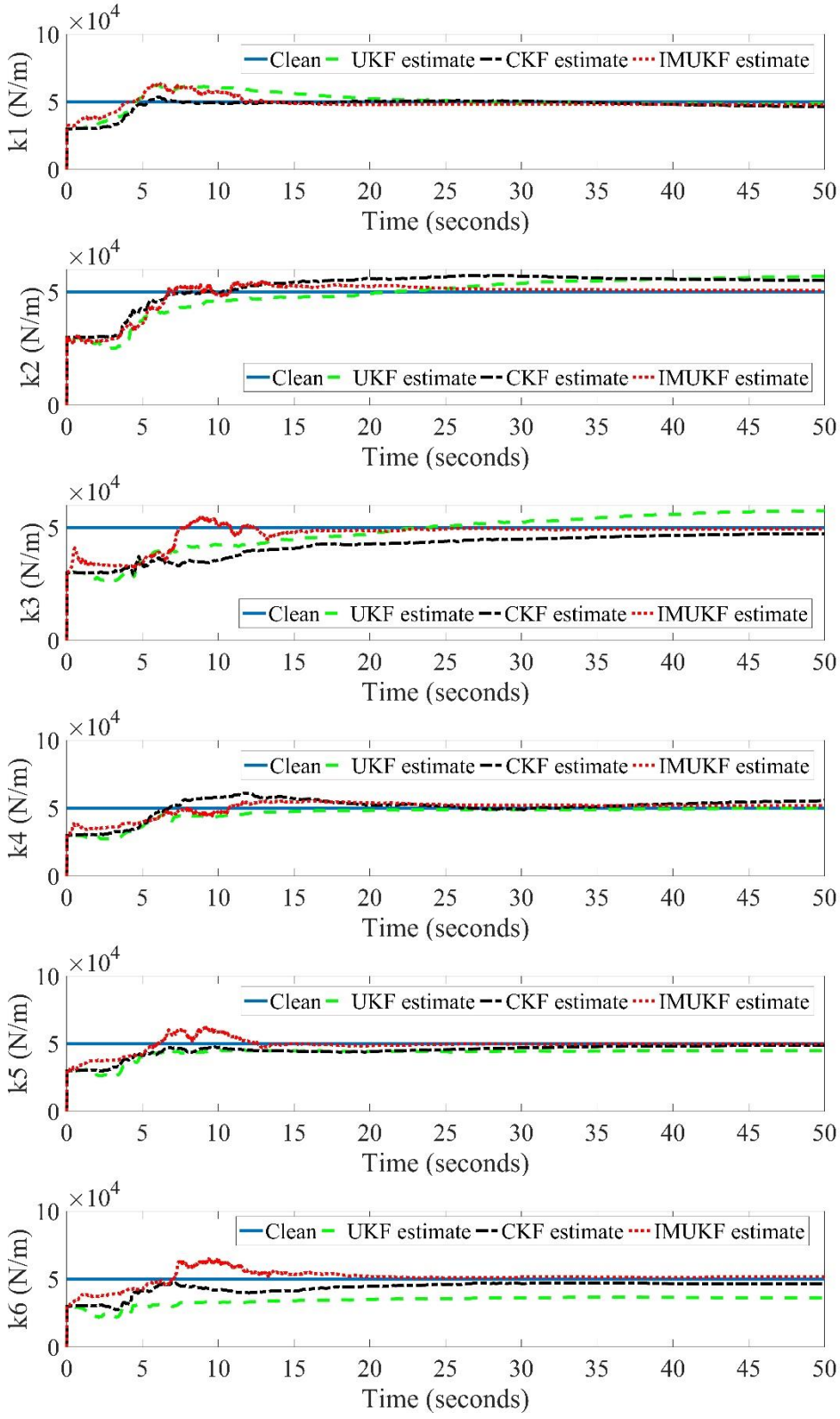

Figure 3-10: Predicted stiffness (k1–k10) values for a 10-DoF system with SNR = 15

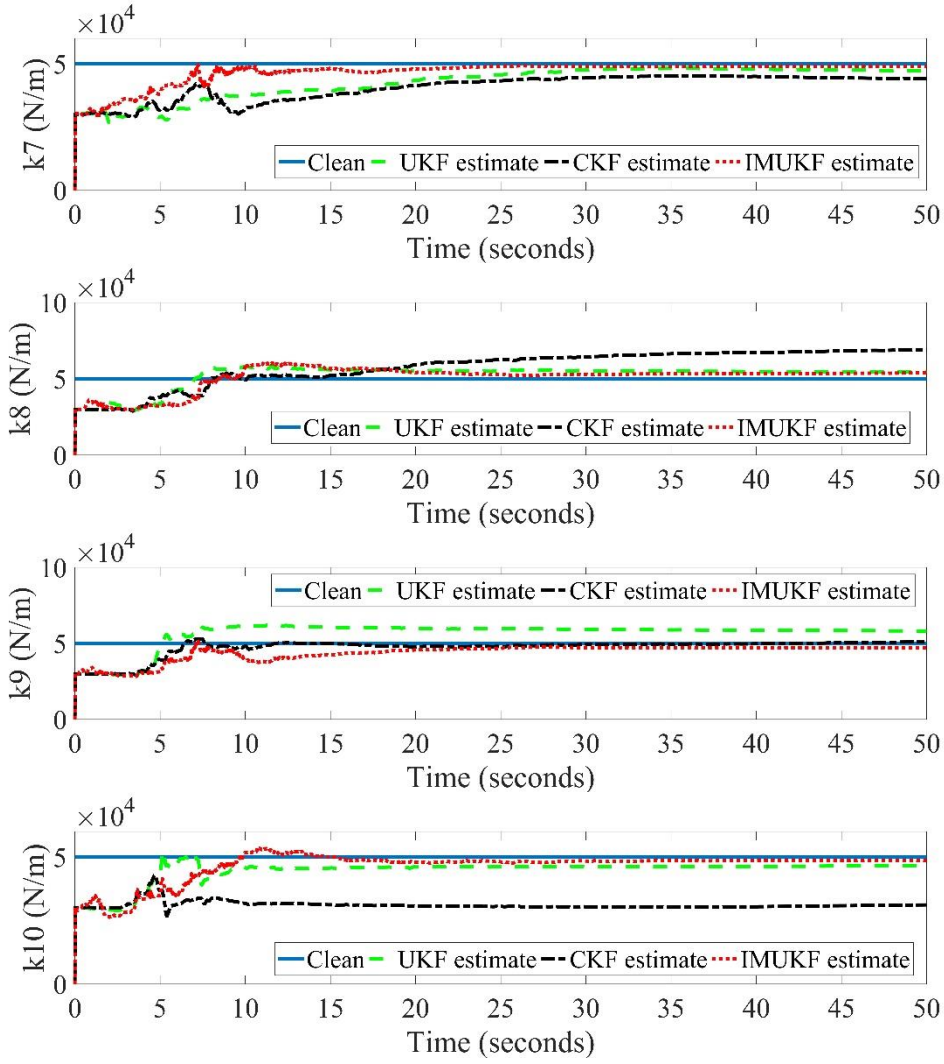

Figure 3-10: Predicted stiffness (k1–k10) values for a 10-DoF system with SNR = 15

As shown in Figure 3-10, for stiffness, the IMUKF is more accurate than the UKF and CKF techniques. Neither the UKF nor the CKF have a stable prediction trend in all DoFs, and in some cases, their predictions are quite far off, such as k3, k8, and k10, while IMUKF has the same trend in all DoFs.

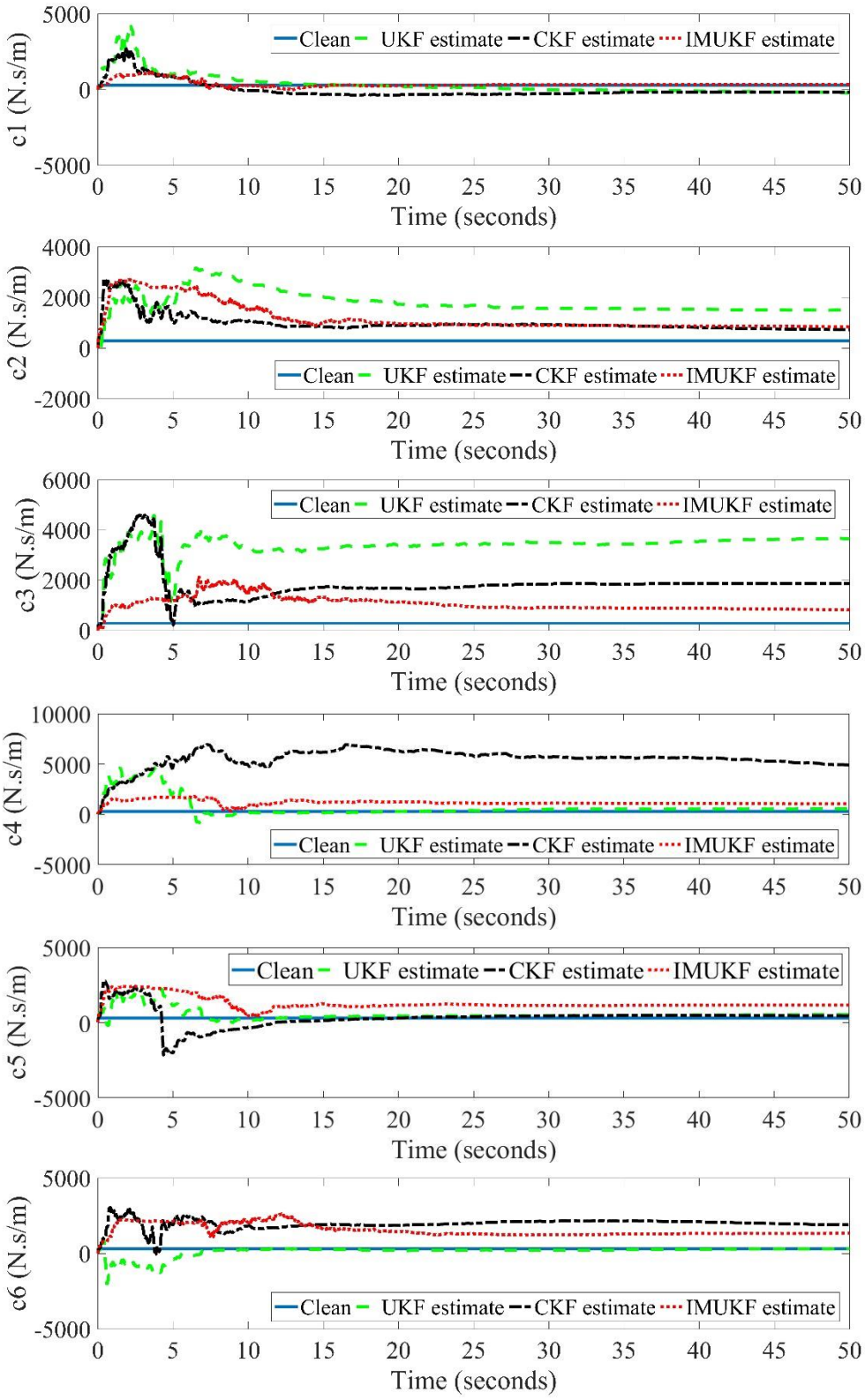

Figure 3-11: Predicted damping coefficient (c1–c10) values for a 10-DoF system with SNR = 15

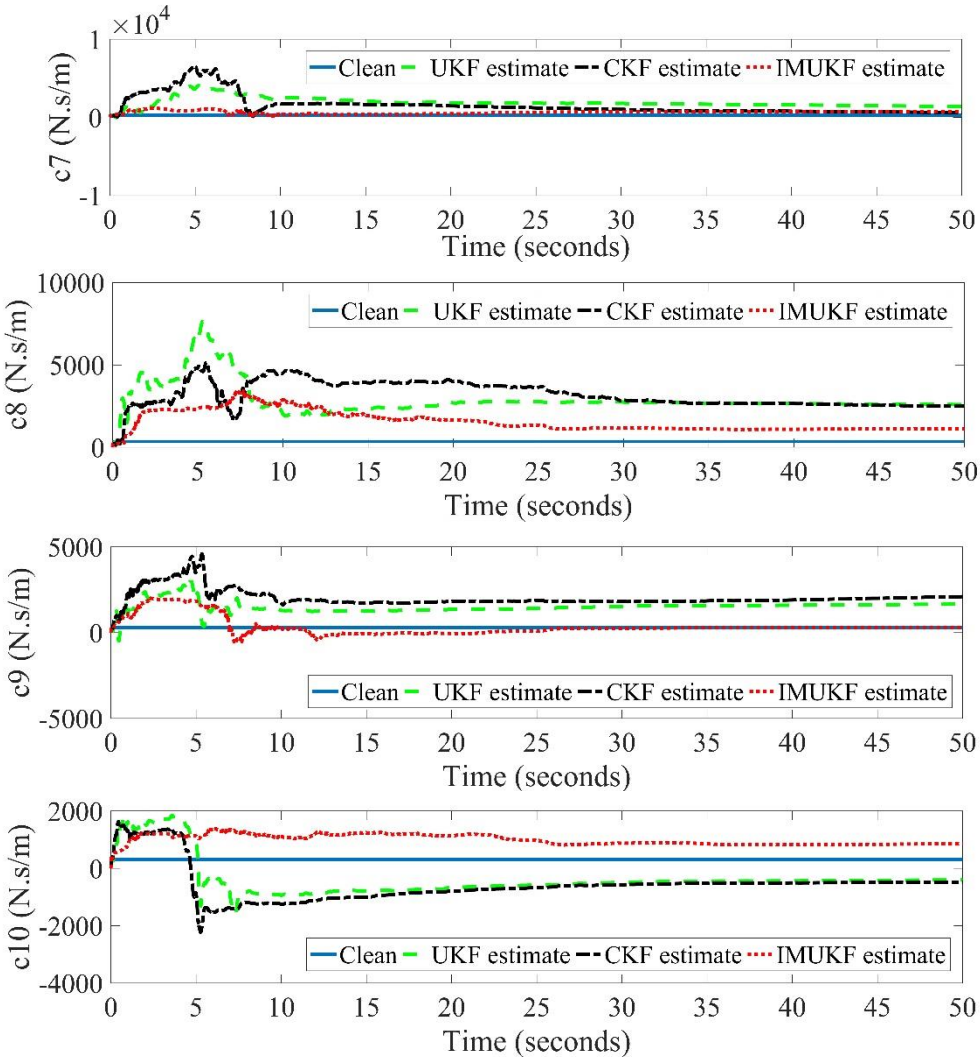

Figure 3-11: Predicted damping coefficient (c1–c10) values for a 10-DoF system with SNR = 15

Figure 3-10 and Figure 3-11 illustrate that the IMUKF method provides quite superior results to the UKF and CKF methods. Of course, as far as the computational cost is concerned, the UKF method is considerably faster, while the UKF and CKF methods seem to perform quite poorly.

A review of previous works in this field indicates that all the results for previous works are accurate in the case of a few DoFs, such as the previous 3-DoF system. In this paper, we propose a new method that is more powerful for high rates of noise in a large-DoF system. It must be mentioned that, for this system, only three measured acceleration responses from floors 1, 3, and 10 are used for prediction. Thus, seven other unknown states are added to the 40 states that have to be predicted. It is clear that the traditional UKF method diverges

specifically in the prediction of the damping coefficients, while the proposed method provides better results in the case of SNR 15, as shown in Figure 3-10 and Figure 3-11. Although there is some discrepancy for predicted damping using the proposed method, the method yields a constant value, while the UKF and CKF predicted values are unstable in each DoF and cannot be used.

3.4. **Conclusion**

A new system identification technique based on the unscented transform and cubature integration has been proposed in this paper. To improve the performance of UKF-based system identification, points calculated from the CKF are added to the UKF sigma points, as well as the iterative Kalman filtering concept, which is also adopted for the modified UKF. The main idea of the proposed method is the use of more sigma points than in the ordinary UKF, as well as the rearrangement of the nonlinear transformed data within the state transition function before substitution in the measurement function.

To demonstrate the performance of the proposed method, the method is applied to three different numerical examples. First, it is applied to the Bouc–Wen model with two different noise levels. The results showed that the proposed method (i.e., IMUKF) had better performance in predicting model parameters in high noise levels. Moreover, two linear 3-DoF and 10-DoF systems were investigated for comparative studies with high noise levels for large DoF systems. The results showed that in the 3-DoF systems, the results are similar to each other. However, in the 10-DoF system, the UKF showed weak performance, similar to methods described in previous journal articles, but the newly proposed IMUKF showed significantly better accuracy in predicting the stiffness values for the 10-DoF system with high noise levels. In the prediction of damping coefficient values, the proposed method still performed better than the traditional UKF.

Chapter Four:

Hybrid Output-only Structural System Identification Using Random Decrement and Kalman Filter

This chapter encloses the paper published in the peer-reviewed Journal *Mechanical Systems and Signal Processing*[1] introduced in the Co-authorship section. The paper introduces an output-only damage quantification method with the combination of two data-based and model-based methods. The method extracts the free vibration response of a dynamic system under any type of excitations or combination of them; then feeds the free vibration to the unscented Kalman filter to quantify the desired parameters of the underlying system. The capabilities of the proposed method are examined with numerous numerical models and one full-scale experiment. The method is capable of the quantification of the level of damage under different damage scenarios. A detailed explanation about the method and its implementation details are explained in this chapter, followed by the paper abstract.

---

1 **E. Ghorbani**, O. Buyukozturk, and Y. J. Cha, "*Hybrid output-only structural system identification using random decrement and Kalman filter*", Mechanical Systems and Signal Processing, 144 (2020): 106977.

Abstract, A novel hybrid output-only structural identification and damage identification method is proposed. The method is developed by integration of Kalman filtering as a model-based technique, and random decrement, as a data-driven technique. The random decrement method extracts free vibration from the structural system's measured responses under various types of loadings. The extracted free vibration is inputted into the Kalman filtering system to estimate the status of the structural system. In contrast to the traditional output-only techniques using the Kalman filter, it is not required to estimate the input excitation in the damage detection process. The Kalman filter uses only the free vibration responses extracted from the random decrement. This also leads to downsizing the size of the unknown state vector, which consequently decreases computational cost significantly. Since it is not required to use any parameter related to excitations in the mathematical model, the uncertainty of the physical model decreases. The proposed approach is numerically verified in three degrees of freedom and ten degrees of freedom systems under three different loading conditions. It is shown that the approach is robust to provide an accurate estimation of states under physical changes due to structural damage assuming the input data is unknown. As another verification, the stiffness and damping matrices of a seven-story building on a shake table are estimated to show the capability of the method for damage identification of real structures. These numerical and experimental case studies demonstrate that the proposed technique is capable of detecting, localizing, and quantifying the extent of damage in a structure under a combination of any kinds of loadings.

4.1. **Introduction**

Monitoring the condition of and identifying damage to civil, mechanical and aerospace engineering structures to evaluate the remaining life and performance of a system constitutes structural health monitoring (SHM). Damage identification usually consists of three different steps: damage detection, damage localization, and damage quantification. The damage identification techniques within vibration-based approaches are usually categorized into three approaches of data-driven techniques, model-based techniques, and hybrid techniques. Data-driven techniques entirely work based on the measured data and mostly reach the

second step of damage identification. Model-based techniques need a physics-based model in addition to the measured data. These approaches are capable of evaluating the extent of damage (damage quantification). For this reason, more research is focusing on the development of model-based techniques. However, these approaches have drawbacks because developing an accurate physics-based numerical model is difficult and tedious. Some studies have recently attempted to combine both model-based and data-driven approaches as hybrid techniques [60].

Vibration-based damage identification methods generally use both input excitation and the measured vibration response to estimate the physical status [61-63] of the underlying system. However, it is not almost viable to measure the input excitation forces in many civil infrastructures in normal operation [64]. Three different approaches have commonly been used to overcome the difficulties in measuring input excitation in a system. In the first approach, shakers are used to simulate the excitations on the structure, and the system response by this sophisticated excitation is used for damage identification. However, this is not a beneficial way to apply a shaker test on a massive infrastructure due to the tremendous mass on the shakers, in addition to the inaccuracy of the reproduced excitation rather than the real one. In some cases, although small-scale lab tests are applicable, but scaling issues and modelling complex boundary conditions are some of the main obstacles leading to the deviation between the result of the experimental test and the field results [9]. Therefore, the tendency for developing output-only techniques has grown up among researchers during the last decade.

The second approach is based on the estimation of the input using different filters, such as Kalman filtering. Kalman filtering as a model-based technique has been used for structural system identification and damage detection purposes. There are two different main approaches developed based on the Kalman filtering as an output-only system identification technique. The first group is joint input-state techniques, which count an input as a state that will be identified in the recursive process within other unknown states [65-67]. However, this approach increases the number of unknown states, which will decrease the estimation accuracy of the Kalman filters significantly [68]. Dual Kalman filtering is another solution that has been widely used for output-only system identification. At first, a Kalman filter is used to identify the input excitation, and the other Kalman filter is used for state estimation.

Obviously, the estimated states' accuracy is strongly dependent on the estimated input excitation by the first Kalman filter [53, 57]. Adding some auxiliary constraints to the system can be an alternative remedy to estimate the input excitation. As another example, Al-Hussain and Haldar [54, 55] set apart Rayleigh damping for the underlying system and used the least square technique to estimate the input followed by an unscented Kalman filter (UKF) to extract the system dynamic properties. Their Rayleigh damping assumption does not always fit for all the systems. Furthermore, they used the least square technique to extract the input, which is not an appropriate choice as a general approach working for any kind of loadings.

The third approach involves the reconstruction of the input using mathematical methods [69]. Autoregressive moving average (ARMA) methods, subspace methods, and Markov chain Monte Carlo (MCMC) methods are used to reconstruct the input in the damage identification process. In the subspace method [70], the input is usually assumed as a white noise signal for the frequency or time-domain techniques. Considering this, the result of the fast Fourier transform (FFT) of a white noise signal is a flat signal in the frequency domain; therefore, the transfer function is only dependent on the measured output's FFT. Because of this assumption, the input is replaced with a constant parameter in the nominator of the transfer function. For instance, Allen et al. [71] used this approach as an output-only modal analysis method for linear time-periodic systems. This is not a reliable assumption for situations where the input does not follow white noise behaviour.

As another example, Erazo and Nagarajaiah [72] considered a first-order Markov chain to parametrize the input excitation and used the Metropolis-Hasting sampling technique to estimate the input. This technique strongly depends on the selection of an appropriate sampling distribution and needs a high computational cost due to its iterative approach using many samples compared to the Kalman filter. All MCMC methods are time-consuming and are never comparable with KF methods. There are many references emphasizing that Kalman filters are significantly faster than MCMC [72, 73]. As model-based approaches, ARMA models have complicated mathematical equations, and many iterations are required for accurate response estimation. Their main weaknesses are related to their inaccuracy for the estimation of systems with combined excitations and systems with a high level of noise in

the measured data [74]. Moreover, for the ARMA model (as a time series statistical model), the selection of the order of ARMA coefficients is critical to avoid incorrect estimation [75].

To overcome the drawbacks of the current output-only approaches, in this study, a new hybrid method is proposed by a combination of random decrement (RD), as a data-driven approach, and Kalman filter, as a model-based approach. The RD extracts a free vibration response from the measured responses of the structure. This free vibration response is the input of the Kalman filter, and such a response is the only data used for identification by the Kalman filter, as the system uses a free vibration dynamic equation of motion for its state-space equation. The proposed method can perform damage quantification without estimation of input excitation. This is the main advantage of the proposed method compared to the traditional Kalman filter-based output-only approaches. As the input variables are omitted in the mathematical model of the system, the complexity and uncertainty of the state-space model of the Kalman filter are decreased [29, 76]. It also helps that the proposed method works for the damage identification of large state-space systems. Moreover, it will be shown that the proposed hybrid technique identifies the damage of structures under different kinds of loadings or combinations of them.

This paper is organized as follows. In Section 4.2, the overall proposed method is introduced with the mathematical basics of the RD technique and the formulation and algorithm of the UKF. In Section 4.4, three illustrative systems are selected to demonstrate the efficacy of the proposed method. The first system, a 3- degrees of freedom (DoF) numerical model, is used to show the accuracy of the proposed method's results and robustness considering three different loading conditions. For the second system, an iterated modified unscented Kalman filter (IMUKF) (which is introduced by the authors in their previous work [77] for identification of relatively large scale systems) is implemented as a renovation of the UKF in order to identify the stiffness and damping values of a 10-DoF numerical model. Finally, for experimental verification of the proposed approach, vibration responses of a seven-story shear building, mounted on a shake table, are analyzed by the proposed method when different levels of damage are localized in the building. Comparing the estimated values with respect to the existent works and their robustness to the change of physical parameters due to the different levels of damage demonstrates the proposed method's accurate performance while there is no input history available.

4.2. **Problem description**

For a linear *l*-DoF system with stationary random zero-mean excitation, the equation of dynamic motion can be represented in the following state-space form:

$$\mathbf{x}(t) = g(\mathbf{x}(t), \mathbf{f}(t), \mathbf{u}(t)), \tag{4.1}$$

$$\mathbf{Y}(t) = h(\mathbf{x}(t), \mathbf{f}(t), \mathbf{v}(t)), \tag{4.2}$$

where $\mathbf{x}$ is a state vector, completely assumed observable and controllable, and g and h are transition and measurement functions. $\mathbf{u}(t)$, and $\mathbf{v}(t)$ are the zero-mean white stationary process noise and measurement noise vectors, respectively. $\mathbf{f}(t)$ is the excitation vector which can have any form of white noise and stationary excitation, periodic excitation, ambient vibration, or any combination of these.

When both input and output data are measurable, Kalman filtering methods estimate a system stiffness and damping matrices effectively [73]. For situations that the input data are not available, some techniques are defined to estimate the input at first, followed by the traditional Kalman filtering techniques for estimation of stiffness and damping matrices, which these techniques are introduced in the introduction.

In reference to the literature review, current output-only approaches are faced with difficulties in finding the excitation information of an underlying system. This augmented computation process to identify input excitation information considerably reduces the accuracy of the results of system identification. In the present study, a new hybrid output-only method is proposed, and it does not require input excitation in the damage and system identification process. This idea contradicts that of traditional output-only approaches, which try to estimate or reconstruct the input excitation using the Kalman filter.

Conceptually, the total dynamics response of a linear system subjected to any kind of excitation contains free and forced responses. Considering this concept, in the output-only system identification problem addressed in this paper, instead of estimation or reconstruction

of the input data for the Kalman filtering process, the input excitation effect will be eliminated from the total measured response of the system.

The overall approach of the output-only system identification problem in the paper stands on the extraction of the free vibration responses from the measured total responses of a system using the RD method. Following that, the free vibration will be used in the Kalman filtering (KF) approach as output-only system identification. The schematic view of the proposed method is shown in Figure 4-1. The details of the RD method and nonlinear KF will be explained in the following section.

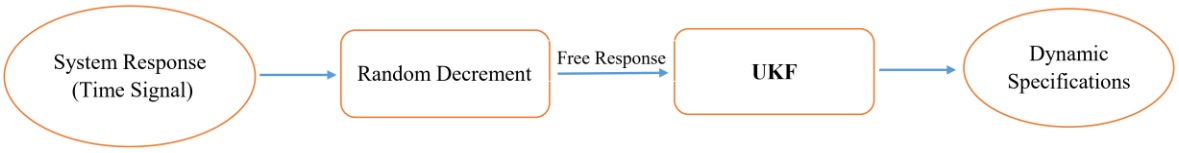

Figure 4-1: The proposed output-only method flowchart based on the nonlinear KF.

4.3. **Methodology**

In this section, at first, the basic of RD is introduced and following that the UKF algorithm is presented.

4.3.1. Random decrement method

The RD method was initially proposed by Cole [31] to extract the free vibration response from the measured response of a dynamic system subjected to random or ambient excitation. The RD method is data-driven and can only reach to the second step of the damage identification process. The technique has been adequately improved to determine the free vibration response of a system under different loading conditions [32]. In brief, it follows a simple process of averaging time segments of the measured system responses with a common initial or triggering condition. By using the procedure, the responses are transformed into the RD functions. At any time t, the total response can be decomposed into three parts, including:

i) the step response from the initial displacements;

ii) the impulse response from the initial velocity; and,

iii) the random response from the excitation applied to the structure in the period [9, 78].

Therefore, the dynamic response ($\mathbf{x}$) of j^{th} DoF of the system at a time t is written as:

$$\mathbf{x}_j(t) = \mathbf{x}_j(t)|_{x(0)} + \mathbf{x}_j(t)|_{\dot{x}(0)} + \mathbf{x}_j(t)|_{f(t)} \ , \ j = 0,1,2,\cdots l, \tag{4.3}$$

where, $a|_b$ means that a conditional b. Based on this understanding, we use the RD method to extract the free vibration responses from the system responses. In order to realize this, a trigger point ($x0$) is defined as shown in Figure 2.

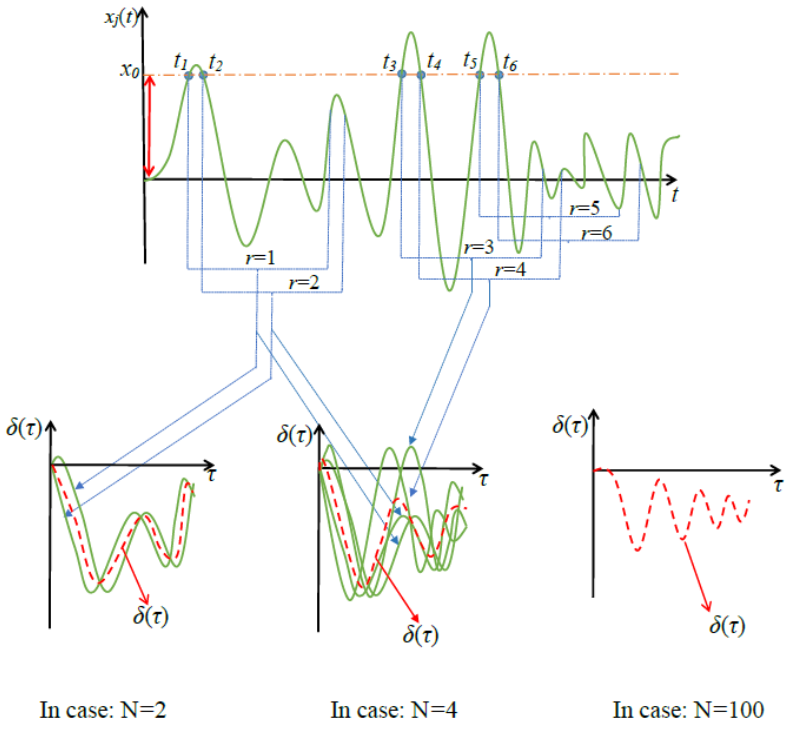

Figure 4-2: The Random decrement procedure

If $x_j(t)$ is reached to this $x0$, a predefined segment of the signal is captured with a constant length (τ). This constant length (τ) will be the length of the free vibration signals

as an output of the RD method. As shown in Figure 3-1, there are possibly more than one number of segments of the signal. All of these segments start from ($x0$) with the same length (τ) (i.e., the first segment $\mathbf{x}_j(t_1+\tau)$ starts at time t_1 to time $t_1+\tau$). These extracted multiple segments (i.e., r equal to 1: *N* in Figure 3-1) are eventually plotted in a new coordinate system by averaging as an output for each DoF.

The average of these segments, the free-response for each DoF, is calculated by:

$$\boldsymbol{\delta}_N(t)=\frac{1}{N}\sum_{r=1}^{N}\mathbf{x}_j(t_r+\tau)\ . \tag{4.4}$$

Users have to carefully choose the amplitude of the trigger point ($x0$) and constant length (τ) by trial and error. With an increasing number of segments (*N*), the contribution of the response due to the initial velocity (the second part of Eq.(4.3)) will average out due to its sign alternates. The third part of the Eq. (4.3) will average out due to the random zero-mean nature of the force response; therefore, the remnant is the response of the system due to the initial displacements, which have the free vibration form. Some mathematical equations of the RD technique are explained in Appendix B and the RD algorithm is summarized as follows:

i) Set the trigger point and the segment length that the selection depends on experiences;

ii) Gather the segmented responses with the same length when the trigger point is satisfied; and;

iii) Average the segments, and the result provides the free vibration response of the system.

The selection of the triggering level is an important aspect of the RD technique. Using a trigger point with low values might negatively affect the free vibration response by noise; however, a trigger point with a high value decreases the number of segments. To overcome this trade-off, a suitable level should be selected to ensure an adequate number of segments containing most of the crucial specifications of the underlying system. Brincker proposed

using $\sqrt{2}\sigma$ (σ is the standard deviation of the response time history) as a trigger point [79], and, usually, 20% of that is the trigger band [80]. For multi DoF systems, Ibrahim et al. suggested using the vector triggering random decrement technique [81]. In terms of the segment length, it is better to have a sufficient time length to see the complete decay of the response. Thus, the length of the segment should be large enough to cover some of the low frequencies of the structure because the length of the segments is inversely proportional to the frequency [79, 80].

As it was mentioned in the beginning, the input excitation has to be a zero-mean random signal. For other cases, such as periodic excitation and a combination of them, some modifications are necessary, which will be explained in the following section via numerical examples. The Natural Excitation Technique (NExT) [82] is another technique that also extracts the free vibration response. However, NExT needs the whole response while the RD just needs to save some of the segments of the signals. Moreover, RD uses simpler algorithms than NExT [83], so RD was used to extract the free vibration response.

4.3.2. Kalman filtering

As a model-based technique, Kalman filtering is strong enough to quantify the severity of the damage in a structure (it reaches the third step of damage identification). It requires input excitation, which is not proficient in many real situations. To overcome the aforementioned limitation, as a novel idea, the free vibration extracted by RD was used in the Kalman filtering for system and damage identification purposes. The state-space model for the free vibration motion of the Kalman filter does not require any input excitation. Regarding this, the state-space model of the system will be derived for identification of dynamic properties of the system using the KF as:

$$\dot{\mathbf{x}}(t) = g(\mathbf{x}(t), \mathbf{u}(t)), \tag{4.5}$$

$$\mathbf{Y}(t) = h(\mathbf{x}(t), \mathbf{v}(t)), \tag{4.6}$$

where $\mathbf{x}$ is a state vector, and g and h are transition and measurement functions. $\mathbf{u}(t)$, and $\mathbf{v}(t)$ are the process noise and measurement noise vectors, respectively. In order to estimate structural dynamic properties, such as stiffness and damping values, an unscented Kalman filter [27] is selected to be applied to the free vibration response of the system. Consider the discrete state-space model of Eq. (4.5) and Eq. (4.6):

$$\mathbf{x}_{k+1,k} = G(\mathbf{x}_k, \mathbf{u}_k), \tag{4.7}$$

$$\mathbf{Y}_k = H(\mathbf{x}_{k+1,k}, \mathbf{v}_k), \tag{4.8}$$

where $G(\mathbf{x}_k, \mathbf{u}_k) = \mathbf{x}_k + \int_{k\Delta t}^{(k+1)\Delta t} g(\mathbf{x}(t), \mathbf{u}(t))dt$, and $H = h$. Δt is a time-step, $\mathbf{x}_k$ is a state variable vector, $\mathbf{u}_k$ is a discrete process white noise, $\mathbf{Q}$ is defined as its covariance matrix, $\mathbf{Y}_k$ is the measurement vector, $\mathbf{v}_k$ is a discrete measurement process noise vector, and $\mathbf{R}$ is defined as its corresponding covariance matrix value. The UKF is as same as a linear Kalman filter consisting of two measurement and time-update steps, which calculates Kalman gain in the measurement step and updates the state vector and posterior estimation error for the next iteration in the update step [84].

Let us assume that states follow a Gaussian distribution with an initial assumption for the state's vector mean $\mathbf{m}$ and covariance error matrix $\mathbf{P}_0^{XX}$, sigma points (χ^i) can be defined as follows:

$$\chi^0 = \mathbf{m} ,$$

$$\chi^i = \mathbf{m} + \sqrt{\left((n+\lambda)\mathbf{P}_0^{XX}\right)}_i , \qquad i = 1, 2, ..., n \tag{4.9}$$

$$\chi^i = \mathbf{m} - \sqrt{\left((n+\lambda)\mathbf{P}_0^{XX}\right)}_{i-n} , \qquad i = n+1, n+2, ..., 2n$$

where n is the number of states, λ is a scaling parameter, and i index is a column vector number. Cholesky decomposition as a stable numerical method will be used for the square

root calculation of the covariance matrix. The corresponding weights for the sigma points are given by:

$$w_m^0 = \frac{\lambda}{n+\lambda},$$

$$w_c^0 = \frac{\lambda}{n+\lambda} + \left(1-\alpha^2+\beta\right), \tag{4.10}$$

$$w_m^i = w_c^i = \frac{1}{2\left(n+\lambda\right)}, \quad i = 1,\ldots,2n,$$

while $\lambda = \alpha^2(n+\kappa) - n$, α determines the spread of the sigma points and is a positive number $(0 \le \alpha \le 1)$; κ as a secondary scaling parameter equals to $3-n$, and $\beta = 2$ are optimal for Gaussian distributions.

The measurement step of the UKF consists of the calculation of a state vector, and output vector covariance matrices leading to the calculation of the Kalman gain is as follows:

$$\boldsymbol{\chi}_{k+1|k}^i = F\left(\boldsymbol{\chi}_k^i, \mathbf{u}_k\right), \tag{4.11}$$

$$\mathbf{P}_{k+1}^{XX} = \sum_{i=0}^{2n} w_c^i \left[\boldsymbol{\chi}_{k+1|k}^i - \sum_{i=0}^{2n} w_m^i \boldsymbol{\chi}_{k+1|k}^i\right]\left[\boldsymbol{\chi}_{k+1|k}^i - \sum_{i=0}^{2n} w_m^i \boldsymbol{\chi}_{k+1|k}^i\right]^T + \mathbf{Q}_k, \tag{4.12}$$

$$\begin{aligned}\mathbf{P}_{k+1}^{YY} = \sum_{i=0}^{2n} w_c^i &\left[\mathbf{H}\left(\boldsymbol{\chi}_{k+1|k}^i, \mathbf{v}_k\right) - \sum_{i=0}^{2n} w_m^i \mathbf{H}\left(\boldsymbol{\chi}_{k+1|k}^i, \mathbf{v}_k\right)\right] \\ &\left[\mathbf{H}\left(\boldsymbol{\chi}_{k+1|k}^i, \mathbf{v}_k\right) - \sum_{i=0}^{2n} w_m^i \mathbf{H}\left(\boldsymbol{\chi}_{k+1|k}^i, \mathbf{v}_k\right)\right]^T + \mathbf{R}_k,\end{aligned} \tag{4.13}$$

$$\mathbf{P}_{k+1}^{XY} = \sum_{i=0}^{2n} w_i^c \left[\boldsymbol{\chi}_{k+1|k}^i - \sum_{i=0}^{2n} w_m^i \boldsymbol{\chi}_{k+1|k}^i\right]\left[\mathbf{H}\left(\boldsymbol{\chi}_{k+1|k}^i, \mathbf{v}_k\right) - \sum_{i=0}^{2n} w_m^i \mathbf{H}\left(\boldsymbol{\chi}_{k+1|k}^i, \mathbf{v}_k\right)\right]^T. \tag{4.14}$$

$$\mathbf{G}_{k+1} = \mathbf{P}_{k+1}^{XY}\left(\mathbf{P}_{k+1}^{YY}\right)^{-1}. \tag{4.15}$$

The time update step of the UKF is:

$$\hat{\mathbf{x}}_{k+1} = \sum_{i=0}^{2n} w_m^i \, \boldsymbol{\chi}_{k+1|k}^i + \mathbf{G}_{k+1}\left(\boldsymbol{\delta}_{k+1} - \sum_{i=0}^{2n} w_m^i \, H\left(\boldsymbol{\chi}_{k+1|k}^i, \mathbf{v}_k\right)\right), \tag{4.16}$$

$$\mathbf{P}_{k+1} = \mathbf{P}_{k+1}^{XX} - \mathbf{K}_{k+1}\mathbf{P}_{k+1}^{YY}\mathbf{K}_{k+1}^{T}. \tag{4.17}$$

The time-step *k* is incremented. The $\hat{\mathbf{x}}_{k+1}$ in Eq. (4.16) is the estimated state's vector of the dynamic system.

An algorithm for the application of the RD-UKF approach for system identification is presented below in Figure 4-3 . This proposed technique will work for any linear system with any kind of excitation (e.g., random, periodic, and earthquake excitations).

In contrast to the joint input-state technique, where the number of states increases due to the append of the inputs to the state vector, in the proposed method, the number of states does not change, and this is a critical advantage of this technique. Likewise, in the dual Kalman filtering technique, at the first step, the input has to be estimated by the assumption of other states, which inaccurate in many cases and strongly depends on the initial guess of other states. Here, the effect of external excitation will be eliminated from the response, and the system parameters are identified only by using the free vibration response. In the next section, the performance of the proposed technique will be demonstrated using two numerical models under different loadings and one experimental case study to show the capability of the technique for real structures.

RD-UKF Algorithm

$\boldsymbol{\delta}_N(t)$ = **RD (** $\mathbf{x}(t)$, Δt **)**,

Initialize x_0, and τ,

set $N = 0$,

for $t_r = 0 : \Delta t : t$,

  if $\mathbf{x}_j(t_r) \geq \mathbf{x}_0$ for j[th] DoF,

    save $\mathbf{x}(t_r + \tau)$,

    $N = N + 1$,

  end if,

end for,

$$\boldsymbol{\delta}_N(\tau) = \frac{1}{N}\sum_{r=1}^{N}\mathbf{x}(t_r + \tau) .$$

$(\mathbf{x}, \mathbf{P})$ = **UKF (** $\boldsymbol{\delta}_N(\tau)$, $G(\cdot)$, $H(\cdot)$ **)**

initialize $\mathbf{x}_0$, and $\mathbf{P}_0$,

set Q, R, $\alpha, \beta,$ and κ.

for $i = 1 : \tau / \Delta t$

  calculate sigma points, χ, using Eq. (4.9), and their weights, w, using Eq. (4.10).

  propagate the sigma points using Eq. (4.11).

  update $\mathbf{P}_i^{xx}, \mathbf{P}_i^{xy}, \mathbf{P}_i^{yy}$ using Eqs. (4.12)–(4.14).

  estimate the new state vector $\mathbf{x}_i$ using Eq. (4.16) and the covariance matrix $\mathbf{P}_i$ using Eq. (4.17)

end for

Figure 4-3: The RD-UKF algorithm

4.4. **Implementation of the approach to numerical and real examples**

In order to examine the proposed output-only identification method, extensive numerical studies have been conducted. In Case 1, a 3-DoF system is analyzed with a white noise excitation. Case 2 used different stiffness and damping values of the 3-DoF with the same excitation to evaluate the robustness of the algorithm to the change of stiffness and damping values. In Case 3, a periodic excitation is applied on the same 3-DoF system to the Case1, and Case 4 used an earthquake excitation to that 3-DoF system. In the 5th case, the stiffness and damping values of a 10-DoF system were identified to show the applicability of the proposed technique for large DoF systems, and, in Case 6, as the application of the technique on a real structure, the vibration response of a seven-story shear building is analyzed to estimate its stiffness and damping matrices and following localized building damage on different floors under various damage levels. The details of each numerical example applied the RD scenarios, and the UKF and IMUKF implementation parameters are described in the following sections.

4.4.1. Case 1: A 3-DoF system with white noise excitation

As the first numerical implementation, the proposed method is applied to a 3-DoF system with white noise excitation. The governing equation of motion is:

$$[\mathbf{M}]\{\ddot{\mathbf{X}}(t)\}+[\mathbf{C}]\{\ddot{\mathbf{X}}(t)\}+[\mathbf{K}]\{\mathbf{X}(t)\}=\{\mathbf{f}(t)\}\ . \tag{4.18}$$

The system is simulated via MATLAB software with the mass value 500 kg, stiffness value 50000 N/m, and damping value 300 N.s/m for each DoF for 50 s while the input excitation is white noise with the power of 10^{-4}.

For identification purposes, the simulated system acceleration response (including noise) is processed using the RD technique to extract the free vibration response data. For the RD, the trigger point selected equals to $0.3\sqrt{\text{var}(\ddot{\mathbf{x}}_1)}$, and 30 s (i.e., τ in Eq.(4.4)) as the length of each segment while the response of the 1st DoF is selected for evaluation of the trigger point. The acceleration response of the system and the RD processed the free vibration

responses are shown in Figure 4-4. The white noise information is assumed as unknown in the identification process.

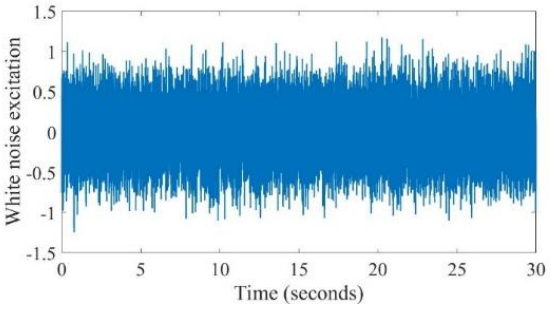

(a) $\ddot{\mathbf{x}}_1(t)$

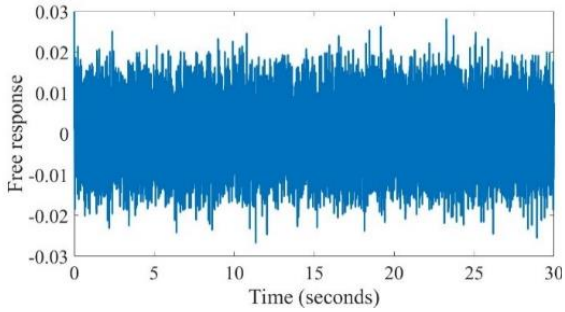

(b) $\ddot{\boldsymbol{\delta}}_1(t)$

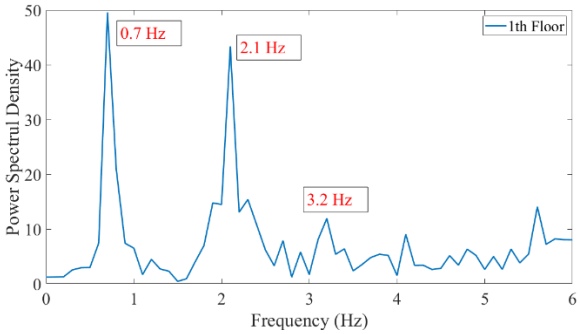

(c)

Figure 4-4: a) The acceleration response of the 1st DoF of the 3-DoF system, b) the RD processed response as the free vibration response of the 1st DoF of the system, c) Power spectral density (PSD) of free vibration response from the 1st DoF

The analytical natural frequencies of the system are 0.7 Hz, 1.98 Hz, and 2.86 Hz. Based on Figure 4-4-c, the natural frequencies of the free vibration response calculated using the RD technique are 0.7 Hz, 2.1 Hz, and 3.2 Hz using spectral analysis; these are close enough to the analytical responses. The free vibration responses $\ddot{\boldsymbol{\delta}}(t)$ obtained from the RD will be employed in the UKF as a model-based system identification technique. In this case, the system governing equation will change to:

$$[\mathbf{M}]\{\ddot{\boldsymbol{\delta}}(t)\}+[\mathbf{C}]\{\dot{\boldsymbol{\delta}}(t)\}+[\mathbf{K}]\{\boldsymbol{\delta}(t)\}=\mathbf{0}. \tag{4.19}$$

In the state-space model of the new governing equation without the input information, the state vector is defined as below:

$$\mathbf{x} = \begin{Bmatrix} x_1 & x_2 & x_3 & x_4 & \dot{x}_1 & \dot{x}_2 & \dot{x}_3 & \dot{x}_4 & k_1 & k_2 & k_3 & k_4 & c_1 & c_2 & c_3 & c_4 \end{Bmatrix}^T,$$

where the state space model is presented in Eq. (4.20) and Eq. (4.21). The prior information of the UKF for the structural identification are assumed as $m = 500$ kg, $k = 30000$ N/m, $c = 200$ N.s/m, and $x = \dot{x} = 0$ for each DoF.

$$\dot{\mathbf{x}} = \begin{Bmatrix} \dot{x}_1 \\ \dot{x}_2 \\ \dot{x}_3 \\ \ddot{x}_1 \\ \ddot{x}_2 \\ \ddot{x}_3 \\ \dot{k}_1 \\ \dot{k}_2 \\ \dot{k}_3 \\ \dot{c}_1 \\ \dot{c}_2 \\ \dot{c}_3 \end{Bmatrix} = \begin{bmatrix} x_4 \\ x_5 \\ x_6 \\ [-(x_7 + x_8)x_1 + x_8 x_2 - (x_{10} + x_{11})x_4 + x_{11}x_5]/m_1 \\ [x_8 x_1 - (x_8 + x_9)x_2 + x_9 x_3 + x_{11}x_4 - (x_{11} + x_{12})x_5 + x_{12}x_6]/m_2 \\ [x_9 x_2 + x_{12}x_5 - (x_{12}x_6 + x_9 x_3)]/m_3 \\ 0 \\ 0 \\ 0 \\ 0 \\ 0 \\ 0 \end{bmatrix} + \mathbf{u}(t)$$

$$= f(\mathbf{x}, t) + \mathbf{u}(t), \tag{4.20}$$

$$y = \begin{Bmatrix} \ddot{x}_1 \\ \ddot{x}_2 \\ \ddot{x}_3 \end{Bmatrix} = \begin{bmatrix} -(x_7 + x_8)x_1 + x_8 x_2 - (x_{10} + x_{11})x_4 + x_{11}x_5]/m_1 \\ [x_8 x_1 - (x_8 + x_9)x_2 + x_9 x_3 + x_{11}x_4 - (x_{11} + x_{12})x_5 + x_{12}x_6]/m_2 \\ [x_9 x_2 + x_{12}x_5 - (x_{12}x_6 + x_9 x_3)]/m_3 \end{bmatrix} + v(t)$$

$$= h(x, t) + v(t). \tag{4.21}$$

The simulation results based on the sampling rate of 1000 Hz are shown in Figure 4-5 and Figure 4-6.

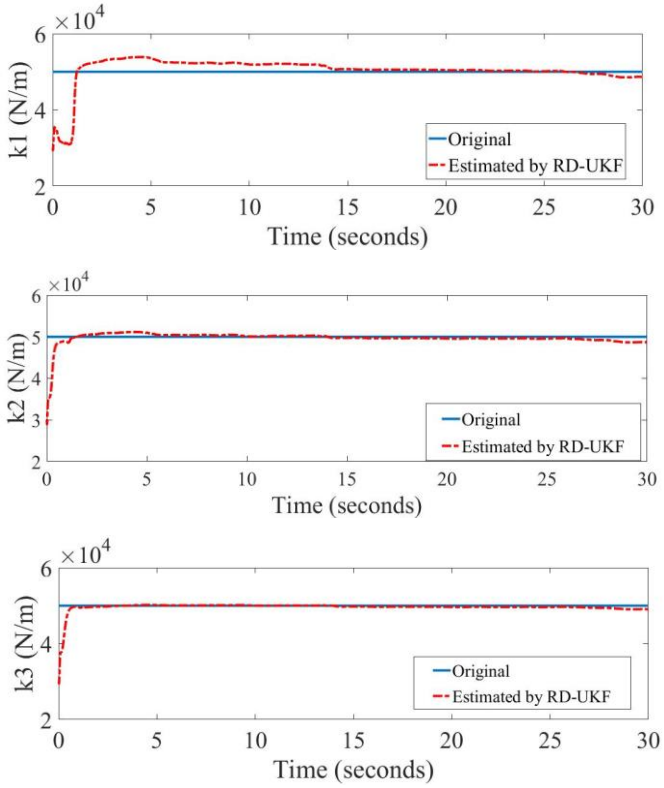

Figure 4-5: Case 1: Estimated stiffness (k1–k3) values with white noise excitation.

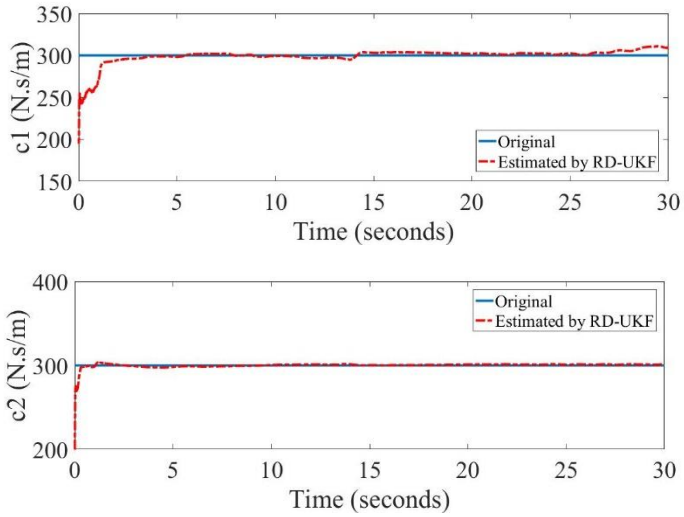

Figure 4-6: Case 1: Estimated damping (c1–c3) values with white noise excitation.

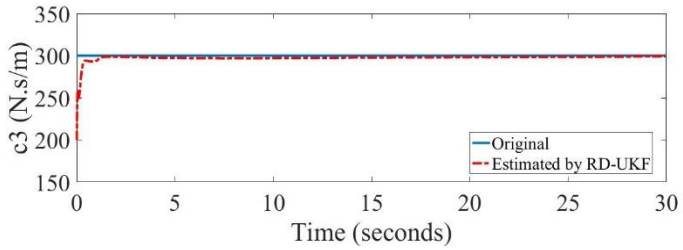

Figure 4-6: Case 1: Estimated damping (c1–c3) values with white noise excitation.

Obviously, an accurate model leads to an accurate result. In this study, no states or parameters related to the excitation input are involved in the state's vector in Eq. (4.20) and Eq. (4.21), which reduce the complexity and uncertainty of the physics-based mathematical model. In contrast, in the traditional model-based output-only approaches, the input parameter is induced to the state's vector [30], or it is estimated at first, and the estimated input is used in the identification process of states [53]. Both approaches increase the level of uncertainty in the state-space model. Considering this, in our proposed approach, the uncertainty level of the mathematical model decreases dramatically, which leads to a better performance of the Kalman filtering for large DoF systems, as well.

The proposed method has estimated the stiffness and damping values accurately based on Figure 4-5 and Figure 4-6. However, in Figure 4-4, the free vibration response does not appear as a usual free vibration response form. In addition, for the new RD-UKF technique, the trigger point and segment length, as two new constant values, are added to the other constant parameters of the UKF. In the following numerical example, Case 2, the stiffness and damping values of the system are changed to show the independence of the proposed method to these predefined constant values and the robustness of the technique, while all the predefined constant values of the RD-UKF are fixed based on the Case 1.

4.4.2. Case 2: Damage identification of the 3-DoF with white noise excitation

In Case 2, the new stiffness and damping values $k_1 = k_2 = k_3 = 55000\,\text{N/m}$, $c_1 = c_2 = c_3 = 270\,\text{N.s/m}$, (10 percent change from the original value) are used, but the same mass matrix is used in comparison with Case 1. With the same prior information for the UKF

and other constant parameters for the RD as Case 1, the new stiffness and damping values are estimated as shown below:

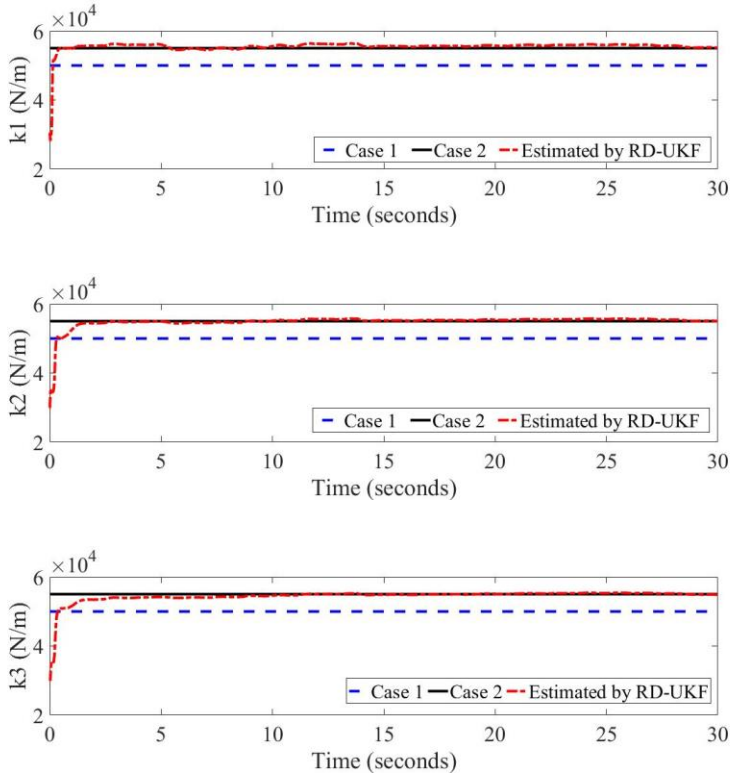

Figure 4-7: Case 2: Estimated stiffness (k1–k3) values with white noise excitation.

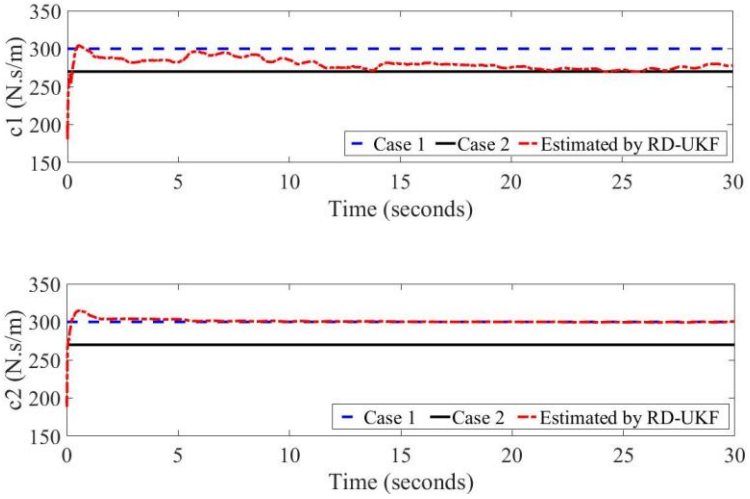

Figure 4-8: Case 2: Estimated damping (c1–c3) values with white noise excitation.

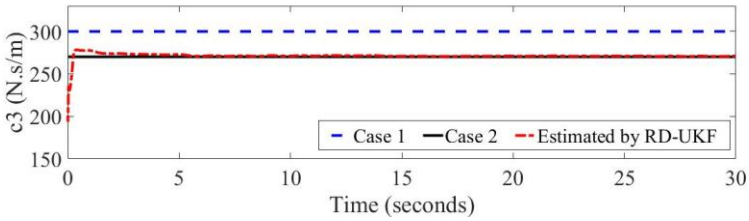

Figure 4-8: Case 2: Estimated damping (c1–c3) values with white noise excitation.

The robustness of the proposed method was validated from Figure 4-7 and Figure 4-8 with accurately estimated stiffness values using the same parameters as used in Case 1. As we simulated, the estimated stiffness values increased by 10 percent, and the estimated damping values decreased by 10 percent. The proposed method has estimated the new stiffness values accurately, and, for the damping values, it works well except for the second DoF of the system.

As a sensitivity analysis, this section addresses the capability of the technique to identify damage to the system under the same white noise loading condition but with different stiffness and damping values. The tuning parameters of the algorithm were the same as those used in Case 1. Thus, the proposed method is robust for tracking the changes in the stiffness values of the system, while the tuning parameters are fixed.

4.4.3. Case 3: A 3-DoF system with periodic excitation

The RD basically works well for excitations with random nature; then, to overcome the weakness of the RD for excitations with periodic components, some modifications are proposed [85, 86]. For a linear system, based on the superposition rule, the main idea comes from the elimination of that part of the total response caused by the periodic excitation.

In linear systems, a periodic excitation leads to a periodic response, which is repeated based on the excitation frequency. If there is more than one periodic excitation component, the component with the lowest frequency is defined as the main frequency of all periodic excitations. Dividing the measured response to α segments with equal length and averaging, the resultant averaged signal can be used to subtract the effect of periodic components from the total response. The remaining signal, after subtracting the periodic parts, is the sum of

the random excitations and the initial value responses that can be processed by the RD technique.

From a mathematical point of view, the signal will be divided into portions $\alpha = bTF_s$ where *b* is an arbitrary integer, *T* is the main period, which is equal to the inverse of the main frequency, and F_s is the sampling rate of the measured response. The average, $\mathbf{x}_p$, of the segments is given by:

$$\mathbf{x}_p(j) = \frac{1}{[(\Gamma - j)/\alpha]} \sum_{i=1}^{[(\Gamma-j)/\alpha]} \mathbf{x}(j + i\alpha), \quad j = 1, 2, \cdots \alpha, \tag{4.22}$$

where *j* is a time-step of the mean average, $\mathbf{x}$ is the response with size Γ and $\mathbf{x}_p$ is the mean average of the segments, and [ ] is the floor function operator. In the next step, the $\mathbf{x}_p$ will be subtracted from the total response and the remnants are the responses due to the random excitations and initial values ($\mathbf{x}_R$).

$$\mathbf{x}_R = \mathbf{x} - \mathbf{x}_p, \tag{4.23}$$

$$. \mathbf{x}_R(\alpha i : \alpha(i+1) - 1) = \mathbf{x}(\alpha i : \alpha(i+1) - 1) - \mathbf{x}_p \qquad i = 0, 1, 2, \cdots [(\Gamma - \alpha)/\alpha]. . \tag{4.24}$$

Now, the $\mathbf{x}_R$ can be processed by the RD technique to eliminate the component of the response related to the random excitation. Based on the defined 3-DoF system (Case 1) in the previous section, the input excitation is changed to a combination of random white noise (F_R) with the power 10^{-4} and two sinusoid signals with different amplitude and frequencies ($F(t) = F_R(t) + 7\sin(3\pi t) + 6\sin(2\pi t)$). The excitation and, following that, the response of the system due to the combined excitation are shown in Figure 4-9.

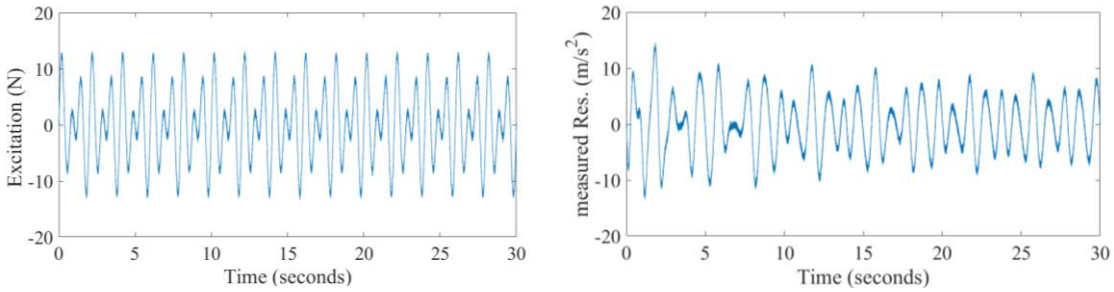

(a) (b)

Figure 4-9: a) The periodic excitation, and b) the system total response.

Based on the linear system theory, the system response contains three different parts: 1) the response of the periodic excitations; 2) the response of the random excitation; and 3) the response of the system due to initial conditions of the system.

To implement the output-only UKF, the first two parts should be eliminated. At first, using Eqs. (4.22)-(4.24), the periodic parts are removed. In this study, as the input force is known for simulation, the main frequency is set to 2π Hz, and the sampling rate is equal to 1000 Hz. For constant value, b equals π, and the signal will be divided into 500 parts. After averaging and subtracting the periodic part from the total response, the remnant is the system response due to random excitation and initial values. The effect of the random excitation will be omitted by the RD. To implement the RD, the trigger point is selected $1.2\sqrt{\text{var}(\ddot{x})}$ of the first DoF and only 30 s of the response is considered for averaging. The remnant will be the system response to the initial condition (named as free vibration response), which is used for the output-only UKF system identification, as shown in Figure 4-10.

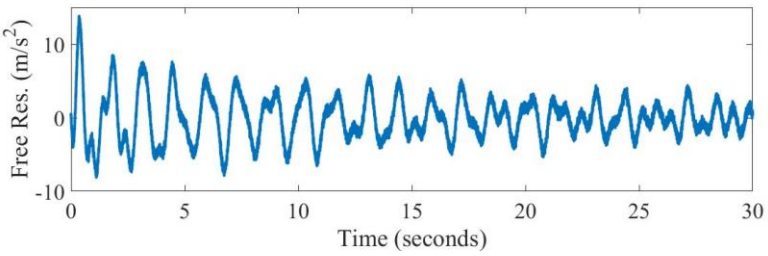

Figure 4-10: The free vibration response of the system after removing external forces using the RD method.

To implement the UKF, per the previous section, the state-space model (Case 1) of the previous section is used for identification with the same initial condition. The estimated stiffness and damping values are shown in Figure 4-11 and Figure 4-12. In this case, as like as case 1 and case 2, only the simulated system acceleration response is used for the identification process.

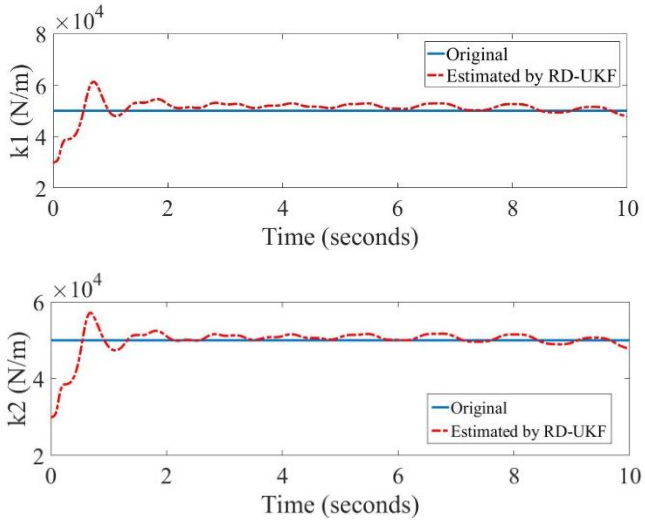

Figure 4-11: Case 3: Estimated stiffness (k1–k3) values with periodic excitation.

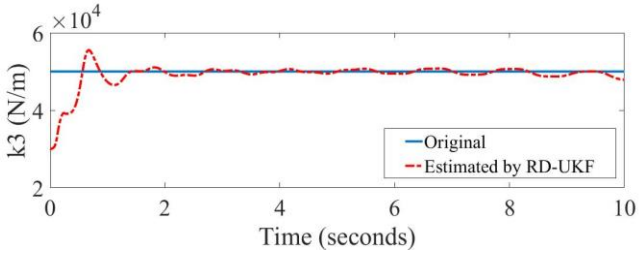

Figure 4-11: Case 3: Estimated stiffness (k1–k3) values with periodic excitation.

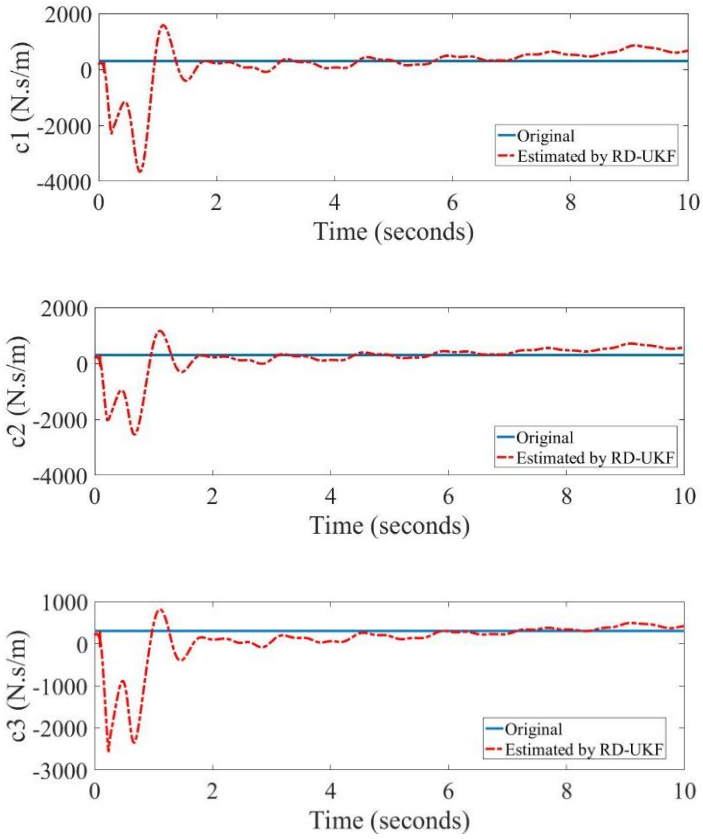

Figure 4-12: Case 3: Estimated damping (c1–c3) values with periodic excitation.

Based on Figure 4-11 and Figure 4-12, the iteration converges to the clean response after 10 s (10,000 time-steps). The duration for the proposed RD-UKF technique for output-only identification is approximately 58 s on an Intel® core™ i5 2400 K CPU @ 3.10 GHz. To calculate the main period (T) in field tests (since there is no information about the input), pre-signal processing of the measured response and using fast Fourier transform (FFT) can be helpful to find the lowest periodic frequency component (T).

4.4.4. Case 4: A 3-DoF system with earthquake excitation

Heretofore, the proposed output-only UKF technique is applied on a 3-DoF system with random and periodic excitation. Also, it is shown how the periodic part of a linear system response can be removed from the system response. In this section, the proposed technique is applied to extract the stiffness and damping values of the pre-defined linear 3-DoF system while it is excited with the EI-Centro earthquake data, shown in Figure 4-13 during 50 s. This record is only used for the simulation of the system, and it is assumed as unknown in the identification process. Therefore, only the acceleration response of the system is used.

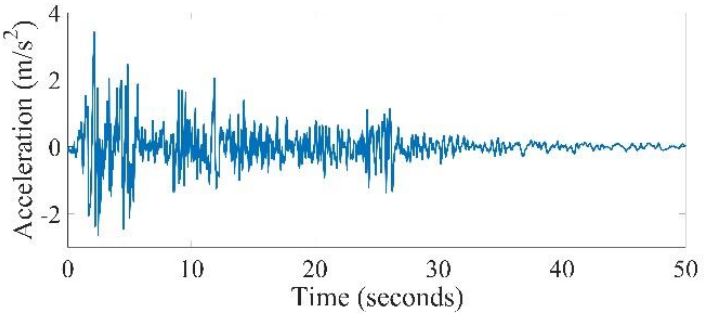

Figure 4-13: EI-Centro earthquake acceleration time history.

The system acceleration response by the earthquake excitation is averaged using the RD technique to extract its free vibration response as shown in Figure 4-14. The trigger point of the RD is selected $0.5\sqrt{\text{var}(\ddot{\mathbf{x}}_1)}$ of the first DoF, and only 30 s of the response is considered for averaging. Similar to the previous sections, the sampling rate is equal to 1000 Hz. The estimated values are converged to the true one after 15 s as shown in Figure 4-15 and Figure 4-16.

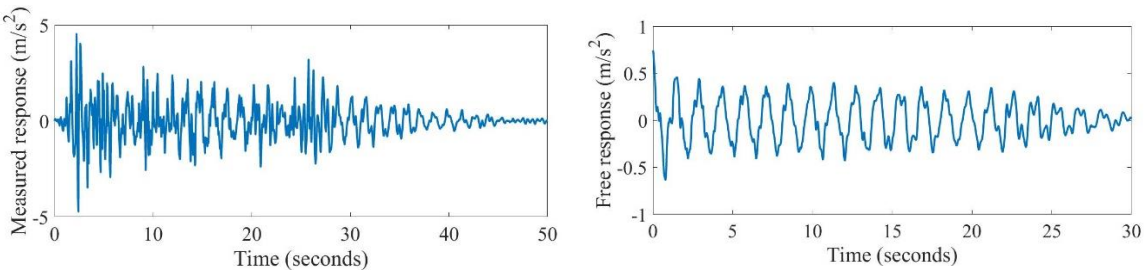

(a) $\ddot{\mathbf{x}}_1(t)$ (b) $\ddot{\boldsymbol{\delta}}_1(t)$

Figure 4-14: a) system response due to El-Centro earthquake excitation, and b) the system free vibration response using the RD method.

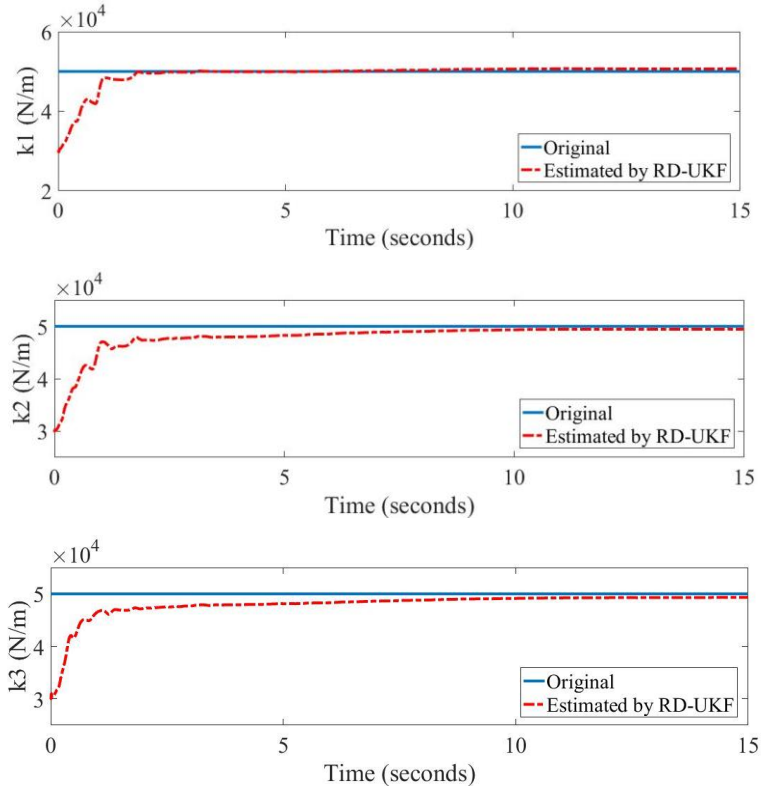

Figure 4-15: Case 4: Estimated stiffness (k1–k3) values with earthquake excitation.

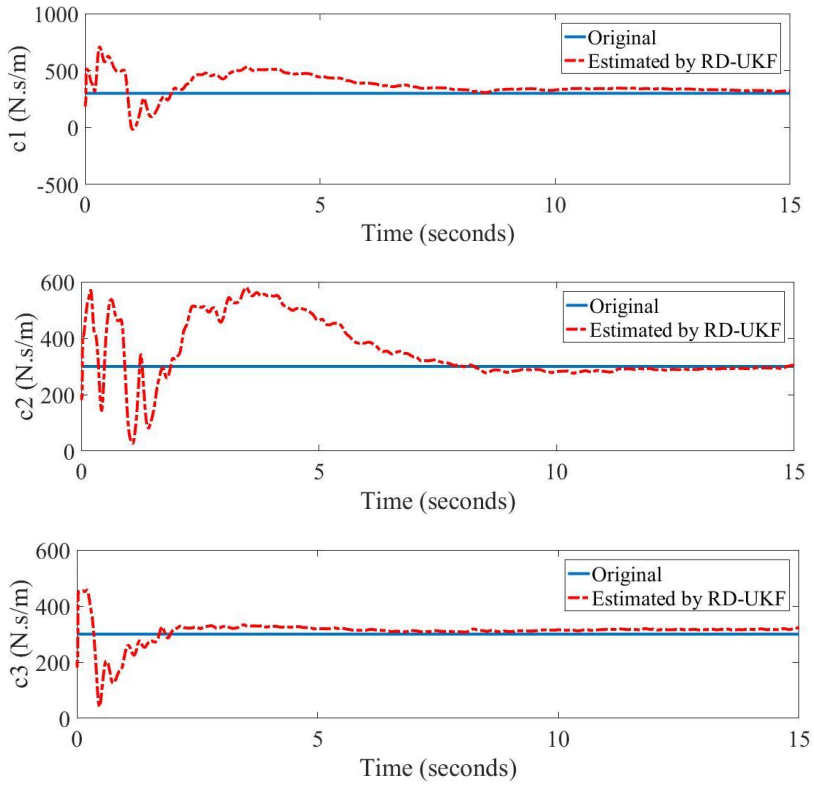

Figure 4-16: Case 4: Estimated damping (c1–c3) values with earthquake excitation.

For the UKF implementation, the same as previous sections, the prior information of the UKF for the structural identification are $m = 500$ kg, $k = 30000$ N/m, $c = 200$ N.s/m, and $x = \dot{x} = 0$, for each DoF. As earthquakes are random in nature, the basic RD can be used to extract the free vibration response. It should be mentioned that the selection of the trigger point and length of the segments strongly depend on the data and experience. The duration for the proposed RD-UKF technique for output-only identification is approximately 60 s on an Intel® core™ i5 2400 K CPU @ 3.10 GHz.

4.4.5. Case 5: A 10-DoF system with earthquake excitation

In this section, the proposed algorithm is applied to a 10-DoF system. With four unknown states (i.e. x, $\dot{x}$, k, and c) for each DoF, a total of 40 unknown states have to be estimated for this system. The UKF has limitations in the identification of large state-space systems [68, 87]; therefore, in our previous study, an iterated cubature unscented Kalman filter (IMUKF) was introduced to overcome this limitation [77]. To develop an output-only system

identification method viable for large state-space systems, the UKF used in Cases 1-4 is replaced with the IMUKF, meaning that the RD technique is jointed with the IMUKF method as an output-only system identification technique for large state-space systems. The flowchart in Figure 4-1 is modified and showed again in Figure 4-17. Notably, the main difference between UKF and IMUKF relies on the number of the sigma points and the two scaling parameters in the IMUKF. The details of the IMUKF are found in Ghorbani and Cha [77].

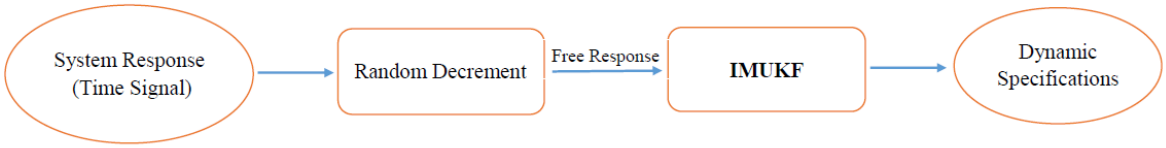

Figure 4-17: The proposed output-only method flowchart based on the IMUKF.

Based on the flowchart in Figure 4-17, at first, the system is simulated with the El-Centro earthquake excitation (see Figure 4-13) across 50 s. The constant values for simulation are $m_1 = m_2 \cdots\cdots m_{10} = 500$ kg, $k_1 = k_2 \cdots\cdots k_{10} = 50000$ N/m, and $c_1 = c_2 \cdots\cdots c_{10} = 300$ N.s/m, with the sampling rate of 500 Hz. As in previous cases, the EI-Centro earthquake excitation is only used for simulation purposes, and it is unknown in the identification process. The simulated system acceleration response is only recorded for identification purposes.

Based on our experience, putting the sensors on the lower floors results in a more accurate estimation of the stiffness and damping of all the floors. In the identification process using the RD-IMUKF the segment length is 30 s, and the trigger point of RD is selected as $0.5\sqrt{\text{var}(\ddot{\mathbf{x}})}$ once on the first DoF and another time on the fifth DoF of the system to show the effect of the trigger point on the estimation of parameters. The prior information of the state's vector in the IMUKF identification process is assumed as $\left[\tilde{\mathbf{x}} \quad \dot{\tilde{\mathbf{x}}} \quad \mathbf{K} \quad \mathbf{C}\right]$. Its each component is set to: $\tilde{\mathbf{x}} = \text{zeros}(10,1)$, $\dot{\tilde{\mathbf{x}}} = \text{zeros}(10,1)$, $\mathbf{K} = 30000 \times \text{ones}(10,1)$, and $\mathbf{C} = 200 \times \text{ones}(10,1)$. Furthermore, the initial error covariance matrix is defined as $\text{diag}[\mathbf{P}_x \quad \mathbf{P}_{\dot{x}} \quad \mathbf{P}_k \quad \mathbf{P}_c]$ where $\mathbf{P}_x = \mathbf{P}_{\dot{x}} = \text{ones}(10,1)$, $\mathbf{P}_k = 10^7 \times \text{ones}(10,1)$, and

$\mathbf{P}_c = 10^6 \times \text{ones}(10,1)$. The IMUKF tuning parameters are $\gamma_1 = 3$ and $\gamma_2 = 5$ as scaling parameters, and $\eta = 0.04$ is the reduce rate of the iterated Kalman filter with 10 iterations. The process and measurement noise covariance matrices are $10^{-12}\,\mathbf{I}_{40}$, and $10^{-4}\,\mathbf{I}_{10}$, sequentially. The duration for the RD-IMUKF identification is approximately 540 s on an Intel® core™ i5 2400 K CPU @ 3.10 GHz.

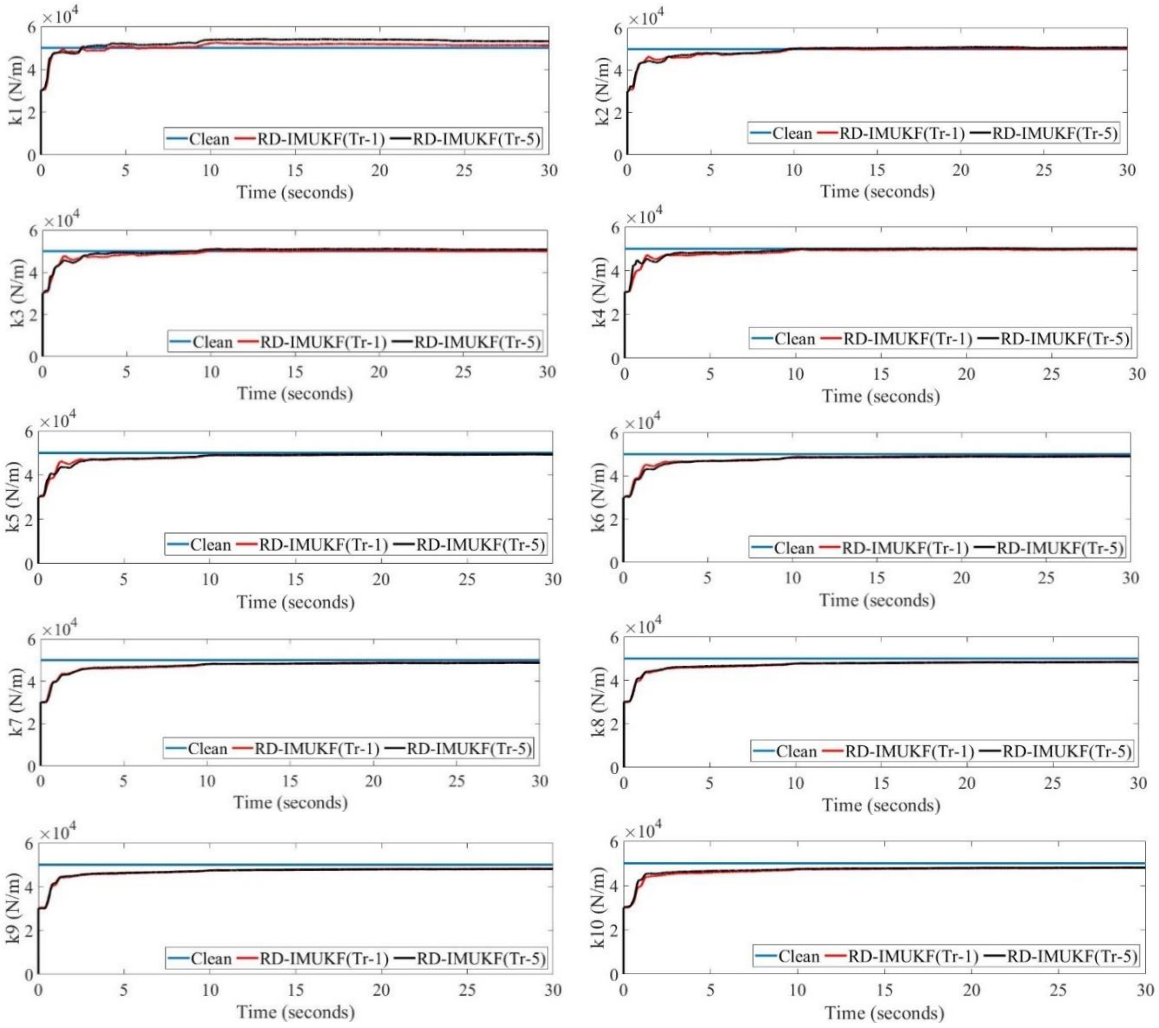

Figure 4-18: Case 5: Estimated stiffness (k1–k10) values for the 10-DoF system.

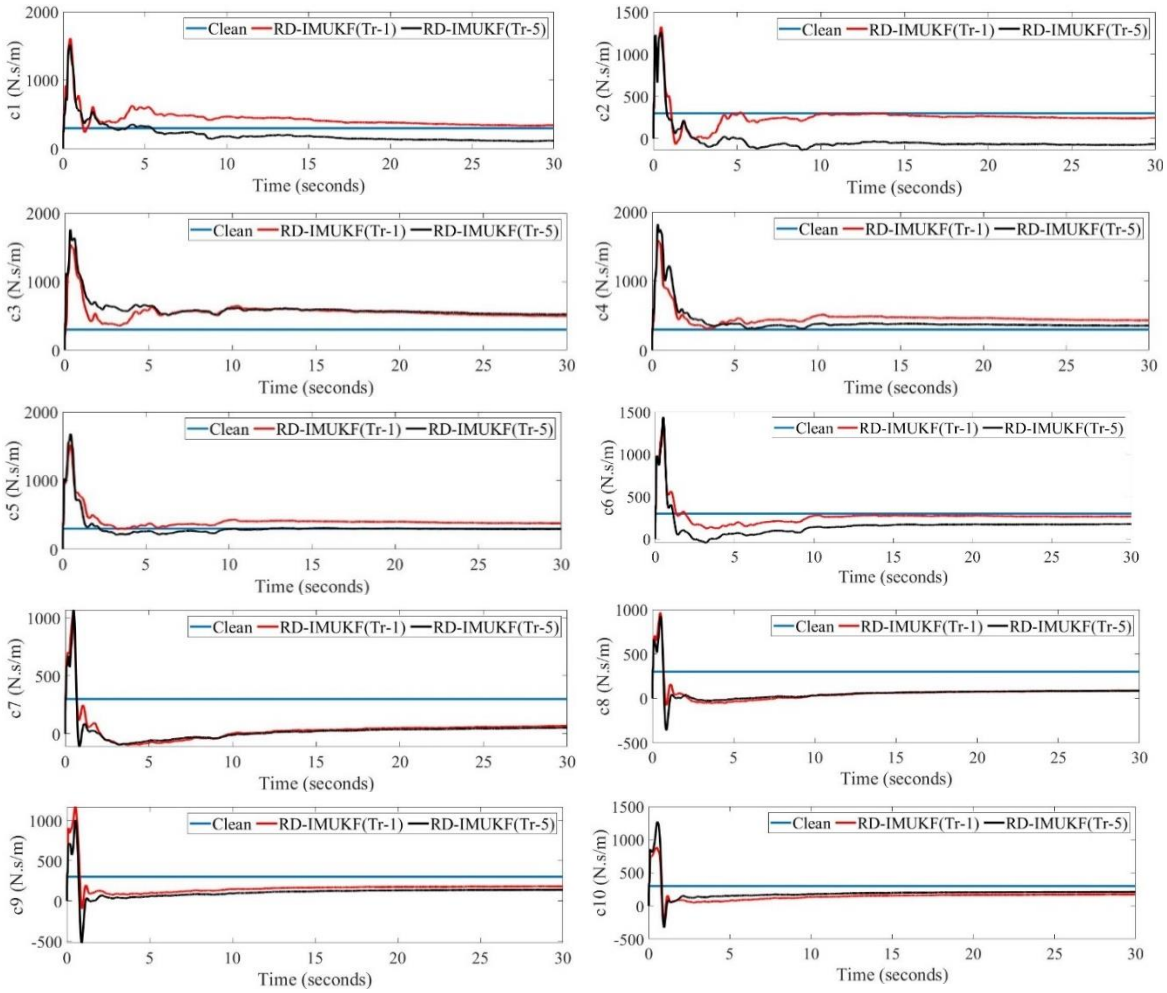

Figure 4-19: Case 5: Estimated damping (c1–c10) values for the 10-DoF system.

The estimated values of the stiffness and damping are shown in Figure 4-18 and Figure 4-19 respectively, for two different trigger points. Based on these figures, the stiffness estimation converges to the clean response after approximately 10 s for both trigger points. Comparison with previous work [77] shows that the stiffness values were accurately estimated, while the damping values presented some deviations for both trigger points in certain DoFs (c7–c10) because of the large difference between the stiffness and damping values. However, this result is inevitable [88].

4.4.6. Case 6: A seven-story residential load bearing wall building

The test structure, as shown in Figure 4-20 represent a slice of a seven-story residential load-bearing wall building located at the University of California at San Diego (UCSD). It consists

of a main wall (web wall) providing lateral force resistance in the East-West direction, a back wall perpendicular to the main wall (flange wall) for transversal stability, a concrete slab at each floor level (except at the base), an auxiliary post-tensioned column to provide torsional stability, and four gravity columns to transfer the weight of the slabs to the shake table plate [89]. More details about the building are available in [90].

The building was instrumented with a dense array of over 430 data channels consisting of different kinds of sensors. In this study, data from 14 longitudinal acceleration channels (on the web wall at each floor level and at mid-height of each story) were used to estimate the stiffness and damping matrices at different damage states of the building. The measured acceleration responses sampling rate is 240 Hz (Nyquist frequency of 120 Hz). These measured data were band-pass filtered between 0.5 Hz and 25 Hz using a high order (1024) FIR filter [89].

The building was excited with four different earthquake records simulated by the shake table. The four historical earthquake records applied to the building are as follows: (1) longitudinal component of the 1971 San Fernando earthquake (magnitude = 6.6) recorded at the Van Nuys station (EQ1); (2) transversal component of the 1971 San Fernando earthquake recorded at the Van Nuys station (EQ2); (3) longitudinal component of the 1994 Northridge earthquake (magnitude. = 6.7) recorded at the Oxnard Boulevard station in Woodland Hill (EQ3); and, (4) 360_ component of the 1994 Northridge earthquake recorded at the Sylmar station (EQ4). Excitations based on white noise consist of eight-minute-long realizations of a banded white noise (0.25–25 Hz) process with root-mean-square (RMS) amplitudes of 0.03 g. Table 4-1 reports the dynamic tests used in the present study of the building at various damage states. Obviously, it is assumed that these records are not available in the identification process. The data coming from test numbers 39, 41, 46, 49, 61, and 64 are only used in the identification process without any information about the applied earthquakes.

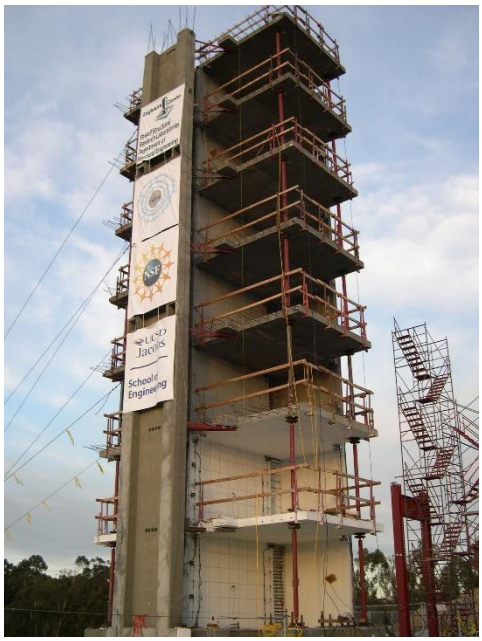

Figure 4-20: The building test structure [89].

Table 4-1**:** List of the dynamic tests to induce damage and ones used in the identification process.

Test No.	Test discerption	State
39	8 min WN (0.03 g) + 3 min AV	D0
40	EQ1	
41	8 min WN (0.03 g) + 3 min AV	D1
43	EQ2	
46	8 min WN (0.03 g) + 3 min AV	D2
48	EQ3	
49	8 min WN (0.03 g) + 3 min AV	D3-1
61	8 min WN (0.03 g) + 3 min AV	D3-2
62	EQ4	
64	8 min WN (0.03 g) + 3 min AV	D4

WN: white noise base excitation test,

AV: ambient vibration test.

For the identification purpose, the building geometrical information and its construction material specifications, such as the elasticity modulus (Young's modulus), are

used to estimate prior information. Regarding that, as the building slice is on the shake table, each floor's initial stiffness can be calculated by the equation $\frac{12EI}{L^3}$. *E* is Young's modules, *I* is the second-moment inertia of the web wall, and *L* is the web wall height in each floor. The initial critical damping ratio (ξ) is assumed equal to 0.02.

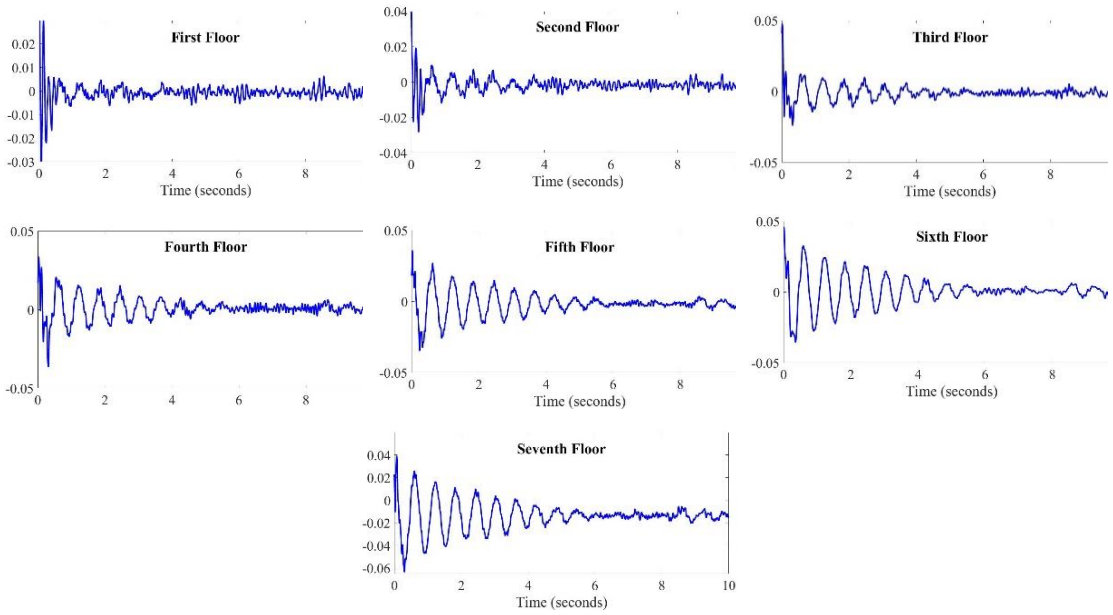

Figure 4-21: The free vibration response of the building each story without any damage (D0).

The free vibration response vibration is extracted from the measured response, numbers 39, 41, 46, 49, and 61 (see Table 4-1), of each floor for all damage states (D0-D4) using the RD technique. The trigger point is selected equal to $1.4\sqrt{\text{var}(\ddot{\mathbf{x}}_6)}$ of the sixth floor, and each segment length is set to the total signal length divided by 30. The free vibration response of the building for each story are shown in Figure 4-21, using data number 39 for damage state D0. The free vibration responses of the building under different damage states are shown in Appendix C. It should be mentioned that only the system response is involved in the extraction of free responses.

The extracted free vibration responses are used for the identification of the stiffness and damping matrices of the building, only considering the knowledge of the mass matrix without any information about the input excitation. For the identification process, the UKF is employed. The mathematical equation of a linear 7-DoF damped mass-spring model is

derived in the state-space form, and the parameters are extracted by the unscented Kalman filter. The state vector ($\mathbf{x}$) with the dimension of 28 is in the form of:

$$\mathbf{x}=\{x_1 \quad \cdots \quad x_7 \quad \dot{x}_1 \quad \cdots \quad \dot{x}_7 \quad k_1 \quad \cdots \quad k_7 \quad c_1 \quad \cdots \quad c_7\}^T,$$

and the dynamic equation of motion is:

$$[\mathbf{M}]\{\ddot{\boldsymbol{\delta}}(t)\}+[\mathbf{C}]\{\dot{\boldsymbol{\delta}}(t)\}+[\mathbf{K}]\{\boldsymbol{\delta}(t)\}=\mathbf{0}. \tag{4.25}$$

Based on Table 4-1, the excitation force lasted for a total of 11 min; the excitation for the first 8 min was white noise vibration and that for the remaining 3 min was ambient vibration. Regarding excitation, existing studies [89, 91] have reported that all the damage scenarios (D0–D4) have different natural frequencies, thus presenting different levels of damage for these scenarios due to successive tests as well as their accumulated damage.

In order to assess how our proposed method estimates the changed natural frequencies from the excitation tests, we applied our method using the excitations presented in Table 4-1. The sampling rate of measured responses from each floor is 240 Hz. The UKF is tuned with the constant parameters, process noise matrix, measurement noise matrix, and initial values. The process and measurement noise matrices are tuned $10^{-4.3}\mathbf{I}_{28\times28}$, and $10^{-9}\mathbf{I}_{7\times7}$, respectively, where $\mathbf{I}$ is the unit matrix. The initial state's vector $\left[\tilde{\mathbf{X}} \quad \dot{\tilde{\mathbf{X}}} \quad \tilde{\mathbf{K}} \quad \tilde{\mathbf{C}}\right]$, is set to $\tilde{\mathbf{X}}=\dot{\tilde{\mathbf{X}}}=\text{zeros}(7,1)$, each story equivalent mass (m_i), initial stiffness ($\tilde{\mathbf{K}}$), and other geometrical information are presented in Table 4-2. The initial damping can be calculated by $\tilde{\mathbf{C}}=2\zeta\sqrt{\tilde{\mathbf{K}}(i)\times m_i}\times\text{ones}(7,1)$ where $i=1\cdots7$. The initial error covariance matrix of the UKF, $\mathbf{P}_0^{xx}=\text{diag}[\mathbf{P}_x \quad \mathbf{P}_{\dot{x}} \quad \mathbf{P}_k \quad \mathbf{P}_c]$, is equal to $\mathbf{P}_x=\mathbf{P}_{\dot{x}}=\text{ones}(7,1)$, $\mathbf{P}_k=10^{13.5}\times\text{ones}(7,1)$, and $\mathbf{P}_c=10^{9.5}\times\text{ones}(7,1)$. As mentioned above, for the identification process, both the white noise and ambient vibration responses are used together without any separation. The duration for the identification is approximately 33 s on a processor Intel® core™ i5 2400 K CPU @ 3.10 GHz.

Table 4-2: The building lumped seismic each floor mass and the web wall geometrical information.

Floor	Mass value (kg)	Initial stiffness (kN/m)	Wall thickness (m)	Wall width×length (m)
1	$m_1 = 3.3\times10^4$	$k_1 = 4\times10^7$	0.203	3.658 × 2.743
2	$m_2 = 2.9\times10^4$	$k_2 = 4\times10^7$	0.152	3.658 × 2.743
3	$m_3 = 2.9\times10^4$	$k_3 = 4\times10^7$	0.152	3.658 × 2.743
4	$m_4 = 3.07\times10^4$	$k_4 = 4\times10^7$	0.152	3.658 × 2.743
5	$m_5 = 2.9\times10^4$	$k_5 = 4\times10^7$	0.152	3.658 × 2.743
6	$m_6 = 2.9\times10^4$	$k_6 = 4\times10^7$	0.152	3.658 × 2.743
7	$m_7 = 2.5\times10^4$	$k_7 = 4\times10^7$	0.203	3.658 × 2.743

The estimated stiffness and damping values are shown in Figure 4-22 and Figure 4-23, respectively. Ideally, the estimated stiffness values should be compared to the results of the solo UKF using input excitations. However, Erazo and Nagarajaiah [72] noted that the solo UKF is unable in output-only parameter estimation of large state-space systems. Moreover, the information about the excitation is unclear. In fact, these are the evident limitations of the traditional Kalman filtering-based method. Therefore, instead of a direct comparison, we compared the natural frequencies calculated from the results obtained using our method to the natural frequencies from the existing studies [89, 92].

As expected, the calculated natural frequencies match well with the results of the other works, as shown in Table 4-3. For example, we compared our calculated natural frequencies with those calculated using stochastic subspace identification (SSI) [92, 93] and the multiple-reference natural excitation technique combined with the Eigensystem realization algorithm (MNExT-ERA) [92, 94]. Based on Table 4-3, the natural frequencies extracted from RD-UKF are in good agreement with the other two techniques for each damage state.

The estimated stiffness values in Figure 21 also show the same trend as the reduction tendency of the natural frequencies due to the accumulated damage within the seven-story structure. For example, it is expected that the stiffness value decreases when the level of damage increases from D0 to D4, as shown in Figure 21. The stiffness value k_1 gradually

decreases in the order of D0, D1, D3-2, D2, D3-1, and D4. The values of k_2, k_3, and k_4 decrease in the order of D0, D1, D2, D3-2, D3-1, and D4. Those of k_5 and k_6 decrease in the order of D0, D1, D2, D3-2, D4, and D3-1. The value of k_7 decreases in the order of D1, D0, D2, D3-2, D2, D4, and D3-1. Based on these results, we conclude that our proposed method could correctly estimate the stiffness values of the seven-story building.

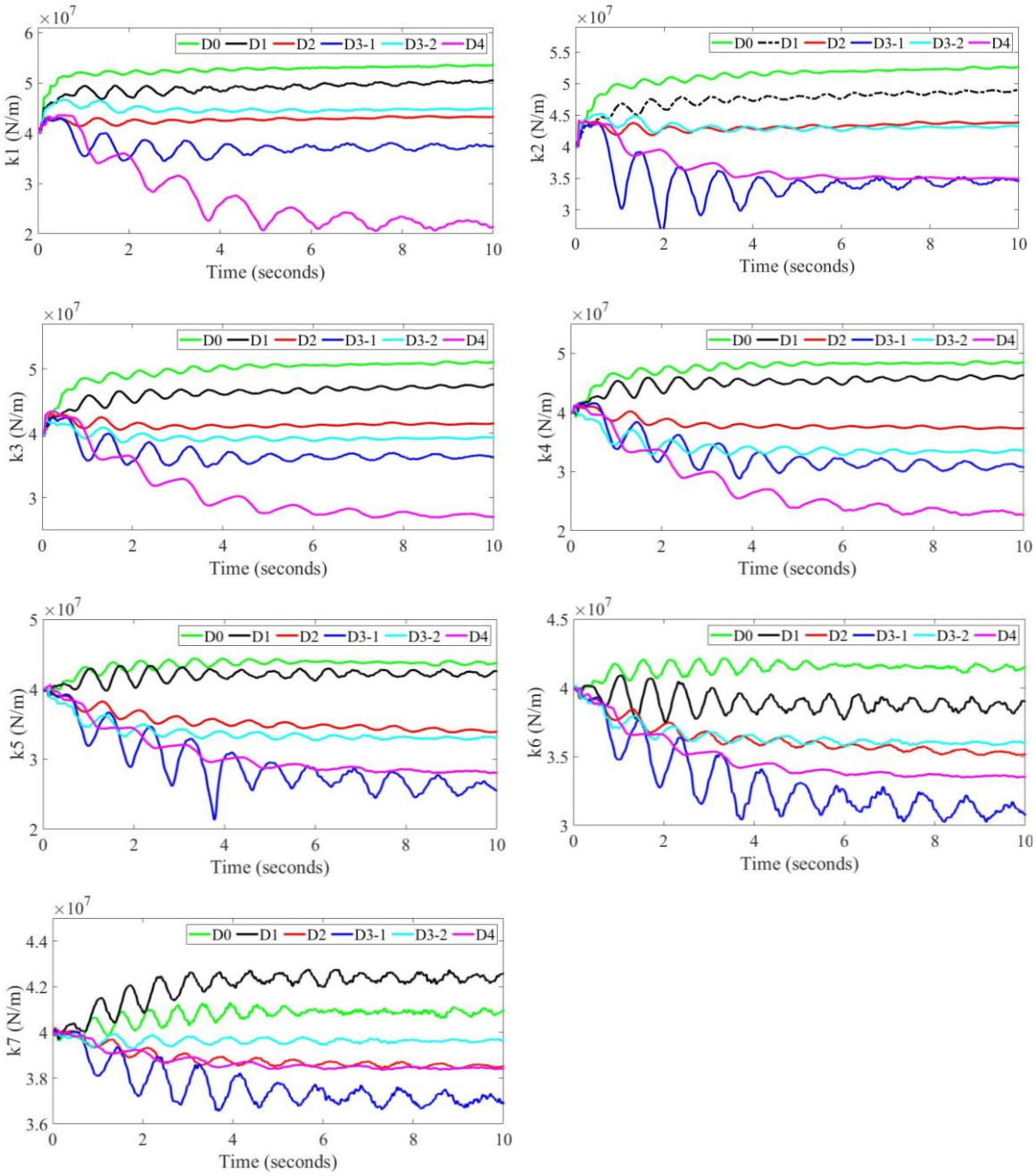

Figure 4-22: Estimated stiffness (k1– k7) values of the building within all damage states.

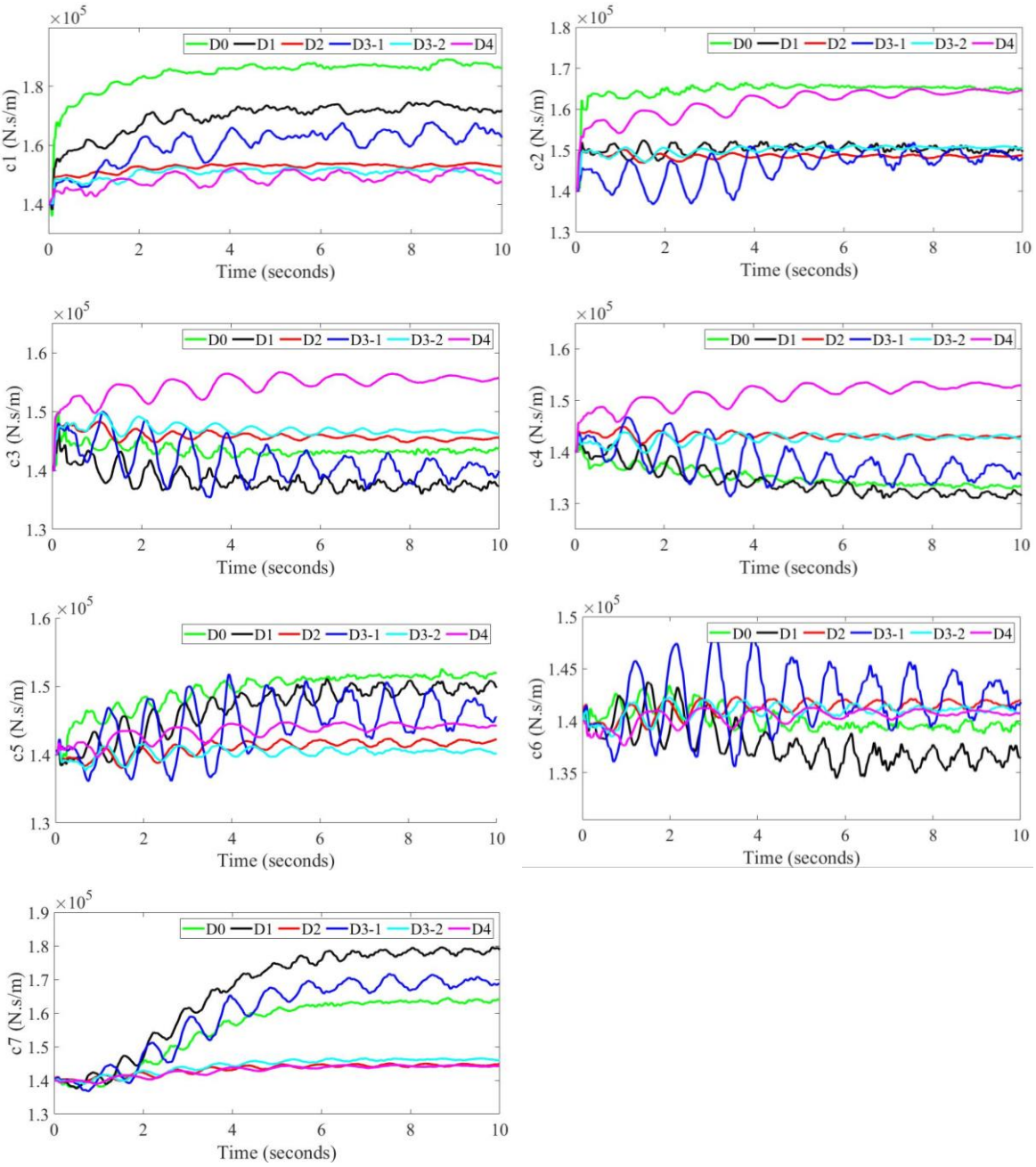

Figure 4-23: Estimated damping (c1– c7) values of the building within all damage states.

Two of the damage scenarios are more extended than the case of state D3-1, but we expect that the structure's stiffness increases somehow after this stiffening process because of the stiffening of the bracing system between the slabs of the building and the post-tensioned columns after this state of damage (D3-1) [89]. Then, based on Figure 4-22, the

damage state D3-1 will have a lower level of stiffness rather than D3-2 regarding this and what is mentioned in other work [92], which is evident in Figure 4-22, as well. Figure 4-22 shows that the estimated damping values do not follow a clear trend as a function of structural damage. The inaccuracy in the estimation of the damping matrix also has been seen in other works [39, 88, 92].

The 1st natural frequencies estimated by the RD-UKF in the D0 and D1 are slightly lower (i.e., 0.29 Hz) than those of the other two methods (i.e., MNExT-ERA and SSI), as shown in Table 3. However, the other two methods always provide different estimated natural frequencies for the same damage state under different excitations (i.e., 0.03g WN and AV). The discrepancies presented in Table 4-3 are a maximum of 0.55 Hz for the 1st natural frequency and 2.61 Hz for the 2nd natural frequency, respectively, which are nonnegligible discrepancies. However, the RD-UKF provides consistent estimated natural frequencies for the same damage state under different excitations that are more reasonable. The natural frequencies estimated by the RD-UKF show quite identical results for the different damage scenarios except D0 compared to those of the other two methods. Therefore, it appears that the estimated natural frequencies by the RD-UKF are more reasonable, based on the fact that we do not know the ground truth.

Table 4-3: Comparison of the extracted natural frequencies

State/ test No.	Method	0.03 g RMS WN		0.05 g RMS WN		AV		Discrepancy in	
		1st –L mode	2nd –L mode	1st –L mode	2nd –L mode	1st –L mode	2nd – L mode	1st NF	2nd NF
D0 test39	RD-UKF	1.4	11.1	–	–	1.4	11.1	0	0
	MNExT-ERA	1.71	11.49	–	–	1.92	10.49	0.21	1
	SSI	1.66	–	–	–	1.89	10.53	0.23	–
D1 test41	RD-UKF	1.37	10.01	–	–	1.37	10.01	0	0
	MNExT-ERA	1.54	11.35	1.39	10.78	1.86	10.27	0.47	1.08
	SSI	1.51	11.25	1.4	11.38	1.86	10.24	0.46	1.14
D2 test46	RD-UKF	1.25	9.25	–	–	1.25	9.25	0	0
	MNExT-ERA	1.22	10.88	1.12	10.41	1.67	10.34	0.55	0.54
	SSI	1.25	11.1	1.14	10.24	1.67	10.16	0.53	0.94
D3-1 test49	RD-UKF	1.15	8.54	–	–	1.15	8.54	0	0
	MNExT-ERA	1.11	10.24	1.05	10.22	1.46	10.60	0.31	0.38
	SSI	1.13	9.87	1.06	10.23	1.46	9.28	0.4	1.18
D3-2 test61	RD-UKF	1.22	9.01	–	–	1.22	9.01	0	0
	MNExT-ERA	1.18	11	–	–	1.58	8.39	0.4	2.61
	SSI	1.2	10.89	–	–	1.58	8.52	0.38	2.37
D4 test64	RD-UKF	0.97	7.9	–	–	0.97	7.9	0	0
	MNExT-ERA	0.83	4.68	0.8	4.62	1.02	5.68	0.22	1.06
	SSI	0.85	4.68	0.81	4.52	1.02	5.69	0.21	1.17

In general, the proposed method is defined for linear systems, while it is clear that damage leads to nonlinear behaviour in the system. Then, with increasing the level of damage, the assumption of a linear model for the UKF process is violated, and a quasi-linear or nonlinear model is suitable to represent the system behaviour. Defining a specific nonlinear precise model and customizing the RD technique for this nonlinear model will improve the estimated result dramatically, which will be considered in future works.

Furthermore, in contrast to other works which had separately identified the modal properties in two loading conditions (white noise excitation and ambient vibration), in this work, the data of both excitations are considered together, and we have shown that the

estimated stiffness values follow a clear trend as like as previous researches. This is another confirmation, emphasizing that this technique works for any kind of excitation.

The comparison of the performance of the technique with MCMC techniques shows that the computational time of the UKF-MCMC technique developed by Erazo and Nagarajaiah [72] for the UCSD experimental setup (case 6) was about 7 minutes, whereas that for the RD-UKF method was less than 33 s in a standard desktop computer. The UKF-MCMC method only used 1,000 samples for identification, which is a small number in the MCMC because of the burn-in phenomena of the algorithm. The RD-UKF used free vibration data with 2,400 samples (10 s with a sampling rate of 240 Hz). Furthermore, Figures 21 and 22 show that the algorithm reaches a steady condition just after 6 s. The RD-UKF technique is, therefore, significantly faster than the UKF-MCMC technique.

Constant values for the Q and R matrices are assumed during the estimation process since the condition of the model and the sensing systems are fixed throughout the estimation process of a simulation study. However, in real applications, assuming constant Q and R values will decrease the performance of the UKF. The harmonic errors observed in the figures are due to the R values, which are not adaptive to the system response. Obviously, the level of noise in a real measurement changes over time. To solve this problem, some researchers have suggested an adaptive adjustment of noise covariance for the Kalman filtering approach [95]. In the current study, the level of harmonic error decreased during the estimation time.

One limitation of the proposed method is that it does not follow a real-time scheme in the identification process, as RD is a data-driven approach and requires a set of measured time history data to extract the free vibration response of the structural system. Another limitation is that RD needs to be derived based on each specific problem. In other words, as RD was initially defined for linear systems, there is no general approach that can apply the technique in different nonlinear systems. It has to be separately solved case by case for different nonlinear systems. With this limitation considered and based on the inherent nonlinearity of the seven-story building, the UCSD case study, the small deviation in the estimated results from the comparison with previously published works can be justified because we used the linear RD procedure for the data of the seven-story building. However,

the estimated stiffness and corresponding natural frequencies are still consistent with the expected results compared with those of other published works.

4.5. **Conclusion**

A new hybrid output-only system identification method based on the Kalman filtering and the random decrement technique was proposed in this paper. Traditional methods have tried to identify or estimate the input excitation (step one) and use it for state estimation (step two) to estimate system parameters. However, in this proposed method, the output responses of the excited structural system were processed by the RD method to extract free vibration responses only. The extracted free vibration was inputted to the state-space equation of the Kalman filter to estimate the system parameters to detect structural damage. Therefore, the input excitation parameter was not involved in the state-space model because the free vibration dynamic equation of motion was used. It reduces the order of the state-space equation and also reduces uncertainties and complexities of the system.

Furthermore, the proposed method has advantages compared to the traditional output-only approaches:

1. The proposed method can detect, localize, and quantify the extent of damage, whereas data-driven methods can only cover the first two missions.

2. In contrast to pure model-based output-only system identification techniques, the proposed method works for high-dimensional state vectors by reducing the overall order of state-space equation though the removal of input excitation states.

3. The proposed method does not require any physics-based numerical model to estimate input excitations.

4. The technique reduces the complexities and uncertainties of the numerical model induced by the input excitation parameters while improves the observability rank of the system.

5. It is applicable to various systems subjected to different kinds of excitations (i.e., random noises, periodic excitations, and earthquake excitations) or any combination of these excitations.

6. The proposed method was validated for an actual large-scale structure by comparing its results against those of existing works.

The proposed hybrid method uses the positive point of RD to overcome the drawbacks of traditional model-based methods by using input excitations or related methods to replace the input excitations. These advantages demonstrate that the proposed method is more reliable and practical than pure data-driven or model-based methods, and it is applicable for the damage identification and quantification of large state-space systems. In the future, we will conduct more extensive numerical and experimental studies with more real cases, such as nonlinear systems and 3D frames. We will also conduct a sensitivity analysis of different tuning parameters for the RD and the UKF.

Chapter Five:

Analyzing the Robustness of Hybrid, Output-only Kalman Filtering–based System Identification Method

This chapter encloses the conference paper published in the 10th *European workshop on structural health monitoring*[1] introduced in the Co-authorship section. The paper has examined the performance and robustness of the RD-UKF method, which was introduced in Chapter 4. The method estimation accuracy and robustness were evaluated under different types of excitations, 100 independent simulations, missing sensor information, and uncertainty related to the structure's mass matrix. The mathematic basics related to each scenario are developed in this chapter, and the tuning parameters are mentioned for the sake of reproducibility for future readers. The results demonstrate that the method is robust to these worse-case scenarios associate with the identification process, and it is easy and straightforward to implement it on real structures.

---

1 **E. Ghorbani** and Y. J. Cha, "*Analyzing the robustness of hybrid, output-only, Kalman filtering–based system identification method*," 10th European Workshop on Structural Health Monitoring, Palermo, Italy, 225, November 2020.

Abstract: This paper investigates, in detail, the robustness of a previously introduced approach to output-only structural system identification using the random decrement method and unscented Kalman filter (RD-UKF) in chapter 4, [96]. Unscented Kalman filters have been widely used for structural system identification and damage detection purposes. These filter's divergence in estimating the desired states of a structural system with unknown excitations is a well-known weakness, considerably limiting their application. To overcome this difficulty, the current study initially employs the random decrement method to extract a system's free decaying response from its measured responses. Subsequently, it applies an unscented Kalman filter to the extracted free response in order to estimate the system's dynamic properties. Our previous study demonstrated this method's proficiency. The present study conducts further sensitivity analysis to show the RD-UKF method's robustness vis-à-vis different uncertainties in the process of identification. First, we estimate the stiffness and damping matrices of a three-degrees-of-freedom (DoF) system with three different kinds of excitations. Next, we examine the RD-UKF method's robustness in 100 experiments (Monte Carlo simulation). Besides, it will be shown that the method is robust in addressing uncertainties related to mass distribution and missing data (sensor malfunction or a loss of communication connectivity) during the modelling and measurement process. The results of the study show that the RD-UKF method is sufficiently robust for all the uncertainties of the system identification process.

5.1. **Introduction**

The structural damage identification process comprises three main steps: damage detection, damage localization, and damage quantification. Damage identification methods can be categorized into three groups: data-driven methods, model-based methods, and hybrid methods. Model-based methods use the advantages of a physics-based model, compared to data-driven approaches, to evaluate the extent of the damage. Recently, some studies have attempted to combine both model-based and data-driven approaches as a hybrid method in order to harness both method's advantages for damage identification purposes [60, 77, 97].

Measuring excitation is not viable in the course of the normal operation of many civil infrastructures for their damage identification purposes [60]. Many studies have attempted to identify a solution for extracting excitation information for the identification process during the last decade. As the first solution, shakers and actuators simulate excitations on the structure level, and the corresponding system response is used for damage identification. However, the shaker's' enormous mass changes a structure's modal parameters [9].

Estimating input with the help of a mathematical model and the measured response of the system using different methods, such as Kalman filtering, could constitute another approach. Joint input-state methods [66] and dual Kalman filtering [53] are two of the main methods that have been widely used for output-only system identification, utilizing this approach. The predicted state's accuracy strongly depends on the first Kalman filter's estimated input excitation [53]. Reconstruction of the input using mathematical methods [69]—such as autoregressive moving average (ARMA) methods, subspace methods [70], and Markov chain Monte Carlo (MCMC) methods [72]—is the third solution to unknown excitation problems. Selecting an appropriate sampling distribution plays a vital role in these kinds of approaches. Also, these approaches are not robust enough for combined excitations [72].

This study investigates the robustness of a previously introduced output-only damage quantification approach that takes advantage of both data-driven and model-based methods [96]. We believe that estimating input causes an estimation error during the damage identification process. We extract a free decaying response from the measured response of a structure using a data-driven method called random decrement (RD) [31], and we input the free-response into an unscented Kalman filter (UKF) for damage identification. This approach reduces the complexity and uncertainty of the physical model, and the combined method (RD-UKF) [96] could be used for damage identification of large-scale systems under the various kinds of loading involved in the identification process. Therefore, in this paper, we investigate the RD-UKF method's robustness in resolving various uncertainties associated with the structural damage quantification process.

This paper is organized as follows. Section 5.2 briefly introduces the basics of the RD and UKF methods. This section also presents RD-UKF's algorithm. Section 5.3 outlines

extensive studies on 1) RD-UKF's robustness for damage identification, using a 3-DoF numerical model subjected to three different loading conditions, 2) the method's robustness for about 100 Monte Carlo simulation experiments, 3) the method's robustness for uncertainty in a model's mass matrix, and 4) the effect of a missing sensor signal in the identification process, which could be due to sensor malfunction or a loss of communication connectivity. The results emphasize that the RD-UKF method is robust enough for all four cases of uncertainty.

5.2. **RD-UKF**

Conceptually, the vibration response $x(t)$ of a linear system subjected to any excitation consists of a linear combination of free and forced vibration responses, as expressed in Eq. (1).

$$\mathbf{x}(t) = \mathbf{x}(t)|_{x(0)} + \mathbf{x}(t)|_{\dot{x}(0)} + \mathbf{x}(t)|_{f(t)} \ . \tag{5.1}$$

The first two parts of Eq.(5.1), $\mathbf{x}(t)|_{x(0)} + \mathbf{x}(t)|_{\dot{x}(0)}$, refer to the system's free vibration response carrying information about the system's modal parameters and the third part of Eq.(5.1), $\mathbf{x}(t)|_{f(t)}$, returns to the forced vibration response. In this study, we eliminate the third part of the system's total vibration response using the RD method.

The RD method was proposed by Cole [31] to extract the free vibration response from the vibration response of a dynamic system subjected to random or ambient excitation. The method averages out the time segments of the measured responses with a standard initial or triggering condition. To implement the RD method, a trigger point $\sqrt{2}\sigma$ (σ is the standard deviation of the measured response) should be defined, and a segment of the signal is saved when the signal's amplitude yields the trigger point. The average of these segments represents the system's free vibration response (mathematically provable) [96]. The extracted free vibration response is input into the UKF to estimate the desired state.

UKF is a derivative-free Kalman filtering method defined for the state estimation of nonlinear systems [96]. This model-based method has been widely used for structural system identification and damage detection purposes [84, 98]. A discrete state-space model of the system has been derived to identify the system's dynamic properties, using UKF, as:

$$\mathbf{x}_{k+1,k} = G(\mathbf{x}_k, \mathbf{u}_k), \tag{5.2}$$

$$\mathbf{Y}_k = H(\mathbf{x}_{k+1,k}, \mathbf{v}_k). \tag{5.3}$$

Δt is a time-step, $\mathbf{x}_k$ is a state variable vector, $\mathbf{u}_k$ is process white noise, $\mathbf{Q}$ its covariance matrix, $\mathbf{Y}_k$ is the measurement vector, $\mathbf{v}_k$ is a discrete measurement noise vector, and $\mathbf{R}$ its corresponding covariance matrix. In contrast to the linear Kalman filter, the UKF propagates a set of predefined points named sigma points through the transition and measurement functions and calculates the covariance matrix in each iteration. Assuming prior information of a Gaussian distribution with mean $\mathbf{m}$ and covariance error matrix $\mathbf{P}_0^{XX}$, sigma points (χ^i) and their corresponding weights can be defined as follows:

$$\begin{aligned}
&\chi^0 = \mathbf{m}, && w_m^0 = \frac{\lambda}{n+\lambda},\\
&\chi^i = \mathbf{m} + \sqrt{\left((n+\lambda)\mathbf{P}_0^{XX}\right)}_i, \quad i = 1,2,....,n && w_c^0 = \frac{\lambda}{n+\lambda} + \left(1-\alpha^2+\beta\right),\\
&\chi^i = \mathbf{m} - \sqrt{\left((n+\lambda)\mathbf{P}_0^{XX}\right)}_{i-n}, \quad i = n+1, ...,2n && w_m^i = w_c^i = \frac{1}{2(n+\lambda)}, \quad i = 1,\ldots,2n,
\end{aligned} \tag{5.4}$$

where n is the number of states, λ is a scaling parameter, and i is a column vector number. Using these points and the state-space model, the algorithm for the proposed RD-UKF is followed by:

RD-UKF Algorithm

$\boldsymbol{\delta}_N(t)$ =**RD** ($\mathbf{x}(t)$, Δt),

Initialize trigger point (x_0), and segment length (τ), **set** $N = 0$,

for $t_r = 0 : \Delta t : t$,

if $x_j(t_r) \geq x_0$ for j[th] DoF,

save $\mathbf{x}(t_r + \tau)$, for all the DoFs

$N = N + 1$,

end if,

end for,

$$\boldsymbol{\delta}_N(\tau) = \frac{1}{N}\sum_{r=1}^{N} \mathbf{x}(t_r + \tau) .$$

($\mathbf{x}$, $\mathbf{P}$) =**UKF** ($\boldsymbol{\delta}_N(\tau)$, $G(\cdot)$, $H(\cdot)$)

initialize $\mathbf{x}_0$, and $\mathbf{P}_0$, and **set** $\mathbf{Q}$, $\mathbf{R}$, $\alpha, \beta,$ and κ .

for $i = 1 : \tau / \Delta t$

calculate, $\boldsymbol{\chi}$, and, W , using Eq. (5.4), and propagate $\boldsymbol{\chi}^i_{k+1|k} = F\left(\boldsymbol{\chi}^i_k, \mathbf{u}_k\right)$,

$$\mathbf{P}^{XX}_{k+1} = \sum_{i=0}^{2n} w^j_c \left[\boldsymbol{\chi}^i_{k+1|k} - \sum_{i=0}^{2n} w^j_m \boldsymbol{\chi}^i_{k+1|k}\right]\left[\boldsymbol{\chi}^i_{k+1|k} - \sum_{i=0}^{2n} w^j_m \boldsymbol{\chi}^i_{k+1|k}\right]^T + \mathbf{Q}_k ,$$

$$\mathbf{P}^{YY}_{k+1} = \sum_{i=0}^{2n} w^j_c \left[H\left(\boldsymbol{\chi}^i_{k+1|k}, \mathbf{v}_k\right) - \sum_{i=0}^{2n} w^j_m H\left(\boldsymbol{\chi}^i_{k+1|k}, \mathbf{v}_k\right)\right]\left[H\left(\boldsymbol{\chi}^i_{k+1|k}, \mathbf{v}_k\right) - \sum_{i=0}^{2n} w^j_m H\left(\boldsymbol{\chi}^i_{k+1|k}, \mathbf{v}_k\right)\right]^T + \mathbf{R}_k$$

$$\mathbf{P}^{XY}_{k+1} = \sum_{i=0}^{2n} w^c_i \left[\boldsymbol{\chi}^i_{k+1|k} - \sum_{i=0}^{2n} w^j_m \boldsymbol{\chi}^i_{k+1|k}\right]\left[H\left(\boldsymbol{\chi}^i_{k+1|k}, \mathbf{v}_k\right) - \sum_{i=0}^{2n} w^j_m H\left(\boldsymbol{\chi}^i_{k+1|k}, \mathbf{v}_k\right)\right]^T .$$

$$\mathbf{K}_{k+1} = \mathbf{P}^{XY}_{k+1}\left(\mathbf{P}^{YY}_{k+1}\right)^{-1},$$

$$\hat{\mathbf{x}}_{k+1} = \sum_{i=0}^{2n} w^j_m \boldsymbol{\chi}^i_{k+1|k} + \mathbf{K}_{k+1}\left(\delta_{k+1} - \sum_{i=0}^{2n} w^j_m H\left(\boldsymbol{\chi}^i_{k+1|k}, \mathbf{v}_k\right)\right),$$

$$\mathbf{P}_{k+1} = \mathbf{P}^{XX}_{k+1} - \mathbf{K}_{k+1}\mathbf{P}^{YY}_{k+1}\mathbf{K}^T_{k+1} .$$

end for

Figure 5-1: The RD-UKF algorithm

5.3. **RD-UKF robustness studies**

Extensive numerical studies have examined the robustness of the proposed output-only damage identification method. We should mention that the algorithm's tuning parameters are the same in all cases. Thus, the proposed technique is assured to be robust for tracking a system's clean stiffness values.

5.3.1. Case 1: 3-DoF system under different loading conditions

A 3-DoF damped mass-spring system was simulated in MATLAB software for 50 seconds with a sampling rate of 1,000 Hz. The mass, stiffness, and damping values were 500 kg, 50,000 N/m, and 300 N.s/m for each DoF, respectively. The input excitations are white noise with a power of 10^{-4}, the periodic force with a frequency of 2π, and the historic EI Centro earthquake as an ambient / shows the estimated stiffness and damping matrices for three different loading cases.

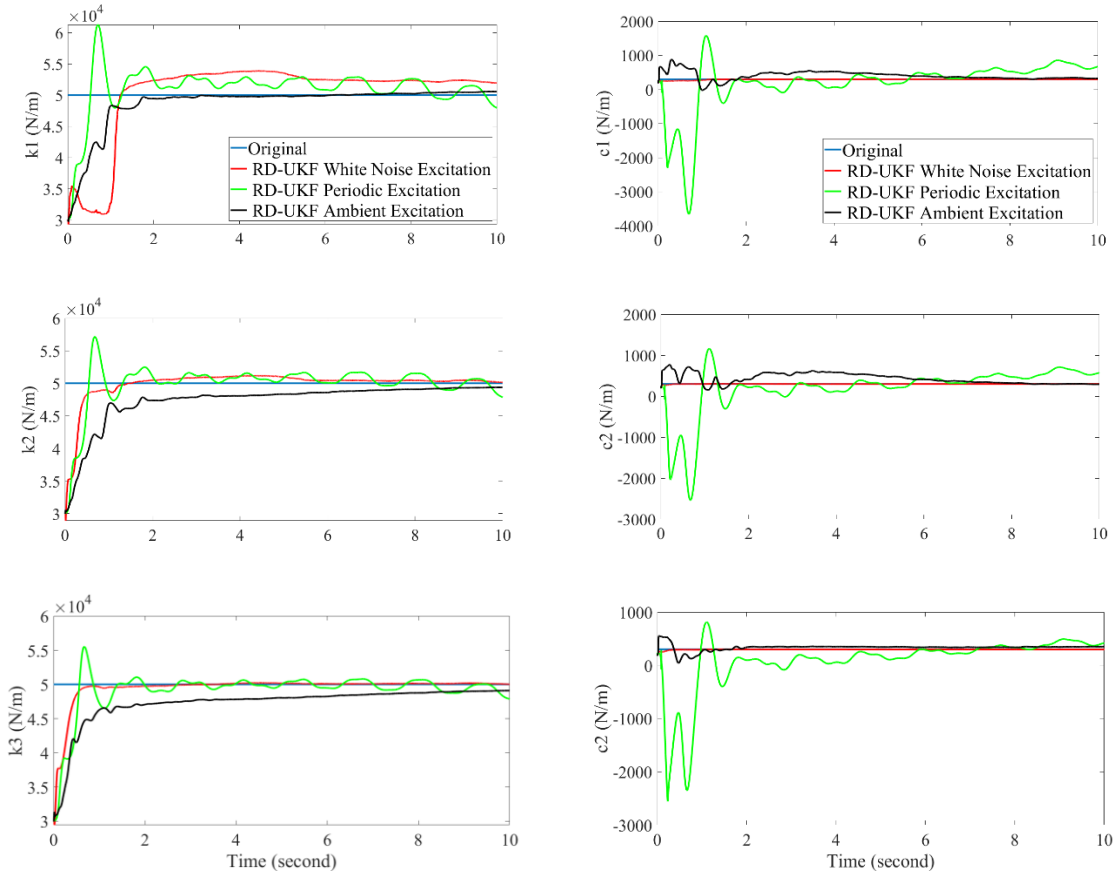

Figure 5-2: Estimated stiffness (left column) and damping values (right column)

Figure 5-2 shows that the RD-UKF method is capable of tracking a clean response for the three kinds of loadings. Only small fluctuations for the periodic forces were observed, which might be due to the elimination of periodic force from the measured response. For identification purposes, the RD method was used to extract the free vibration response data

with a selected trigger point equal to $0.3\sqrt{\text{var}(\ddot{\mathbf{x}}_1)}$ of the 1st DoF and 10 seconds selected as the segment length. Prior information on UKF for structural identification was assumed as $m = 500$ kg, $k = 30000$ N/m, $c = 200$ N.s/m, and $x = \dot{x} = 0$ for each DoF. Detailed information about the model's transition and measurement functions, as well as the procedure to remove the periodic signal from the measured acceleration response, is available in our previous work [96].

5.3.2. Case 2: RD-UKF robustness under Monte Carlo simulations

Because we were working with stochastic models and stochastic signals, Monte Carlo simulations were necessary to show the RD-UKF method's robustness under different initial conditions. Therefore, we generated 100 signal realizations using a simulation model with different seed numbers (that is, random signal generation), estimated the dynamics, and presented the estimates for all realizations. We also added white noise with a signal-to-noise ratio (SNR) of 30 to each measurement for a more realistic evaluation.

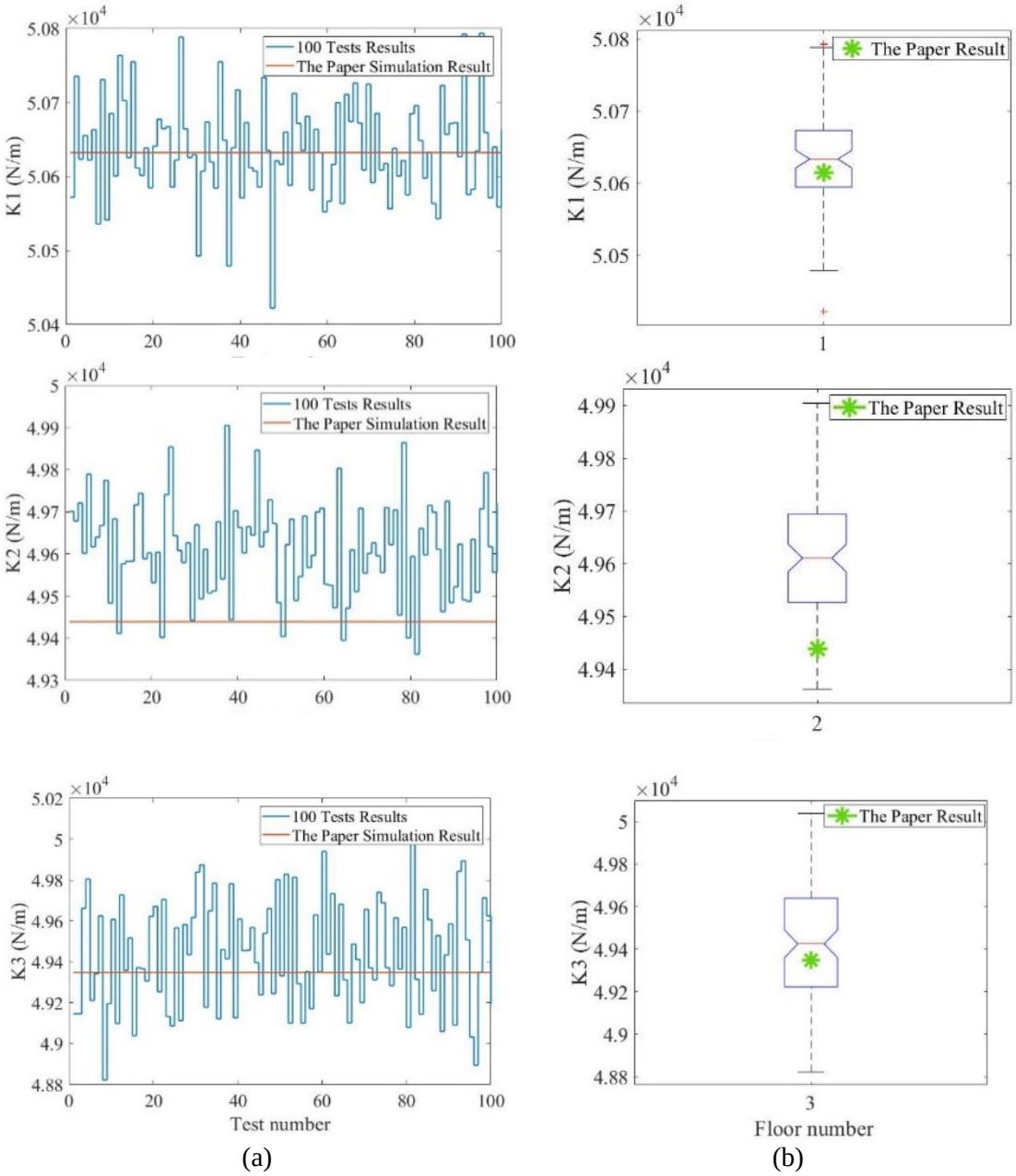

Figure. 5-3: a) Stair-step graphs and b) box-and-whisker plots, of stiffness values for each floor with 100 tests (signal-to-noise ratio = 30).

Figure. 5-3 shows that the error rates for k1–k3 are about 0.14%, 0.34%, and 0.18%, respectively. The error rates for C1–C3 are about 2.1%, 2.6%, and 2.3%, respectively, in Figure. 5-4. In Figure. 5-3 and Figure. 5-4, the orange lines are related to the estimated stiffness and damping value of the previous case study. It should be noted that different seed numbers are assigned to each test, and white noise (SNR = 30) is added to the measured signal. The figures show that the results are repeatable.

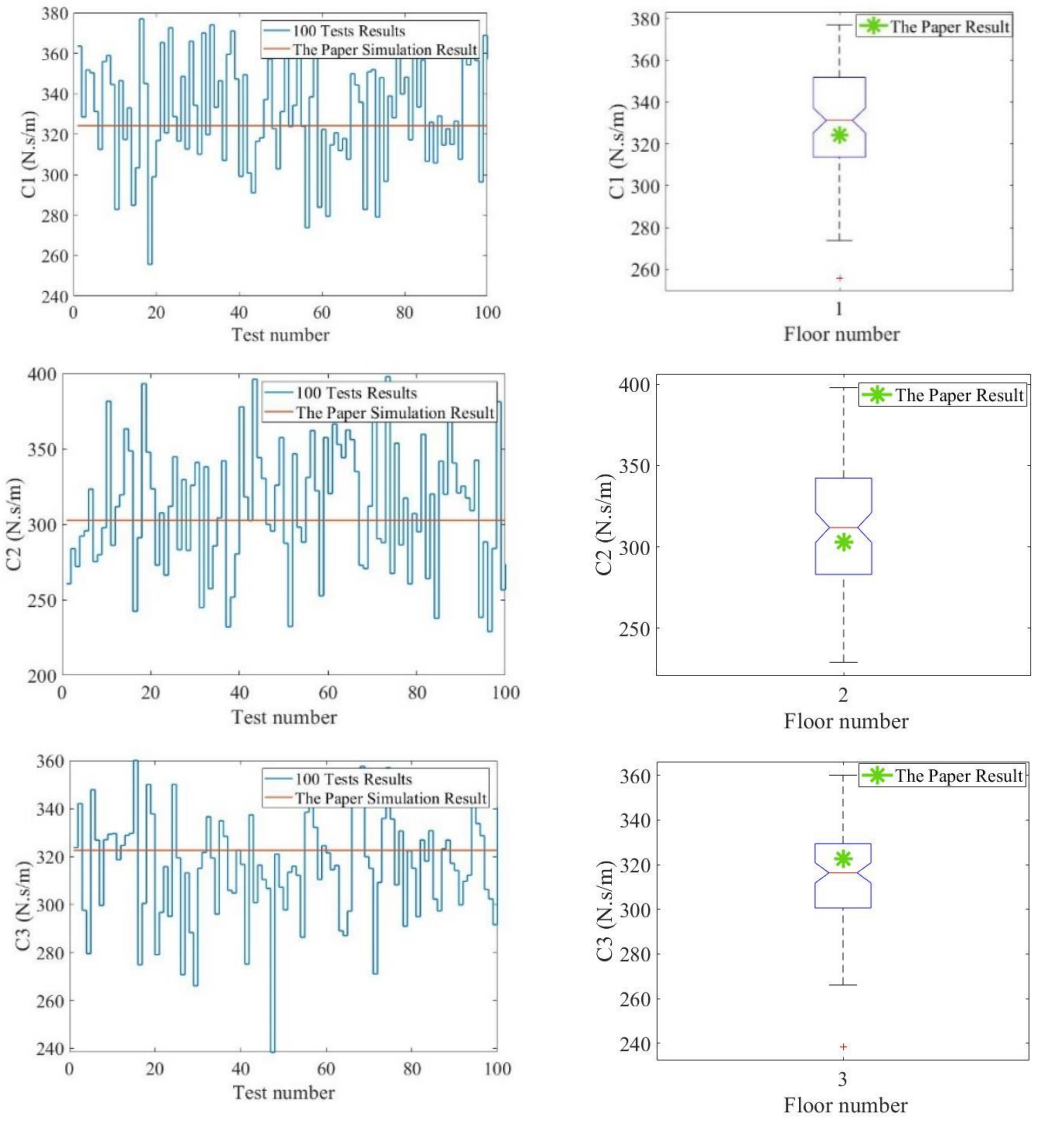

Figure. 5-4: a) Stair-step graphs and b) box-and-whisker plots, of damping values for each floor with 100 tests (signal-to-noise ratio = 30).

5.3.3. Case 3: Mass matrix sensitivity analysis

We examined the RD-UKF method's robustness vis-à-vis changes in stiffness and damping from the previous study [96], while we had assumed that enough information about the mass matrix is available. However, to show the method's proficiency regarding mass matrix uncertainty, we randomly changed the mass values in the transition and measurement functions by 5%. The updated transition and measurement equations are provided in Eq. (5.5) and Eq. (5.6). The estimated results are shown in Figure. 5-5.

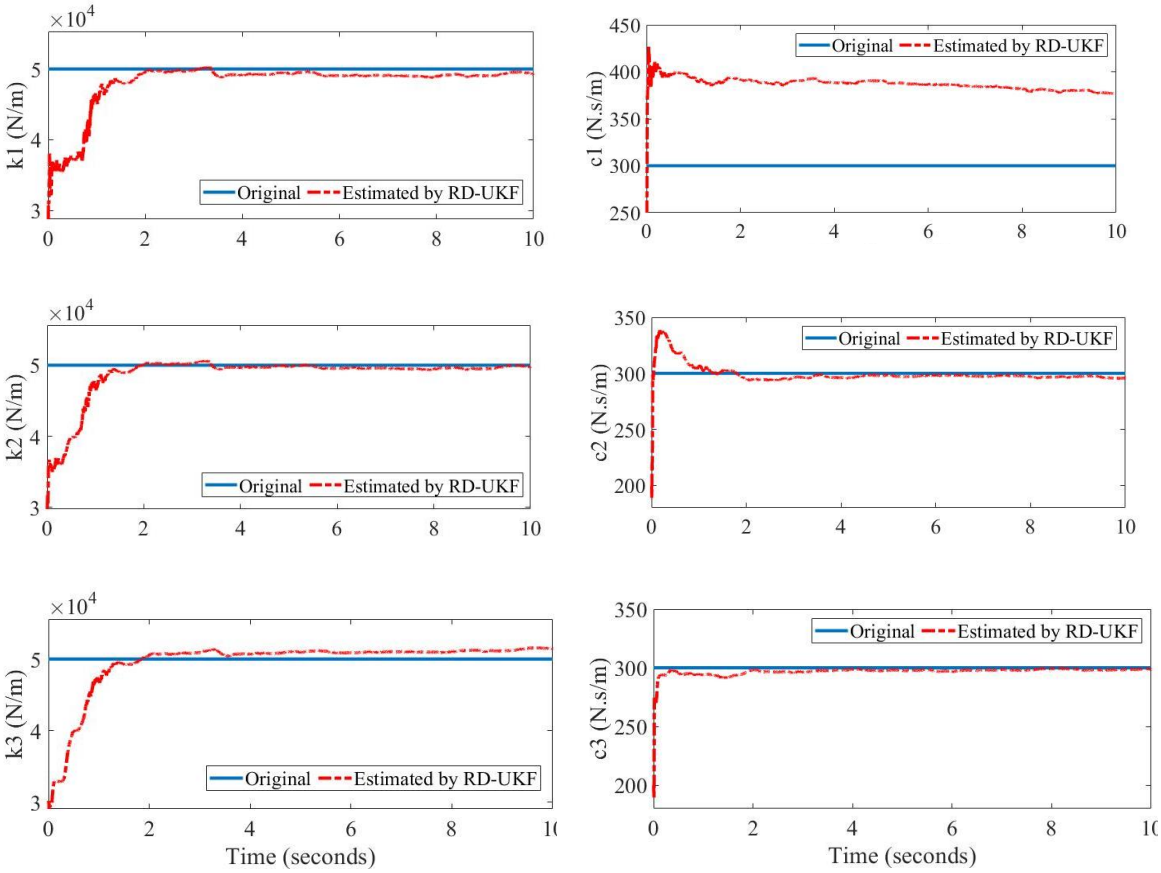

Figure. 5-5: Estimated stiffness (left column) and damping values (right column) of the model under mass distribution uncertainty.

$$\dot{\mathbf{x}} = \begin{Bmatrix} \dot{x}_1 \\ \dot{x}_2 \\ \dot{x}_3 \\ \ddot{x}_1 \\ \ddot{x}_2 \\ \ddot{x}_3 \\ \dot{k}_1 \\ \dot{k}_2 \\ \dot{k}_3 \\ \dot{c}_1 \\ \dot{c}_2 \\ \dot{c}_3 \end{Bmatrix} = \begin{bmatrix} x_4 \\ x_5 \\ x_6 \\ [-(x_7 + x_8)x_1 + x_8x_2 - (x_{10} + x_{11})x_4 + x_{11}x_5]/(m_1 + 0.05m_1) \\ [x_8x_1 - (x_8 + x_9)x_2 + x_9x_3 + x_{11}x_4 - (x_{11} + x_{12})x_5 + x_{12}x_6]/(m_2 - 0.05m_2) \\ [x_9x_2 + x_{12}x_5 - (x_{12}x_6 + x_9x_3)]/(m_3 + 0.05m_3) \\ 0 \\ 0 \\ 0 \\ 0 \\ 0 \\ 0 \end{bmatrix} + \mathbf{u}(t) = f(\mathbf{x}, t) + \mathbf{u}(t), \tag{5.5}$$

$$\mathbf{y} = \begin{Bmatrix} \ddot{x}_1 \\ \ddot{x}_2 \\ \ddot{x}_3 \end{Bmatrix} = \begin{bmatrix} -(x_7 + x_8)x_1 + x_8x_2 - (x_{10} + x_{11})x_4 + x_{11}x_5]/(m_1 + 0.05m_1) \\ [x_8x_1 - (x_8 + x_9)x_2 + x_9x_3 + x_{11}x_4 - (x_{11} + x_{12})x_5 + x_{12}x_6]/(m_2 - 0.05m_2) \\ [x_9x_2 + x_{12}x_5 - (x_{12}x_6 + x_9x_3)]/(m_3 + 0.05m_3) \end{bmatrix} + \mathbf{v}(t) = h(x, t) + \mathbf{v}(t). \tag{5.6}$$

Figure. 5-5 also shows that RD-UKF is not too sensitive to changes in mass. One damping value cannot track the correct response because of a significant difference in absolute values between K and C. This damping value deviation is inevitable, and it is a well-known limitation of Kalman filter-based system identification in many journal articles [39].

5.3.4. Case 4: Missing sensor sensitivity analysis

This section aims to show the RD-UKF method's robustness in situations where the response of some DOFs is not available (not measured due to an absence of sensors). For the 3-DOF system using earthquake excitation, we assumed that the second-floor acceleration response

was not available, and the estimated stiffness and damping values are shown here. Because we expected no differences in the transition function, we have just rewritten the new measurement function in Eq. (5.7).

$$\mathbf{y} = \begin{Bmatrix} \ddot{x}_1 \\ \ddot{x}_3 \end{Bmatrix} = \begin{bmatrix} -\left(x_7 + x_8\right)x_1 + x_8 x_2 - \left(x_{10} + x_{11}\right)x_4 + x_{11}x_5]/(m_1) \\ [x_9 x_2 + x_{12}x_5 - \left(x_{12}x_6 + x_9 x_3\right)]/\left(m_3\right) \end{bmatrix} + v(t) \tag{5.7}$$

$$= h(x,t) + v(t).$$

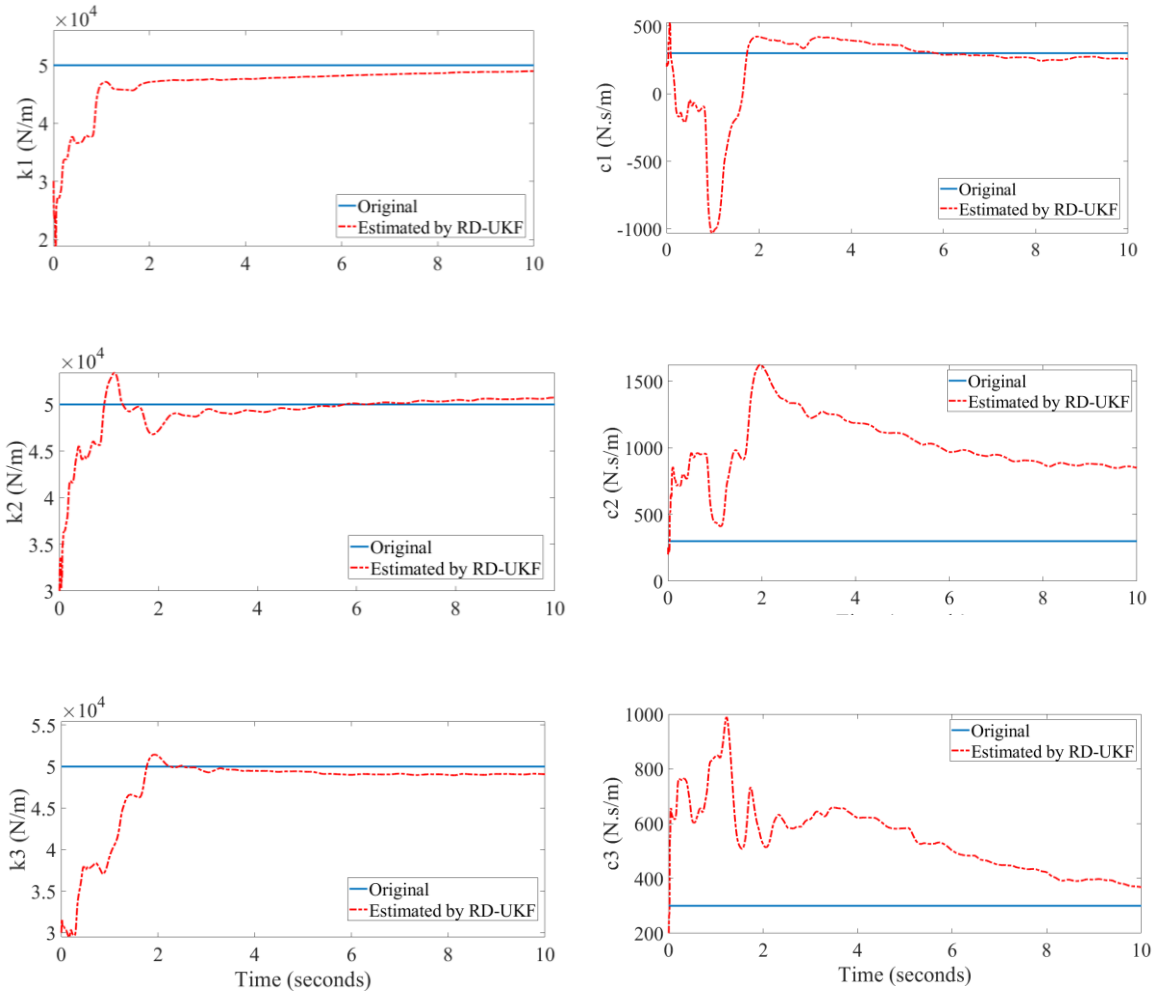

Figure. 5-6: Estimated stiffness (left column) and damping values (right column) of the model in missing-sensor situations.

Figure. 5-6 shows that the missing measurement has no significant effect on the stiffness estimation and that it only leads to some overestimation of damping values (c2), which we saw in our previous study as well [77]. However, we should mention that the RD-UKF method is more sensitive to missing information than mass matrix uncertainty. This difference in sensitivity could be due to the equation's stochastic nature, which yields uncertainties in the model while missing information reduces the rank of observability for the system as well as estimation accuracy.

5.4. **Conclusion**

This paper conducted a sensitivity analysis of a hybrid, output-only system identification method based on an unscented Kalman filter and the random decrement method (RD-UKF) [96]. The proposed hybrid method takes advantage of the RD to overcome the drawbacks of traditional model-based methods (which require both input and output for damage quantification). This study demonstrates that the RD-UKF method is robust, with various loadings exciting the structure and different initial conditions for different realizations. The study also examined the method's robustness vis-à-vis missing data and mass matrix uncertainty in the identification process. These extensive numerical investigations emphasize that the RD-UKF method is sufficiently capable of damage quantification in different real structural systems.

Chapter Six:

Bridge Pier Scour Level Quantification Based on Output-only Kalman Filtering

This chapter encloses the paper submitted in the peer-reviewed journal *Structural Health Monitoring*[1] introduced in the Co-authorship section. The paper initially develops a new physical model for a bridge pier, which is used for bridge scour quantification. The model is developed based on continuous Euler beam theory. With the advantage of the RD-UKF, an output-only scour quantification method is introduced, which only uses the vibration measured from the top of the bridge pier. The method is numerically evaluated with the help of MATLAB software, and it is shown that it is capable of scour quantification. In the next step, the acceleration of vibration at the top of a bridge pier is measured for scour quantification. The method estimates the height of soil around the pier, which is in agreement with the independent bathymetry carried around the pier simultaneously with the vibration measurement.

---

1 E. Ghorbani, D. Svecova, D. J. Thomson and Y. J. Cha, "*Bridge pier scour level quantification based on output-only Kalman filtering*", Journal Structural Health Monitoring, [Submitted Dec. 22, 2020].

Abstract: Soil scour near a bridge pier foundation is one of the leading causes of bridge failures. Traditional vibration-based scour monitoring methods are nearly incapable of quantifying scour levels using a single acceleration response without knowledge of excitation information. In this paper, a new output-only scour level prediction method is introduced via the integration of an unscented Kalman filter, random decrement, and newly derived continuous Euler beam addressing river water, traffic loads, and the linear and nonlinear behaviour of sediments around the pier as external effects. We conducted extensive simulation studies and applied this method to an existing medium span bridge with a steel girder and concrete deck in service in the province of Manitoba, Canada. These studies show that our proposed method can accurately estimate scour levels using only one accelerometer, which was validated by an independent bathymetric survey of the soil level at the pier foundation. Furthermore, three different linear and nonlinear soil profiles representing the soil behaviour around the pier were investigated as case studies in the scour level prediction process. The results confirm that a cubic function exhibits the best performance in the quantification of the scour level around bridge piers.

6.1. **Introduction**

Scour is one of the leading causes of bridge failures, which happen suddenly without any warning [99]. Until 2010, around 80 percent of 614,387 bridges in the United States were built over water streams, and all of these bridges experienced floods frequently during their life spans [20, 100]. Failure analysis of 1,000 bridges in the U.S. determined that foundation scour was the first cause of failure for about 60 percent of bridges [100]. Therefore, developing a scour monitoring system is critical to prevent catastrophic bridge failures in transportation systems. The failures of the Bonnybrook Bridge in Calgary in 2013 and the I-10 bridge in southern California in 2015 are two recent notable cases of bridge failure in North America due to scour around their piers and abutments.

Many approaches have been proposed to detect scours or quantify the severity of scours around the foundations of bridge piers and abutments. These approaches can be categorized into two groups. The first group focuses on directly measuring scour depth using

instruments installed in critical places under the water. The most straightforward technology uses buried switches, which detect the scour when it reaches the buried sensors [101]. However, these sensors are only for one-time use, and the sensor installation process is challenging. Other research has used electromagnetic signals to track changes in physical properties in areas where soil and water interact [102]. With this technique, it is almost impossible to replace the sensor in the case of damage or dysfunctionality. Placing a gravity rod protected by tubes beside the bridge pier has been another approach. The rod moves down when the soil level goes down due to scour [103]. However, the protection of these tubes during the flood season is a massive challenge considering the processes involved in their reinstallation and calibration [104]. Some other techniques, such as fibre sensors [105], piezo sensors, [106] and electrical conductivity devices [107] are also used for scour monitoring.

Electromagnetic sensors are another type of probe that have been installed around bridge piers and piles to track changes in the dielectric permittivity of the surrounding bridge foundation [108]. These wireless probes send information about the scour depth and hole refill in a real-time manner [109]. Still, the installation of these probes, their protection during flood season, and the calibration of the sensor response after flood seasons are significant challenges associated with these sensors. Recently, a technology called “BridgeCat” [110] has been used in the U.K. that puts a sonar scanner, a high-resolution camera, and a digital altimeter on a hydraulic arm. The whole system is installed on a vehicle, and the riverbed height is measured using these sensors. This technique is costly and requires closing the bridge, causing traffic issues [111]. Considering the pros and cons of the direct approaches, they are expensive, and most of them are one-time use only. Also, the uncertainty related to the measurement due to the nature of sensors installed underwater is a big challenge for these kinds of methods [112]. Therefore, structural vibration-based methods have been developed to overcome the disadvantages of direct methods [113].

The second group of approaches uses changes in dynamic modal properties (e.g., natural frequencies and mode shapes) due to scour in piers and foundations by analyzing vibration measurements [114, 115]. The stiffness of a bridge pier depends on the mechanical properties of its structural components and their boundary conditions. Scour phenomena

change the boundary condition of a bridge pier by reducing the height of the soil that supports the pier and pier foundation. Consequently, the stiffness of the pier is changed, which changes the natural frequencies and mode shapes. Many researchers have reported that the natural frequencies of bridges were reduced due to increased scour depth [116, 117]. Therefore, to facilitate the use of changes in natural frequencies and mode shapes due to scour, researchers have developed a bridge-soil interaction model using the finite element method (FEM) [118]. The core concept of this method is to compare the natural frequencies calculated from actual measurements with the natural frequencies calculated from the developed tuned models. As the comparison index, a frequency response function (FRF) with the Winkler model considering the mass of soil surrounding the pier was used, and modal updating using an iterative method was conducted [119]. The limitation of this method is that it requires a specific vehicle FEM model in the developed bridge-soil interaction model; therefore, its application is limited to problems subjected to a specific vehicle vibration only.

Xiong et al. [120] used a flexibility matrix based on FEM to predict the scour level in a bridge pier. The flexibility matrix is a combination of natural frequencies and their mode shapes. Some experimental studies have been conducted to investigate the effects of scour on the change of mode shapes [121]. Choudhury et al. [122] developed a FEM model and updated the model with the actual natural frequencies of the pier; they then used the updated model to estimate scour depth with empirical equations and a modal updating process. To apply these methods to real structures, the mode shapes are required, but it is very challenging to extract accurate mode shapes from measured vibrations, which also requires that many sensors be installed. Furthermore, these methods require very accurate modal updating, and it is unclear which mode shapes and natural frequencies should be used; therefore, extensive simulations and case studies are required to determine sensitive modal properties. Palanisamy and Sim [123] used an extended Kalman filter (EKF) to estimate the change in foundation stiffness due to scour. This method requires accurate excitation time history information and its structural responses, but measuring excitation is very challenging, and the EKF does not perform well in predicting complex FEM model parameters.

The literature above shows that traditional approaches can detect whether a scour has occurred using natural frequencies or can localize the scour by comparing the mode shapes

of bridge systems. Some of these approaches require specific excitations, such as impact or cyclic loadings, or specific loading such as a specific vehicle type, while most can quantify the level of scour to some degree using ambient vibration data.

In this paper, an output-only Kalman filtering–based scour quantification approach is proposed with a continuous Euler beam model of a bridge pier that considers the soil-bridge interaction. The advantages of this proposed method include the following: 1) the proposed method does not require many sensors; rather, only a single accelerometer is attached to the top of the pier close to the girder; 2) the proposed method does not require information on excitation sources in that it can consider any type of excitation source, such as ambient vibration, impact, or vehicle-induced vibration, etc.; 3) this method can quantify the scour level of the bridge pier; and 4) the different boundary conditions of bridge piers and different soil properties can be considered.

This paper is organized as follows: In Section 6.2, the continuous governing equation of motion of a bridge pier is developed based on the Euler beam theory. This model is used for the state-space formulation of Kalman filtering; then, we introduce the unscented Kalman filter (UKF) [28]. Original UKF needs corresponding measured excitation information for estimation, while it is not viable to measure the bridge excitations [124]. Therefore, the random decrement technique [96, 125]is introduced as a data-driven technique that extracts the free vibration of a bridge pier, which is used as an input of the UKF to predict the scour level. In Section 6.3, two illustrative systems are selected to demonstrate the efficacy of the proposed method. At first, simulation studies are done to show the capability of the proposed method. As a full-scale experiment, the proposed method is validated with the vibration data measured from an in-service bridge pier located in the province of Manitoba, Canada. A survey and an Acoustic Doppler Profiler (ADP) system are used to measure the soil level around the pier of interest to verify the estimated results of the proposed method.

6.2. **Proposed method**

In order to predict the scour level, a physics model-based scour prediction method is proposed. The proposed method is composed of the random decrement (RD) method and the UKF. The role of RD is to extract free vibration responses from the ambient acceleration vibrations measured from the accelerometer installed on a bridge pier. The extracted free vibration response is fed into the UKF to predict the soil level, an indicator of the scour level. The UKF estimates the variables of the state-space equation with a newly developed continuous Euler pier model. Therefore, the proposed scour monitoring method is an output-only approach, since it does not use any bridge excitation information Figure. 6-1. The proposed method's details, including the RD, UKF, and newly developed continuous Euler pier model methods, are described in the next sections.

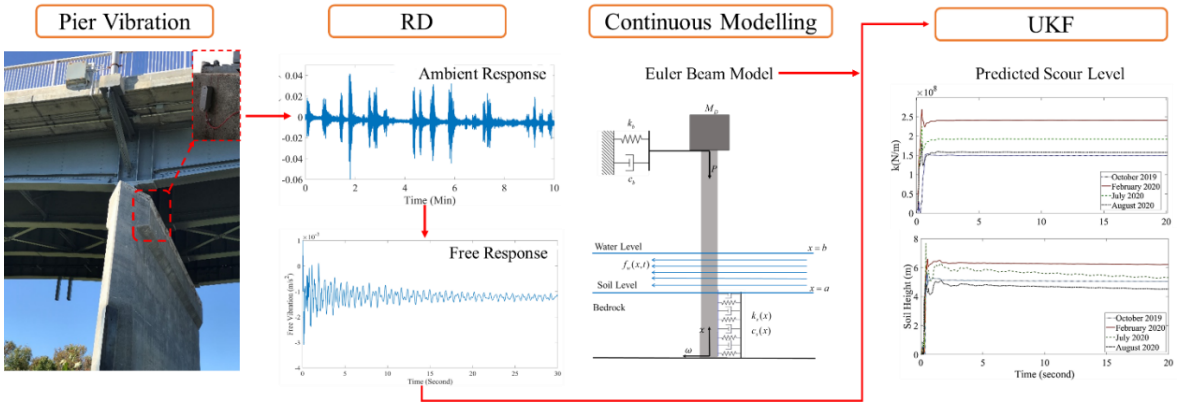

Figure. 6-1: Overall procedure of the proposed method

6.2.1. **Random decrement method**

RD is a data-driven algorithm for extracting the free vibration response of a dynamic system from its measured response and subjected to random or ambient vibrations. The technique averages out to a finite number (r) of segments, $\mathbf{x}_j(t_r+\tau)$, with length τ from the response measured when the signal amplitude reaches a specific trigger threshold point (θ) for the first time, as shown in Figure. 6-2.

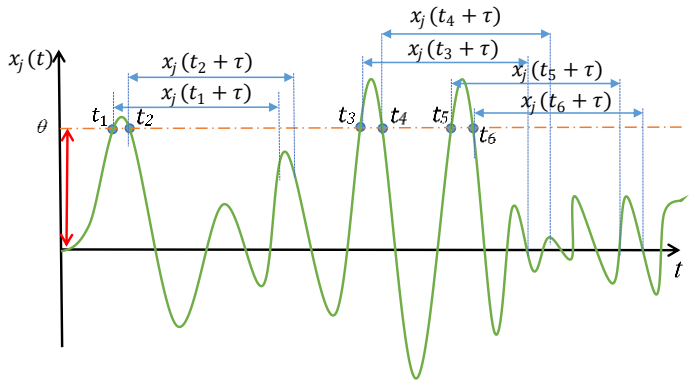

Figure. 6-2: Schematic view of the RD method

$\mathbf{x}_j(t)$ is the jth measured response of the system, e.g., it can be the acceleration response of a bridge pier, and the trigger threshold point (θ) set on the signal usually equals $\sqrt{2}\sigma$ (σ is the standard deviation of the time history response), as proposed by Brincker and Rodrigues [124]. When the signal reaches a trigger point, a segment of the signal is stored. The free vibration response, $\boldsymbol{\delta}_j(t)$, is then calculated by averaging these segments as formulated in Eq. (6.1). The initial idea of the method was developed for the system subjected to random excitations. However, it works for impact and ambient excitations as well. More detail on the algorithm with the mathematical background is available in [96].

$$\boldsymbol{\delta}_j(t) = \frac{1}{\tilde{N}} \sum_{r=1}^{\tilde{N}} \mathbf{x}_j(t_r + \tau). \tag{6.1}$$

where $\tilde{N}$ is the number of extracted segments from each measurement. Increasing the number of segments improves the accuracy of the extracted free vibration response.

6.2.2. Eulerian beam model for a bridge pier

In this paper, the UKF uses the extracted free vibration, $\boldsymbol{\delta}_j(t)$ in Eq. (6.1) by the RD algorithm, to estimate the scour level around the pier foundation. To determine the level of scour, we track the changes in the soil stiffness and damping values of the underlying pier. The changes in these values are predicted by the UKF using a state-space equation, which is

driven from the dynamic equation of pier motion. Therefore, we establish a dynamic equation of motion by developing a continuous Euler beam model for a bridge pier in this section. A schematic view of the bridge pier is shown in Figure. 6-3. ω is the transverse displacement of a beam (i.e., pier), P is an axial force due to the mass of the bridge deck (M_D), k_s is stiffness, and c_s is the damping of the soil over time, t, respectively. Also, k_b and c_b denote the stiffness and damping of the rocker bearing in this study, respectively.

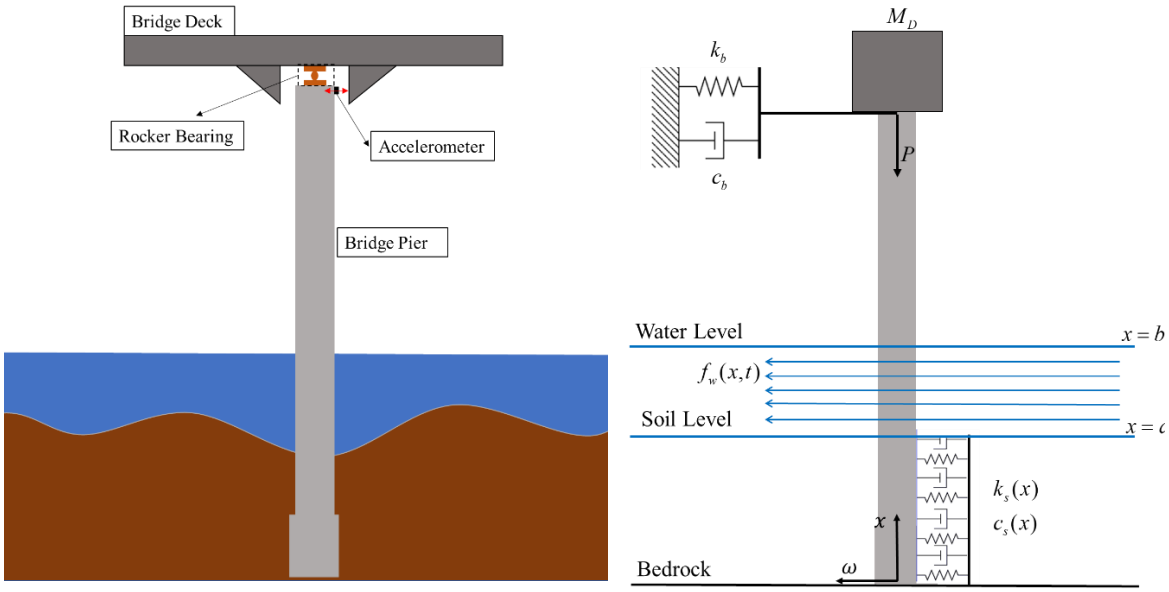

Figure. 6-3: Schematic view of Euler beam model of a bridge pier with rocker bearings

Considering an Euler beam with a modulus of elasticity *E*, moment inertia *I*, cross-section area A, and density of the bridge pier ρ, the beam partial differential equation is written as:

$$\mathrm{EI}\frac{\partial^4\omega(\mathrm{x},\mathrm{t})}{\partial \mathrm{x}^4}+\rho\mathrm{A}\frac{\partial^2\omega(\mathrm{x},\mathrm{t})}{\partial \mathrm{t}^2}+\mathrm{P}\frac{\partial^2\omega(\mathrm{x},\mathrm{t})}{\partial \mathrm{x}^2}=\mathrm{F}(\mathrm{x},\mathrm{t}), \tag{6.2}$$

where t is time, and $\mathrm{EI}\frac{\partial^4\omega(\mathrm{x},\mathrm{t})}{\partial \mathrm{x}^4}$ is defined as the relationship between the bending moment and deflection based on Euler beam theory: $\mathrm{M}(\mathrm{x},\mathrm{t})=\mathrm{EI}\frac{\partial^2\omega(\mathrm{x},\mathrm{t})}{\partial \mathrm{x}^2}$. M is the bending moment through the centroidal axis of the beam. $\rho\mathrm{A}\frac{\partial^2\omega(\mathrm{x},\mathrm{t})}{\partial \mathrm{t}^2}$ is the inertia force of the beam, and

$P\frac{\partial^2\omega(x,t)}{\partial x^2}$ is given by the dead weight of the bridge decks and girders, while the external force $F(x,t)$ is applied as water flowing around the pier:

$$\begin{aligned} F(x,t) &= f_{water}(x,t)[H(x-a)-H(x-b)] \\ &\quad - k_s\omega(x,t)[H(x)-H(x-a)] - c_s\frac{\partial\omega(x,t)}{\partial t}[H(x)-H(x-a)] \\ &\quad - k_b\omega(x,t)\delta(x-L) - c_b\frac{\partial\omega(x,t)}{\partial t}\delta(x-L) - M_D\frac{\partial^2\omega(x,t)}{\partial t^2}\delta(x-L), \end{aligned} \tag{6.3}$$

while δ_{nm} is the Dirac delta function, and $H(x-x_0)=\begin{cases}1 & x\geq x_0\\ 0 & x<x_0\end{cases}$ is the Heaviside function. For any arbitrary function, $g(x)$, $\int_0^L g(x)H(x-x_0)dx=\int_{x_0}^L g(x)dx$, where x_0 is a constant value in the domain $[0, L]$, and L is the length of the pier.

Based on the assumed mode approach [126], $\omega(x,t)=\sum_{n=1}^{N}X_n(x)q_n(t)$ is defined, where N is the number of modes, $X_n(x)$ is the mode shape function of the beam for each mode, and $q_n(t)$ is a time-depended generalized coordinate function [127]. $\omega(x,t)$ is substituted in Eq. (6.2) and Eq. (6.3), respectively. Considering the orthogonality of the mode shapes, $\int X_n(x)X_m(x)dx=\delta_{nm}$, the equation is integrated over the length of the beam, and each component with a Dirac function is zero when $m\neq n$ (The derivation is detailed in Appendix D). Considering the mode shape orthogonality as follows:

$$\begin{aligned} &(\rho A B_{mn} + M_D X^2{}_m(x=L))\ddot{q}_n(t) + (c_s D_{nm} + c_b X^2{}_m(x=L))\,\dot{q}_n(t) \\ &+ [EI V_{mn} + P Q_{mn} + k_s D_{nm} + k_b X^2{}_m(x=L)]q_n(t) = \int_a^b f_{water}(x,t)X_m(x)dx, \end{aligned} \tag{6.4}$$

where

$$V_{mn} = \int_0^L X_m(x)X_n^4(x)dx, \quad B_{mn} = \int_0^L X_m(x)X_n(x)dx,$$
$$Q_{mn} = \int_0^L X_m(x)X_n''(x)dx, \quad D_{nm} = \int_0^a X_n(x)X_m(x)\,dx. \tag{6.5}$$

The following equation derived from Eq. (6.4)has a standard dynamic equation of motion form as follows:

$$\mathbf{M}\ddot{\mathbf{q}}(t) + \mathbf{C}\dot{\mathbf{q}}(t) + \mathbf{K}\mathbf{q}(t) = \mathbf{F}(t), \tag{6.6}$$

where $C_{mn} = c_s D_{nm} + c_b X^2{}_m(x = L)$, and $K_{mn} = EI V_{mn} + PQ_{mn} + k_s D_{nm} + k_b X^2{}_m(x = L)$, $M_{mn} = \rho AB_{mn} + M_D X^2{}_m(x = L)$, and $F_m(t) = \int_a^b f_{water}(x,t)X_m(x)\,dx$. This set of equations can be numerically simulated based on different boundary conditions. This study assumes a fix-free boundary condition in which the corresponding mode shape function is introduced in the following section.

6.2.3. Kalman filtering

Kalman filtering [34, 128] is a type of Bayesian recursive filter assuming a Gaussian distribution for measured data and a least square loss function in a Bayesian inference framework. A linear Kalman filter works for a limited number of states showing linear behaviour. An extended Kalman filter (EKF) [129] is defined to compensate for the linear Kalman filter's incapability for nonlinear systems identification. The EKF works based on the first-order linearization of the Taylor series, but it still does not estimate an actual value for systems with a high level of nonlinearity. Besides, for the first-order Taylor series, the derivative of the transition and measurement function needs to be calculated, which is in some cases hardly viable [27]. The UKF, is a derivative-free filter, developed to answer the drawbacks of the EKF. The UKF tries to approximate the distribution of the states of the dynamic equation of motion (Eq. (6.6)) using carefully chosen sigma points instead of approximating nonlinear functions. There have been some applications and improvements of the UKF due to damage identification problems in structural systems [77, 130, 131]. In this paper, we use the UKF for scour detection and quantification around a bridge pier. We

need to convert Eq. (6.6) into a state-space form considering the desired states for estimation purposes.

The transition and measurement functions of a dynamic system in a general form of the state-space model in the discrete domain are defined as follows:

$$\mathbf{X}_{k+1|k} = \mathrm{F}(\mathbf{X}_k, \mathbf{u}_k, \mathbf{z}_k), \tag{6.7}$$

$$\mathbf{Y}_k = \mathrm{H}(\mathbf{X}_{k+1|k}, \mathbf{u}_k, \mathbf{v}_k), \tag{6.8}$$

where k is a time step, $\mathbf{X}_k$ is a state variable vector, and, in the simplest form, it could be equal to $\mathbf{X}_k = \{\mathbf{q}(k\Delta t) \quad \dot{\mathbf{q}}(k\Delta t)\}^T$ in Eq. (6.6). It could also include any other parameter desired to be estimated, like the stiffness and damping of a structure. $\mathbf{z}_k$ is a discrete process white noise, $\mathbf{Q}$ is its covariance matrix, $\mathbf{Y}_k$ is the simulation measurement (simulation output) vector, $\mathbf{v}_k$ is a discrete measurement process noise vector, and $\mathbf{R}$ is its covariance value. $\mathbf{u}_k$ is the excitation vector, which can have any form of white noise and stationary excitation, periodic excitation, ambient vibration, or any combination.

To begin the UKF algorithm, we take advantage of some predefined points, sigma points, to approximate the desired parameter distributions of each iteration. Let us assume $\mathbf{X}_0$ is an initial value for a desired state vector and $\mathbf{P}_0$ is its covariance error matrix; then, the equations Eq. (6.9) to Eq. (6.11) need to be solved to find the sigma points.

$$\sum_{i=0}^{2n_s} w_i = 1, \tag{6.9}$$

$$\sum_{i=0}^{2n_s} w_i \boldsymbol{\chi}_i = \mathbf{X}_0, \tag{6.10}$$

$$\sum_{i=0}^{2n_s} w_i \left(\boldsymbol{\chi}_i - \mathbf{X}_0\right)\left(\boldsymbol{\chi}_i - \mathbf{X}_0\right)^T = \mathbf{P}_0, \tag{6.11}$$

where $\boldsymbol{\chi}$ is a sigma point, w is the corresponding weight, and n_s is the number of states. There is not a unique solution for the above system of equations. The most common solution, sigma points, of the above three equations are given below.

$$\boldsymbol{\chi}_{0,0} = \mathbf{X}_0 \ , \ \boldsymbol{\chi}_{i,0} = \mathbf{X}_0 + \sqrt{\left((n_s + \lambda)\mathbf{P}_0\right)}_i \ , \ \boldsymbol{\chi}_{i+n,0} = \mathbf{X}_0 - \sqrt{\left((n_s + \lambda)\mathbf{P}_0\right)}_{i+n_s}, i = 1, 2, ..., n_s, \tag{6.12}$$

where λ is a scaling parameter, and i is the index of column vector number. With the sigma points, the weighting functions can be calculated, as shown below:

$$w_0^m = \frac{\lambda}{n_s + \lambda}, \qquad w_0^c = \frac{\lambda}{n_s + \lambda} + \left(1 - \alpha^2 + \beta\right), \qquad w_i^m = w_i^c = \frac{1}{2\left(n_s + \lambda\right)}, \quad i = 1, \ldots, 2n_s, \tag{6.13}$$

where α determines the spread of the sigma points and is a positive number $(0 \le \alpha \le 1)$, and $\lambda = \alpha^2(n_s + \kappa) - n_s$. κ is a secondary scaling parameter, which usually equals $3 - n_s$. $\beta = 2$ is optimal for Gaussian distributions.

For each time step k, the UKF procedure is presented in Eq. (6.12) to Eq. (6.21), and more detail can be found in [28].

$$\bar{\boldsymbol{\chi}}_{i,k+1|k} = F\left(\boldsymbol{\chi}_{i,k}, \mathbf{u}_k\right), \tag{6.14}$$

$$\mathbf{P}_{k+1}^{XX} = \sum_{i=0}^{2n_s} \omega_i^c \left[\bar{\boldsymbol{\chi}}_{i,k+1|k} - \sum_{i=0}^{2n_s} \omega_i^m \bar{\boldsymbol{\chi}}_{i,k+1|k}\right]\left[\bar{\boldsymbol{\chi}}_{i,k+1|k} - \sum_{i=0}^{2n_s} \omega_i^m \bar{\boldsymbol{\chi}}_{i,k+1|k}\right]^T + \mathbf{Q}_k, \tag{6.15}$$

$$\boldsymbol{\Psi}_{i,k+1|k} = H\left(\bar{\boldsymbol{\chi}}_{i,k+1|k}, \mathbf{u}_k\right), \tag{6.16}$$

$$\mathbf{P}_{k+1}^{YY}=\sum_{i=0}^{2n_s}\omega_i^c\left[\boldsymbol{\Psi}_{i,k+1|k}-\sum_{i=0}^{2n_s}\omega_i^m\boldsymbol{\Psi}_{i,k+1|k}\right]\left[\boldsymbol{\Psi}_{i,k+1|k}-\sum_{i=0}^{2n_s}\omega_i^m\boldsymbol{\Psi}_{i,k+1|k}\right]^T+\mathbf{R}_k, \tag{6.17}$$

$$\mathbf{P}_{k+1}^{XY}=\sum_{i=0}^{2n_s}\omega_i^c\left[\bar{\boldsymbol{\chi}}_{i,k+1|k}-\sum_{i=0}^{2n_s}\omega_i^m\bar{\boldsymbol{\chi}}_{i,k+1|k}\right]\left[\boldsymbol{\Psi}_{i,k+1|k}-\sum_{i=0}^{2n_s}\omega_i^m\boldsymbol{\Psi}_{i,k+1|k}\right]^T, \tag{6.18}$$

$$\mathbf{K}_{k+1}=\mathbf{P}_{k+1}^{XY}\left(\mathbf{P}_{k+1}^{YY}\right)^{-1}, \tag{6.19}$$

$$\mathbf{X}_{k+1}=\hat{\mathbf{X}}_{k+1}^{-}+\mathbf{K}_{k+1}\left(\boldsymbol{\delta}(k+1)-\sum_{i=0}^{2n_s}\omega_i^m\boldsymbol{\Psi}_{i,k+1|k}\right), \tag{6.20}$$

$$\mathbf{P}_{k+1}=\mathbf{P}_{k+1}^{XX}-\mathbf{K}_{k+1}\mathbf{P}_{k+1}^{YY}\mathbf{K}_{k+1}^{T}. \tag{6.21}$$

The term $\boldsymbol{\delta}(k+1)$ in Eq. (6.20) refers to the real output of the system, which would be the extracted free vibration of the system. $\mathbf{P}_{k+1}$ and $\mathbf{X}_{k+1}$ are the estimated covariance matrix and desired state vector, respectively. They would be used in the next iteration to calculate the new sigma points.

The bridge pier is excited by the river water and other external excitations, such as traffic, pedestrians crossing the bridge, and wind. In the Kalman filtering approach, we need to define a process error for the system, compensating for the mathematical model's uncertainty and other assumptions involved in the estimation process. For this specific problem, it is almost impossible to measure the external excitations of the bridge pier. To deal with this issue, we introduced the RD, which extracts the free vibration response of the vibrating system. This means the reference measured data aimed for in the UKF would be independent of the excitation—whatever it is [96].

6.3. **Case studies**

In the previous sections, Euler beam theory was employed to determine a general dynamic equation of a bridge pier. This model could be adapted for any bridge pier with any boundary condition and different external excitations, water levels, and soil height around the pier. After this, the UKF and the RD method were introduced briefly. In this section, we simulate a bridge pier vibration using MATLAB [132] software and use the output vibration response for scour quantification. We also implement our proposed approach on a real bridge pier located in Morris city of Manitoba province, Canada. The detail on each of these studies is presented in the following subsections.

6.3.1. Numerical simulations

In this section, the mathematical model of a virtual bridge pier, Eq. (6.6), is used for simulation studies via MATLAB software. We consider a concrete pier with a rectangular cross-sectional area and a length (L) equal to 20 m, cross-sectional area, $A = 13 \times 1.7\ m^2$, and modulus of elasticity equal to $E = 3 \times 10^{10}\ Pa$ with a density of $3000\ kg/m^3$. Soil stiffness and damping values are $k_s = 8 \times 10^8\ N/m$ and $c_s = 18 \times 10^6\ N/m.s$, respectively. The soil height is assumed to equal 5 m, and the water level is assumed to be 5 m from the top of the soil. $M_D = 42 \times 10^3\ kg$ and $P = M_D\, g$, and $g = 9.81 m/s^2$. We use a rocker bearing, and the stiffness and damping of the bearing is set to $k_b = 56 \times 10^6\ N/m$ and $c_s = 2.4 \times 10^4\ N/m.s$, respectively [133].

The first three vibrational mode functions of the Euler beam are considered for analysis. We apply a combination of a triangle impulse force with a 0.5 s width, a random vibration with an amplitude of 0.02, and an El-Centro earthquake time history (dividing the total signal amplitude by 10) as ambient vibration, all of which are external excitations applied to the bridge (Figure. 6-4 (a)). We assume a fixed-free boundary condition for the beam with mode shape function $X_N(x) = \sqrt{\frac{1}{L}}\left[(\sin \beta_N x - \sinh \beta_N x) - \alpha_N(\cos \beta_N x - \cosh \beta_N x)\right]$, which

$\alpha_N = \frac{\sin\beta_N L + \sinh\beta_N L}{\cos\beta_N L + \cosh\beta_N L}$, and N is a mode number. $\beta_N L$ is equal to 1.87, 4.65, 7.85, and 10.99 for the first four modes [126].

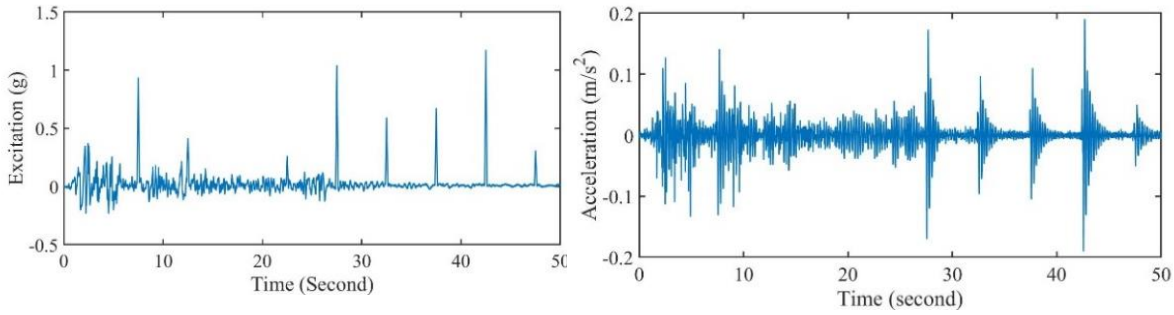

(a) (b)

Figure. 6-4: a) The excitation applied to the simulating structure; b) the total acceleration vibration response of the structure

We define the desired states and transfer Eq. (6.6) to the state-space form. We conduct some case studies to predict soil stiffness directly and predict the height of the soil too; then, we choose to predict the soil parameters as desired states, which is more convenient for quantifying the scour level. We assume that no damage exists on the bridge pier itself. The desired state vector consists of:

$$\mathbf{X} = \{x_1 \quad x_2 \quad x_3 \quad \dot{x}_1 \quad \dot{x}_2 \quad \dot{x}_3 \quad k_s \quad c_s\}^T = \{x_1 \quad x_2 \quad x_3 \quad x_4 \quad x_5 \quad x_6 \quad x_7 \quad x_8\}^T. \tag{6.22}$$

Due to the nature of our proposed output-only scour quantification method, we just need to extract the free vibration response of the bridge pier from its ambient vibration, as shown in Figure. 6-5(a). The RD is applied to the measured response in Figure. 6-4(b), with trigger point $1.9\sqrt{\text{var}(\ddot{\mathbf{x}})}$ and 3000 (six seconds) samples for each segment. The sampling rate is 500 Hz. Based on this trigger point, the algorithm picks about 420 segments for averaging. Based on these tuning parameters for the RD, the first five seconds of the free vibration response and its corresponding fast Fourier response (FFT) are shown in Figure. 6-5(b) .

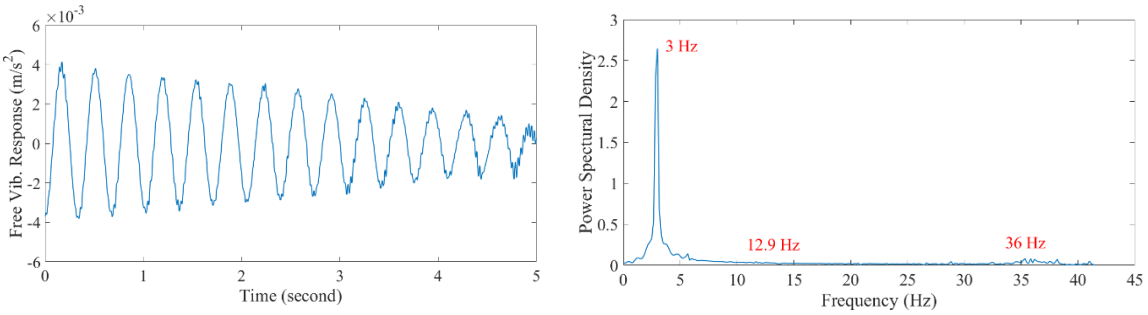

(a) (b)

Figure. 6-5: a) The free vibration response of the system; b) The FFT of the free vibration response

The free vibration response reduces the uncertainty of the mathematical model due to unknown excitations. Considering Eq. (6.6), desired state vector Eq. (6.22), and the free vibration response, the discrete domain state space transition and measurement functions of the model are expressed as:

$$\mathbf{X}_{k+1|k} = \begin{bmatrix} x_1 + \Delta t\, x_4, \\ x_2 + \Delta t\, x_5, \\ x_3 + \Delta t\, x_6, \\ x_4 + \frac{\Delta t}{M_{11}}[-(x_8 D_{11} + \tilde{C}_{11})x_4 - (x_8 D_{12} + \tilde{C}_{12})x_5 - (x_8 D_{13} + \tilde{C}_{13})x_6 \\ \quad - (\tilde{K}_{11} + D_{11}x_7)x_1 - (\tilde{K}_{12} + D_{12}x_7)x_2 - (\tilde{K}_{13} + D_{13}x_7)x_3], \\ x_5 + \frac{\Delta t}{M_{22}}[-(x_8 D_{21} + \tilde{C}_{21})x_4 - (x_8 D_{22} + \tilde{C}_{22})x_5 - (x_8 D_{23} + \tilde{C}_{23})x_6 \\ \quad - (\tilde{K}_{21} + D_{21}x_7)x_1 - (\tilde{K}_{22} + D_{22}x_7)x_2 - (\tilde{K}_{23} + D_{23}x_7)x_3], \\ x_6 + \frac{\Delta t}{M_{33}}[-(x_8 D_{31} + \tilde{C}_{31})x_4 - (x_8 D_{32} + \tilde{C}_{32})x_5 - (x_8 D_{33} + \tilde{C}_{33})x_6 \\ \quad - (\tilde{K}_{31} + D_{31}x_7)x_1 - (\tilde{K}_{32} + D_{32}x_7)x_2 - (\tilde{K}_{33} + D_{33}x_7)x_3], \\ x_7, \\ x_8 \end{bmatrix} \tag{6.23}$$

$$= F(\mathbf{X}_k, \Delta t),$$

$$\mathbf{Y}_k = \begin{bmatrix} \frac{1}{M_{11}}[-(x_8 D_{11} + \tilde{C}_{11})x_4 - (x_8 D_{12} + \tilde{C}_{12})x_5 - (x_8 D_{13} + \tilde{C}_{13})x_6 \\ -(\tilde{K}_{11} + D_{11}x_7)x_1 - (\tilde{K}_{12} + D_{12}x_7)x_2 - (\tilde{K}_{13} + D_{13}x_7)x_3], \\ \frac{1}{M_{22}}[-(x_8 D_{21} + \tilde{C}_{21})x_4 - (x_8 D_{22} + \tilde{C}_{22})x_5 - (x_8 D_{23} + \tilde{C}_{23})x_6 \\ -(\tilde{K}_{21} + D_{21}x_7)x_1 - (\tilde{K}_{22} + D_{22}x_7)x_2 - (\tilde{K}_{23} + D_{23}x_7)x_3], \\ \frac{1}{M_{33}}[-(x_8 D_{31} + \tilde{C}_{31})x_4 - (x_8 D_{32} + \tilde{C}_{32})x_5 - (x_8 D_{33} + \tilde{C}_{33})x_6 \\ -(\tilde{K}_{31} + D_{31}x_7)x_1 - (\tilde{K}_{32} + D_{32}x_7)x_2 - (\tilde{K}_{33} + D_{33}x_7)x_3] \end{bmatrix} \quad (6.24)$$

$$= H(\mathbf{X}_{k+1|k}, \Delta t).$$

where $\tilde{C}_{mn} = c_b X^2{}_m(x = L)$, and $\tilde{K}_{mn} = EI V_{mn} + PQ_{mn} + k_b X^2{}_m(x = L)$. Using these state-space equations, the stiffness and damping of the soil around the pier are estimated using the RD-UKF technique. The soil stiffness and damping values for the constant soil profile are estimated in Figure. 6-6.

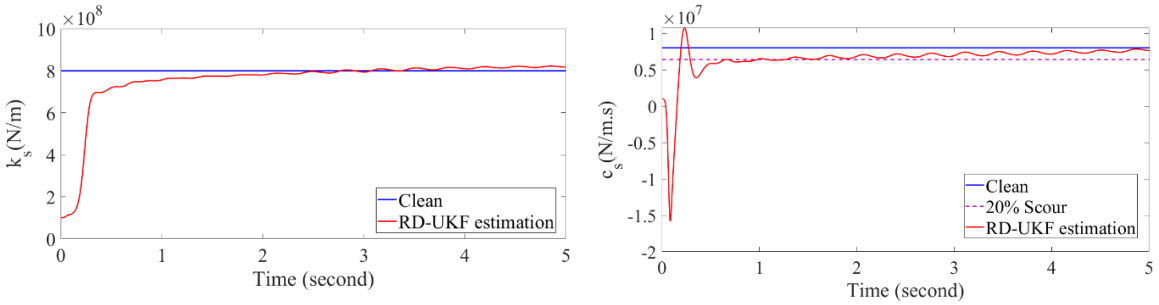

(a) (b)

Figure. 6-6: a) The estimated stiffness and b) damping value of the soil

The initial information for displacement and velocity is assumed to be zero, $\mathbf{x} = \dot{\mathbf{x}} = 0$, for the stiffness value $x_{7,int.} = 1\times10^8$ N/m, and for the damping value $x_{8,int.} = 1\times10^6$ N.s/m. Also, the initial error covariance matrix is defined as $\mathrm{diag}[\mathbf{P}_x \ \ \mathbf{P}_x \ \ \mathbf{P}_k \ \ \mathbf{P}_c]$, where $\mathbf{P}_x = \mathbf{P}_{\dot{x}} = \mathrm{ones}(3,1)$, $\mathbf{P}_k = 10^{12.5}$, and $\mathbf{P}_c = 10^{12}$. The UKF tuning parameters is set as $\lambda = 1$. The process and measurement noise covariance matrices are $10^{-20} \times I_8$, and $10^{-5} \times I_8$, sequentially. To show the technique's ability to quantify scour, we assumed a 20 percent scour in the model and used the previously tuned RD-UKF algorithm for scour quantification without any

change in the tuning parameters of the algorithm. The technique quantifies the scour within an acceptable range, as shown in Figure. 6-7.

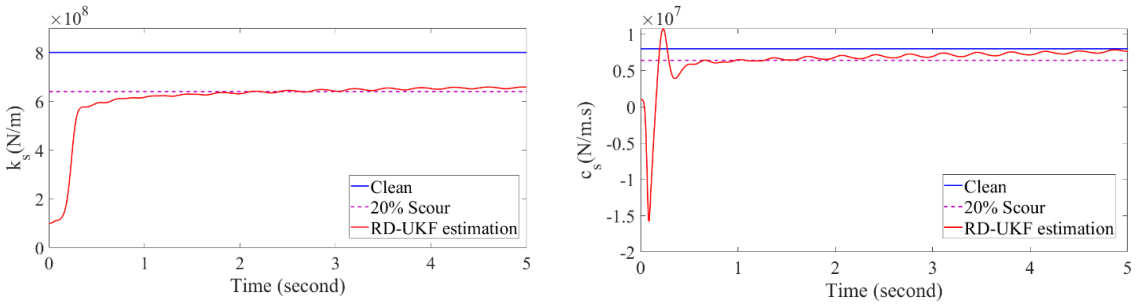

(a) (b)

Figure. 6-7: The estimated a) stiffness and b) damping value of the soil with constant profile affected by scour

Based on the results from Figure. 6-6 to Figure. 6-7, the proposed approach showed good performance in estimating the stiffness and damping of the soil around the pier, with acceptable accuracy for both non-scour and scour scenarios. Even though the soil stiffness was estimated accurately, the damping value has been slightly overestimated, as shown in Figure. 6-7. It should be noted that this poor estimation of damping estimation has been seen before [96].

We could estimate the soil stiffness around the pier accurately; however, to estimate the soil height around the pier, we need to define a soil profile as a function of the soil height. Eq (6.25) represents the lateral soil response around the pier (soil reaction, p, lateral displacement curve, ω). Details on the equation and constant values are available in the American Petroleum Institute (API) design code [134].

$$p = \Lambda p_u \tanh\left(\frac{kx}{Ap_u}\omega\right), \tag{6.25}$$

where p_u is the ultimate resistance of the soil at depth x. The detail information about Λ, and $k\,(kN.m^{-3})$-constant values related to the soil specification- are available in the API standard. The first derivative of the soil reaction equation is approximately equal to the soil

stiffness because the amplitude of the lateral displacement of the soil around the pier is small and remains in the linear region [135].

$$\bar{k}_s = \frac{dp}{d\omega}\Big|_{\omega=0} = \Lambda p_u \frac{\frac{kx}{\Lambda p_u}}{\cosh^2(\frac{kx\omega}{\Lambda p_u})}\Big|_{\omega=0} = kx, \tag{6.26}$$

where $\bar{k}_s$ in Eq. (6.26) has a unit of $kN.m^{-2}$ [135]; then, by multiplying it by the soil height, it will have the stiffness unit. Considering this simplification, we define different soil profiles around the pier to evaluate the proposed method's ability to estimate the soil height under linear, quadratic, and cubic profiles.

The initial values of and details on the state estimation process are mentioned in Table 6-1 for the three profiles for the sake of reproducibility for future users. As we are going to estimate the soil height using different profiles, $h_s = x_7$ will be defined as the soil height, and we will have only seven states in each case.

$$\mathbf{X} = \{x_1 \quad x_2 \quad x_3 \quad \dot{x}_1 \quad \dot{x}_2 \quad \dot{x}_3 \quad h_s\} = \{x_1 \quad x_2 \quad x_3 \quad x_4 \quad x_5 \quad x_6 \quad x_7\}. \tag{6.27}$$

Then, Eq. (6.23) and Eq. (6.24) are rearranged as follows in Appendix E. $f_{k_s}(x_7)$ and $f_{c_s}(x_7)$ define the soil stiffness and damping functions as dependent on the soil height. Their different forms based on soil profiles are given in Table 6-1.

Table 6-1: Initial and tuning parameters for different soil profiles

Soil profile	Equation	$\mathbf{m}_0$	$\mathbf{P}_0$	$\mathbf{Q}$	$\mathbf{R}$
Linear	$f_{k_s}(x_7) \rightarrow 1.6\times10^{8} x_7$ $f_{c_s}(x_7) \rightarrow 1.6\times10^{6} x_7$	$\mathbf{x} = \dot{\mathbf{x}} = 0$ $x_{7,int.} = 0$ m	$\mathbf{P}_x = \mathbf{P}_{\dot{x}} = 10^{0}$ $\mathbf{P}_{x_7} = 10^{0.5}$	$10^{-9.16}\times\mathbf{I}_{7\times7}$	$10^{-2}\times\mathbf{I}_{3\times3}$
Quadratic	$f_{k_s}(x_7) \rightarrow 3.2\times10^{7} x_7^2$ $f_{c_s}(x_7) \rightarrow 3.2\times10^{5} x_7^2$	$\mathbf{x} = \dot{\mathbf{x}} = 0$ $x_{7,int.} = 0$ m	$\mathbf{P}_x = \mathbf{P}_{\dot{x}} = 10^{0}$ $\mathbf{P}_{x_7} = 10^{0.6}$	$10^{-9.34}\times\mathbf{I}_{7\times7}$	$10^{-5}\times\mathbf{I}_{3\times3}$

Cubic	$f_{k_s}(x_7) \rightarrow 6.4\times10^6 x_7^3$ $f_{c_s}(x_7) \rightarrow 6.4\times10^4 x_7^2$	$\mathbf{x} = \dot{\mathbf{x}} = 0$ $x_{7,\text{int.}} = 0$ m	$\mathbf{P}_x = \mathbf{P}_{\dot{x}} = 10^0$ $\mathbf{P}_{x_7} = 10^{0.849}$	$10^{-11}\times\mathbf{I}_{7\times7}$	$10^{-15}\times\mathbf{I}_{3\times3}$

The estimated soil height is shown in Figure. 6-8(a).

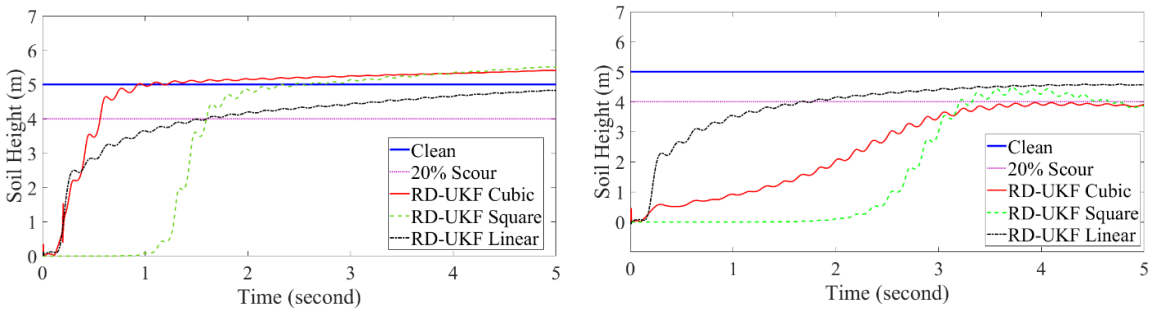

(a) no-scour (b) one-meter scour

Figure. 6-8: Results of soil height estimations:

To show the technique's ability to quantify scour, we applied a one-meter scour to the model and used the previously tuned RD-UKF algorithm for scour quantification without any change in the tuning parameters of the algorithm. The technique could quantify the scour within an acceptable range. Based on Figure. 6-8(b), the accuracy of the scour quantification improves with the increase in the order of the stiffness function.

To compare the data-driven approach to this proposed method, we have illustrated the FRF of the model under scour in Figure. 6-9. The first natural frequency of the pier has changed from 3 Hz to 2.83 Hz. When 20 percent of scour was assumed for the soil around the pier, the natural frequency decreased by about seven percent. This means that the natural frequency-based scour monitoring technique is not reliable in scour quantification. Data-based approach can only detect the existence of scour [112]. This is one of the advantages of the proposed method over other data-based approaches.

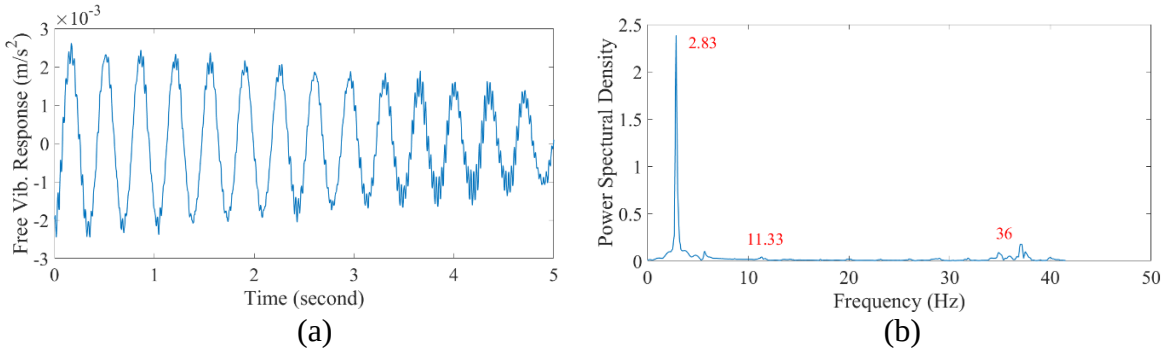

Figure. 6-9: a) The free vibration response under scour; b) The FFT of the free vibration response of the system under scour

This section has shown the capabilities of the proposed method for scour quantification in a simulation study. In the next section, the proposed method will be examined with a full-scale study.

6.3.2. A full-scale study of a bridge pier

In the previous section, we demonstrated the capability of the proposed method in scour quantification of a bridge pier in simulation studies. To investigate the performance of this method on an actual structure, an ambient vibration of a multi-span bridge under normal operation, located in Morris, Manitoba, Canada, was recorded over the duration of a year, starting in October 2019. This five-span continuous bridge system is about 300 meters long and is supported on ten piers.

Approximately 7,500 trucks travel across the bridge each month. We have installed a uniaxial accelerometer to Pier 5, to measure ambient vibration due to the river water beating the piers, crossing traffic, wind, and pedestrians. We selected Pier 5 because it is surrounded by water all year, and it is vulnerable to scour, as shown in Figure. 6-10. Images of the bridge and the installed sensor on the Pier 5 are shown in Figure. 6-11.

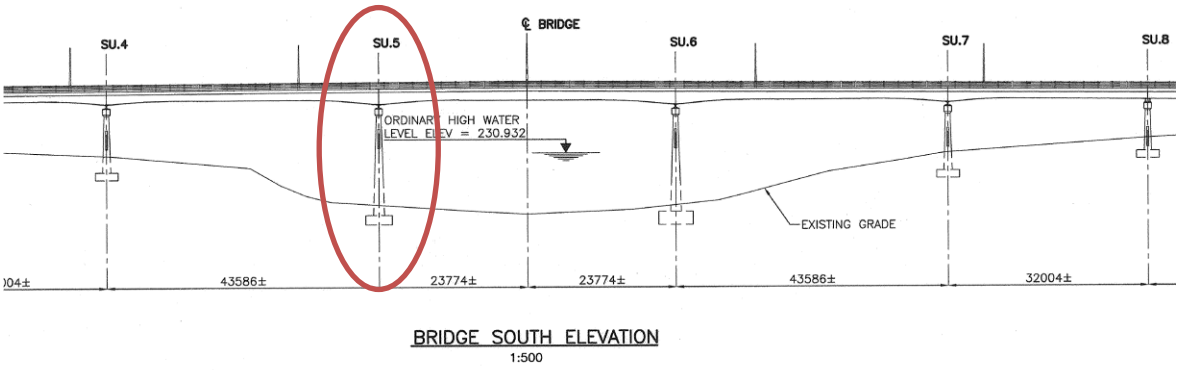

Figure. 6-10: Side view of the large-scale bridge system drawing

(a) Pier 5 (b) close view of Pier 5 (c) installed sensor (d) data acqusition

Figure. 6-11: Views of the bridge and installed sensor and data acquisition system

A MEMS-Piezoresistive BDI model A1316 accelerometer with an amplitude range of ± 2 g, a frequency range (min) of 0–300 Hz, and a voltage sensitivity of 1000 mV/g is used. A four-channel wireless data acquisition system was used for data communication (BDI model, STS-PRIME-0337).

The river water always flows around Piers 5 and 6 of the bridge during a year, but the water level changes during flood seasons in early spring and fall. We recorded the ambient vibration of Pier 5 during four months, including February, July, August and October. The soil stiffness around the pier was estimated each time. The ambient vibrations of Pier 5 in February 2020 and August 2020, both measured around 3 pm, are shown in Figure. 6-12.

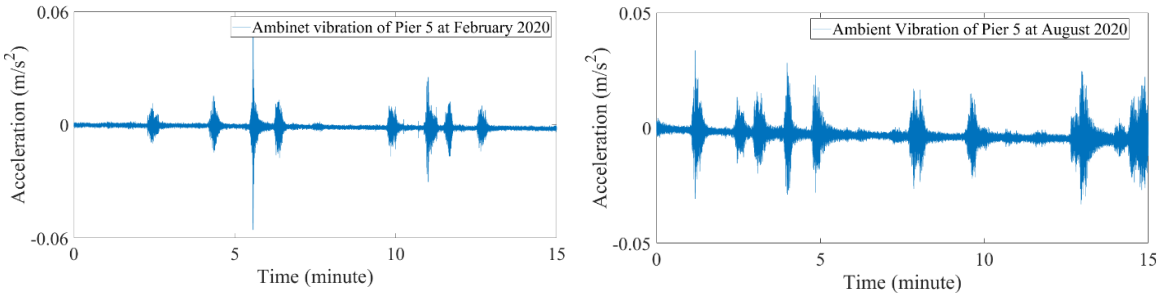

(a) February 2020 (b) August 2020

Figure. 6-12:Ambient vibrations of Pier 5

The sampling rate of the data acquisition system is 100 Hz, and the data is recorded for about 30 minutes each time. Considering that the bridge length is about 300 meters and the maximum speed limit on the bridge is $50\ \mathrm{km/h}$, it takes at least 21.6 seconds for a car to cross the bridge. This time is useful for selecting a reasonable length of segments for the random decrement to extract the free vibration of the pier using the recorded ambient vibration. For RD implementation, $0.01\sqrt{\mathrm{var}(\ddot{\mathbf{x}})}$ is selected as a trigger point, with a segment length equal to 30 seconds. Figure. 6-13 shows the first 20 seconds of the extracted free vibration of Pier 5 in February 2020 and August 2020.

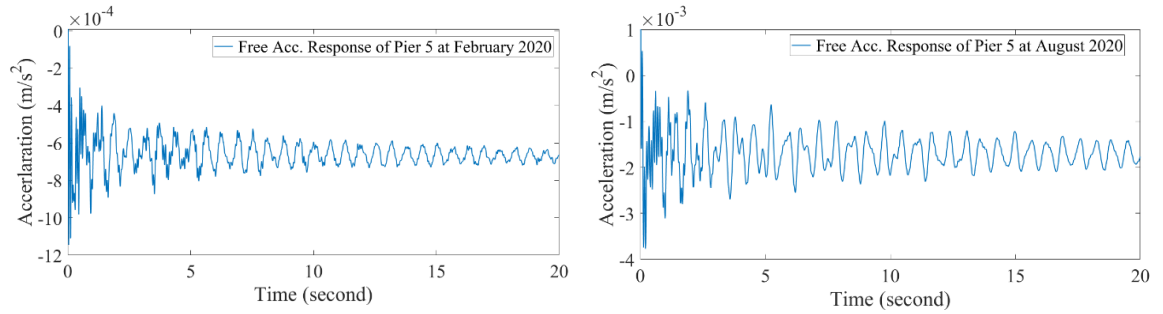

(a) February 2020 (b) August 2020

Figure. 6-13: Free vibration responses of Pier 5

Similar to the simulation study, the fixed-free boundary condition is considered for the modelling of the Euler beam, as shown in Figure. 6-3. Four rocker bearings are at the top of the pier, and they are connected to the girders, as shown in Figure. 6-14. The stiffness and coefficient of friction of this bearing are $\mathrm{k_b} = 14\times10^6\ \mathrm{N/m}$ and $\mu = 0.04$, respectively [133]. The equivalent damping corresponding to the $\mu = 0.04$ is calculated based on

$C_b = (4\mu N_p)/(\pi\omega_p X_p)$, where N_p is the normal force, ω_p is the fundamental natural frequency, and X_p is the maximum displacement [126]. As we have four bearings on the top of the Pier 5 and they are installed in parallel, the total stiffness and damping of the bearings is four times the stiffness and damping of each bearing.

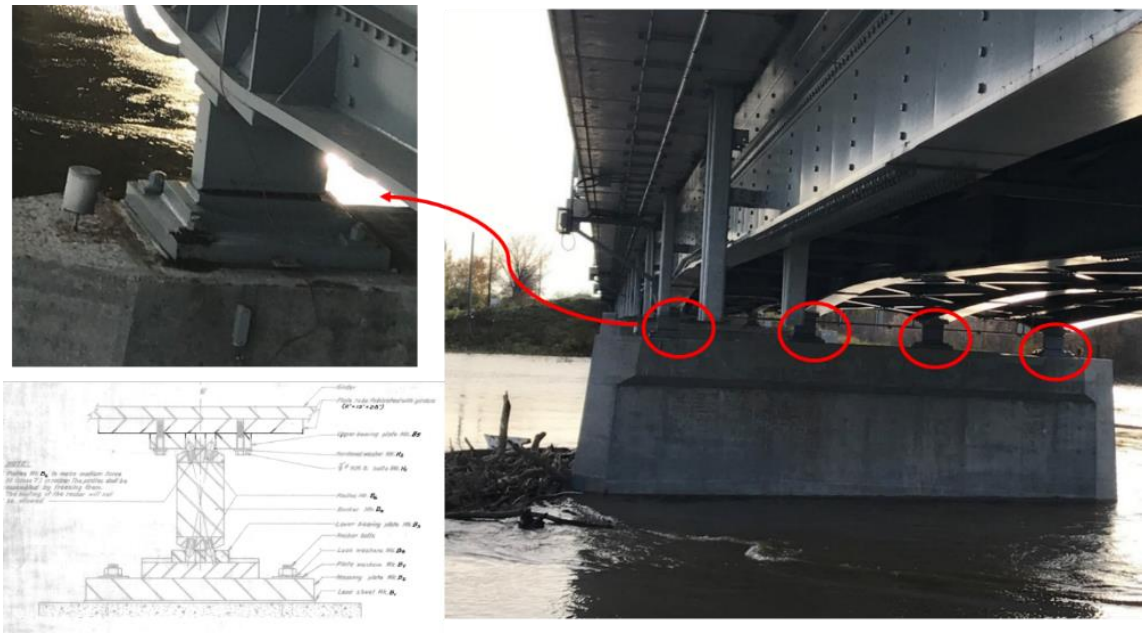

Figure. 6-14: The high type rocker bearing of Pier 5 and its detailed drawing

We consider Pier 5 as an Euler beam with a rectangular shape cross-section with a dimension of $A = 14 \times 1.5\ m^2$ and a length of 20 meters. The concrete modulus of elasticity is set to $E = 15 \times 10^9\ Pa$ with a density of $3000\ kg/m^3$. The initial soil stiffness and damping values and their corresponding covariance values for the UKF tuning are $k_s^0 = 1 \times 10^7\ N/m$, $c_s^0 = 1 \times 10^3\ N/m^2$, $\mathbf{P}_{k_s} = 10^{17}$, and $\mathbf{P}_{c_s} = 10^{15}$, respectively. Also, $10^{-10.8} \times \mathbf{I}_{8\times 8}$ for the covariance of process noise, with $10^{-3.2}$ for the covariance of measurement noise. The estimated stiffness value at each time of measurement is shown in Figure. 6-15. The equivalent stiffness of the sediments around Pier 5 is estimated using the mathematical model developed in Section 6.2.2 and Pier 5's geometrical specification.

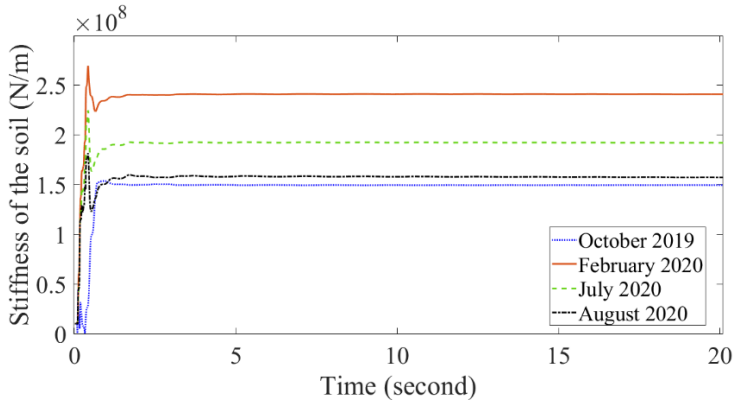

Figure. 6-15: Estimated soil stiffness around the bridge pier in different months

Figure. 6-15 demonstrates the estimated stiffness value around $k_s = 1.5 - 2.3 \times 10^8$ N/m for all the seasons. The difference between February and the other months should be addressed because of the thick ice around the pier during wintertime. The ice thickness can be about 60 cm and increases the stiffness of the pier [136]. Gonzales and his coworkers [137] have shown that the natural frequency of structures increases by up to 35% during winter. Similar behaviour was observed in the bridge considered in this study.

The simulation study results in section 6.3.1 show that the soil stiffness behaviour leads to a more accurate estimation of the soil height around the pier using a cubic function rather than the two other functions. Therefore, the soil height will only be estimated using the cubic function. The initial soil height is assumed to be zero, with $\mathbf{P}_{h_s} = 10^{0.8195}$, and $10^{-18.6} \times \mathbf{I}_{7\times7}$ for the covariance of process noise, and $10^{-10.3}$ for the covariance of measurement noise. The estimated soil height for each month is shown in Figure. 6-16. The estimated soil height is between 4-5 meters. To estimate the soil height, the average stiffness estimated for each month in Figure. 6-15 was used.

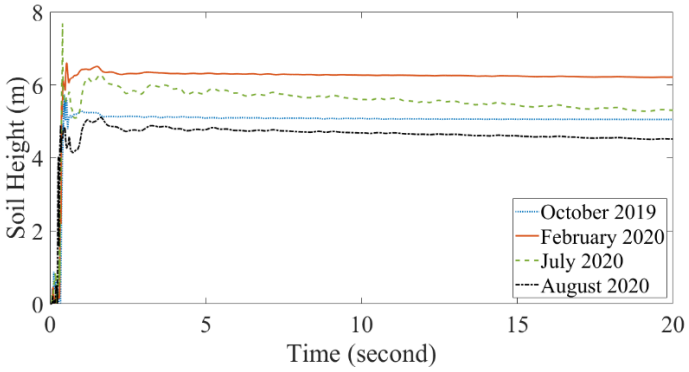

Figure. 6-16: Estimated soil height around the bridge pier in different months

In order to verify the estimated soil height in Figure. 6-16, we excavated the river ice in February 2020 and measured the height of the sediment around the pier based on the Canadian Geodetic Vertical Datum of 2013 (CGVD2013) [138]. We measured the water height and water level using a surveying rod equipment shown in Figure. 6-17(a). The pier footing elevation is available from the bridge drawings. The soil height around the pier was extracted, as shown in Figure. 6-17(b). The thick ice in February caused the difference between the estimated soil height and the measured height. The model does not consider the temperature effect. However, as we assumed all other components have fixed stiffness values, the RD-UKF intelligently increases the soil stiffness (height) to compensate for this difference.

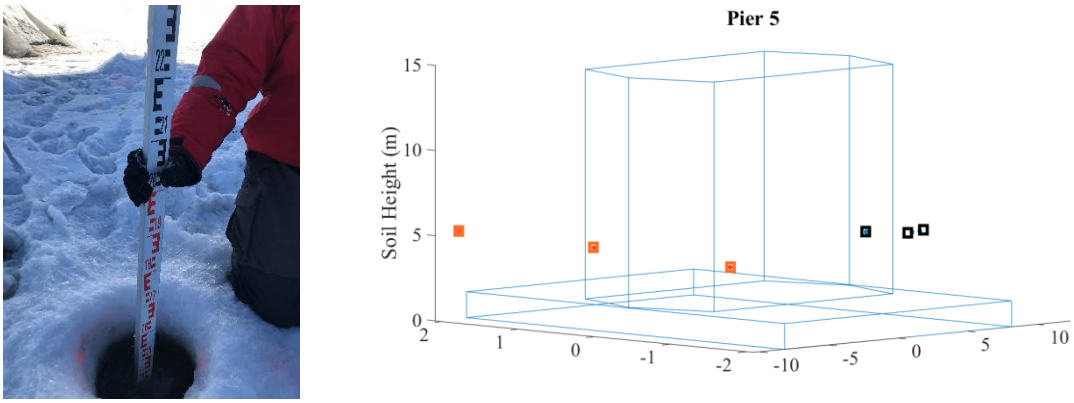

(a) (b)

Figure. 6-17: a) The survey used for the soil height around the Pier 5; b) and schematic of the height of the soil around the Pier 5

In Figure. 6-17(b), the orange colored points denote the height downstream, and the black points denote the height upstream. The estimated soil height is almost in agreement with Figure 18; both show that the soil height is between 4-5 meters, with an average of 4.7 meters. This height can be used for future analysis to create an initial estimate for the sediment profile. In addition to the February measurement, for further confirmation, we verified our estimated soil height in August 2020 as well. A highly accurate Acoustic Doppler Profiler (ADP) system measured the river soil height around the pier, as shown in Figure. 6-18. Based on the second field measurement, the soil height around the pier was between 4-5 meters, with an average of 4.67 meters. Then, the RD-UKF algorithm estimated the soil height around the pier accurately in summer and fall, but not in winter.

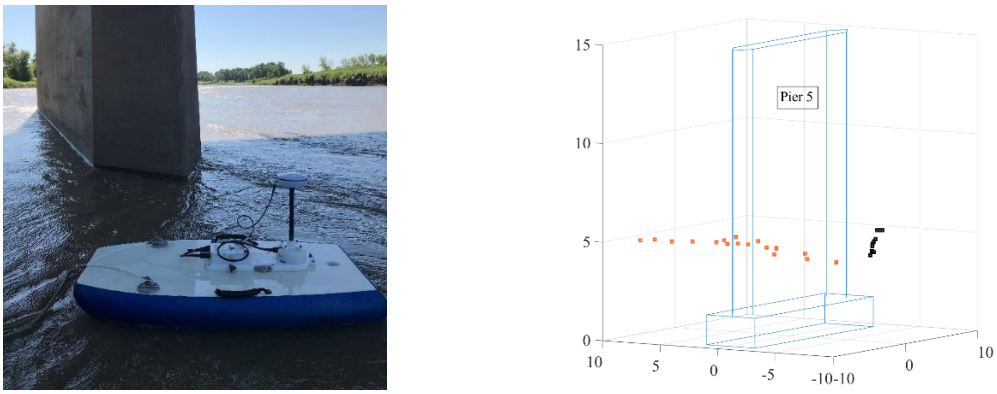

Figure. 6-18: An Acoustic Doppler Profiler (ADP) boat and measured soil height around the Pier 5 in August 2020

In addition to model-based scour quantification, we have shown the FFT of the extracted free vibration response for the four months considered in this study in Figure. 6-19. The model natural frequencies are calculated to compare the accuracy of the pier model's estimated stiffness matrix with the ground truth. Since we have considered the first three modes of the pier model, the first three natural frequencies of the pier's Euler model are 2 Hz, 5.3 Hz, and 11 Hz, respectively. The first extracted natural frequencies are close to the first natural frequency based on Figure. 6-19. The second and third natural frequencies are very close to the other frequencies in Figure. 6-19. There is another peak that can be observed at 11.4 Hz in all the months as well. However, in February, another peak is observed at about 6 Hz, which is not observed in other months. In addition, the peaks around 11.4 Hz increased to about 12.3 Hz in February. In February, the river was frozen, and the ice thickness was about 60 cm. The entire system's stiffness matrix would be affected by this phenomenon and cold temperatures, which could be the reason for the additional 6 Hz peak [137]. Based on Figure. 6-15, the stiffness has increased by about 30 percent in February, while the natural frequency (11.4 Hz) of the pier increased by about 10 percent (12.3 Hz) at the same time.

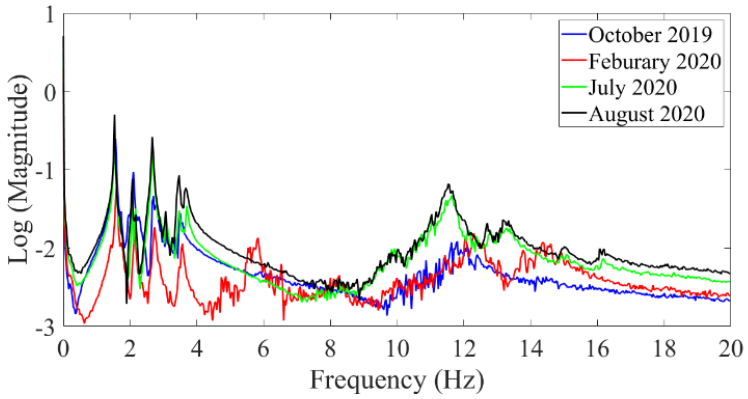

Figure. 6-19:FFT of the free responses of the Pier 5 in different months

Compared to the FFT analysis as a data-driven approach, the proposed method requires complicated mathematical equations featuring extensive trial-and-error solutions to identify the best set of tuning parameters and the initial information for the UKF. However, the proposed model-based method could predict the levels of scour accurately. On the other hand, using the FFT analysis, it is not an easy task to find the dominant peak caused by the soil effect to track its change for scour monitoring as shown in Figure. 6-19. For example, it cannot be recognized which of the peaks between 1.5–4 Hz will be affected by scour; scour could affect all of these peaks. Moreover, we cannot define a clear relationship between the rate of change in the natural frequency and the soil stiffness because of scour. Therefore, this model-based method could be beneficial to overcome the limitations in the traditional data-driven methods.

6.4. **Conclusion**

The scour phenomenon around bridge piers and foundation systems is one of the most critical problems threatening the safety of bridge systems. The physics model-based approach using vibration measurement for estimating the level of the scour are currently nonexistent. Therefore, in this paper, a new scour quantification method was proposed. The technical contributions of this paper include the following:

1. A new output-only physics model-based scour level quantification method was proposed.
2. The proposed method was integrated with the UKF, RD, and continuous pier model.
3. The new continuous Euler pier model was developed to account for loads due to traffic, water flow, wind, and sediments around the pier as external loadings.
4. Any kind of vibration sources can be used for acceleration responses.
5. The proposed method only requires one uniaxial acceleration response measurement.
6. The proposed method can predict the level of scour accurately.
7. The proposed approach was verified using comprehensive simulation and field study considering the linear and nonlinear behaviour of the soil around the pier.
8. The results were demonstrated by an independent bathymetric survey through actual measurement and an ADP system, and the results were well in agreement with actual measurements.

More accurate mathematical equations of the model will be done in our future study.

6.5. **Acknowledgement**

The authors would like to acknowledge Manitoba Infrastructure Agency for their support during the field study and providing required instruments. Evangeline Murison for letting us to have the bridge drawing and other related data. Alexander Wall for his cooperation in the measuring of the riverbed height using survey rod and ADP system, and Geoffrey Gao for his help to attach the accelerometer to the pier. We would like to acknowledge the KGS group for letting us to use their Ansys software to implement modal analysis on the whole bridge.

Chapter Seven:

Conclusions and Future Work

This chapter reviews the conclusions of this dissertation and proposes potential avenues for future research associated with each contribution of the dissertation. The conclusions are divided into three sections based on the research contribution introduced in the first chapter and briefly discuss their advantages and limitations in order to offer up some ideas for future work.

7.1. **Conclusions**

The main goal of this thesis was to improve Kalman filtering performance in terms of estimating the unknown parameters of a high-dimensional system under unknown excitations. The uncertainties associated with the system identification process is reducing by increasing the number of sigma points or eliminating the indeterministic inputs. The skeleton of the work in Chapters 3 through 6 their advantages and drawbacks.

Iterated cubature unscented Kalman filter[1]: The IMUKF filter was developed to improve the filtering performance of the UKF for the identification of a system with a large number of states. The results showed that IMUKF and pure UKF or CKF offer similar results for a 3 DoF model. However, the newly proposed IMUKF outperformed the pure UKF and CKF in terms of estimating the stiffness values for the 10-DoF system with high noise levels.

- *Findings*:

    1. The method does not have a complicated mathematical equation and follows the original UKF steps as opposed to other research studies introduced for the same purpose which does not.

    2. The performance of the method showed improvement as compared to pure UKF for nonlinear systems with a large number of states.

    3. It is more robust to noisy data rather than the original UKF because of the additional iteration added to the algorithm.

- *Drawbacks*:

1 **E. Ghorbani,** and Y. J. Cha, "*Iterated cubature unscented Kalman filter for large-DoF systems identification with noisy data*", Journal of Sound and Vibration, 420, 21-34, (2018).

1. Although the method does not have complicated mathematical equations, converging a clean response is time-consuming. There is a trade-off between the convergence time and the convergence rate.

2. Although the IMUKF performs better than pure UKF for damping estimation, there are still some discrepancies for some DoFs.

Output-only Kalman filtering[1]: The RD-UKF as an output-only method that is defined by the integration of a data-based method and a model-based method in order to quantify the level of damage in a structure. The method is categorized as a hybrid method and could be an avenue to combine other methods in these two fields to introduce more hybrid methods. The method has been verified with several numerical models and its superior performance has been shown. The RD-UKF successfully estimated the stiffness matrix and mass matrix of a full-scale seven-story building under different damage scenarios.

- *Findings*:

1. The RD-UKF method can reach the third step of the damage identification process (damage quantification) while data-driven methods can hardly localize the damage.

2. The proposed method estimates high-dimensional state vectors accurately by reducing the overall order of the state-space equation through the removal of input excitation states.

3. The RD-UKF eliminates the input excitation from the measured response and does not require estimating or reconstructing them.

1 **E. Ghorbani,** O. Buyukozturk, and Y. J. Cha, "*Hybrid output-only structural system identification using random decrement and Kalman filter*", Mechanical Systems and Signal Processing, 144 (2020): 106977. (Ph.D. degree).

4. The method reduces the complexities and uncertainties of the numerical model induced by eliminating the input excitation parameters as it improves the observability rank of the system.

5. RD-UKF is viable for a variety of structures subjected to different types of excitations such as random noises, periodic excitations, and earthquake excitations, or any combination thereof.

6. The RD-UKF is robust to the uncertainty in the mass matrix of the underlying structures and missing information (missing sensors) during measurement.

7. The proposed method was validated for an actual large-scale structure by comparing its results against those of existing methods. The results confirmed that RD-UKF method is capable of damage quantification in different real structural systems.

- *Drawback*:

1. The performance of the RD method decreases as the order of nonlinearity in the structure increases. The RD method must be specialized for specific nonlinear systems; there is no general algorithm of RD for nonlinear systems.

2. RD is not a real-time method; it needs the whole response to extract the free vibration response.

Output-only Kalman filtering for scour quantification[1]: The mathematical model developed in this thesis accurately considers all the external parameters affecting scour level around a bridge pier. The method can estimate the soil stiffness around the pier and the corresponding

1 **E. Ghorbani**, D. Svecova, D. J. Thomson and Y. J. Cha,, "*Bridge pier scour level quantification based on output-only Kalman filtering*", Journal Structural Health Monitoring, (under review) (Ph.D. degree)

soil height based on a defined soil profile. The estimated soil height was also in good agreement with the independent bathymetry conducted around the pier.

- *Findings*:

    1. The novel output-only physics model-based method is capable of scour level quantification.

    2. The use of Euler beam theory to account for loads due to traffic, water flow, wind, and sediments around the pier as external loadings was proved to be sufficient and reduced the complexity of the problem.

    3. The structural response from only one uniaxial accelerometer attached at the top of the pier provided sufficient input for determining the height of the soil at the pier.

    4. The proposed method can accurately estimate the scour level.

    5. The proposed approach estimated the soil height around the pier in both the simulation and field study considering the linear and nonlinear behaviour of the soil around the pier.

    6. The results were verified by actual measurement in an independent bathymetric survey and an ADP system and the results were well in agreement with actual measurements.

- *Drawback*:

    1. The mathematical model was developed based on a beam with a uniform cross-sectional area.

    2. The temperature effect was not considered in the model.

7.2. Future work

Several paths have been identified for potential future research based on the results presented here.

1. This study has assumed that the measured data, process noise, and measurement noise follow a Gaussian distribution. Developing the introduced methods for non-Gaussian data would be an exciting topic of research. Also, comparing the estimated parameters using both Gaussian and non-Gaussian data under different sampling rates would reveal the capabilities of the currently introduced method for the identification of non-Gaussian data.

2. Developing the RD for nonlinear systems would be an exciting topic of research. Comparison of the results of the specialized RD and the general RD will indicate the ways in which different levels of nonlinearities affect the estimation result.

3. Further investigation into the effect of different criteria on the trigger point of the RD could be additional revenue for future research.

4. Another potential avenue involves defining an Euler beam with various cross-sections along the beam length. This would take into account the effect of piles with different moduli of elasticity and areas.

5. An important issue not addressed in this study is the effect of thermal conditions on scour quantification results. As the site temperature changes from -30 Celsius in the wintertime to 25 Celsius in summer, the parameter associated with temperature could be considered in a future study. The soil height was estimated to be one meter higher than its actual height in February due to river ice thickness, and so considering this effect could address this wintertime issue.

References

1. U.S. Department of Transportation, F.H.A., *2015 Status of the Nation's Highways, Bridges and Transit: Conditions and Performance*. Janurary 2017.

2. ARTBA, *Bridge Report*. 2020, The American Road & Transportation Builders Association.

3. Cusson, D., Z. Lounis and L. Daigle, *Durability monitoring for improved service life predictions of concrete bridge decks in corrosive environments.* Computer-Aided Civil and Infrastructure Engineering, 2011. **26**(7): p. 524-541.

4. CSA-S6-19, *Canadian highway bridge design code*. 2019, Toronto : CSA International, 2019.

5. Farrar, C.R. and K. Worden, *An introduction to structural health monitoring.* Philosophical Transactions of the Royal Society A: Mathematical, Physical and Engineering Sciences, 2007. **365**(1851): p. 303-315.

6. Chang, P.C., A. Flatau and S. Liu, *Health monitoring of civil infrastructure.* Structural health monitoring, 2003. **2**(3): p. 257-267.

7. Moaveni, B., *System and damage identification of civil structures*. 2007, UC San Diego.

8. Au, S., *Operational Modal Analysis*. 2017, Singapore: Springer Nature.

9. Fu, Z.-F. and J. He, *Modal analysis*. 2001: Elsevier.

10. Vigsø, M., T. Kabel, M. Tarpø, R. Brincker and C. Georgakis. *Operational modal analysis and fluid-structure interaction*. in *28th International Conference on Noise and Vibration Engineering (ISMA 2018)*. 2018.

11. Voracek, D.F. and A.M. MOraleS, *Shaker Moving Mass on the Measured Modal Characteristics of.* 1988.

12. Teughels, A. and G. De Roeck, *Structural damage identification of the highway bridge Z24 by FE model updating.* Journal of Sound and Vibration, 2004. **278**(3): p. 589-610.

13. Ching, J., M. Muto and J.L. Beck, *Structural model updating and health monitoring with incomplete modal data using Gibbs sampler.* Computer-Aided Civil and Infrastructure Engineering, 2006. **21**(4): p. 242-257.

14. Hou, R., Y. Xia and X. Zhou, *Structural damage detection based on l1 regularization using natural frequencies and mode shapes.* Structural Control and Health Monitoring, 2018. **25**(3): p. e2107.

15. Balageas, D., C.-P. Fritzen and A. Güemes, *Structural health monitoring*. Vol. 90. 2010: John Wiley & Sons.

16. Yang, J.N., S. Lin, H. Huang and L. Zhou, *An adaptive extended Kalman filter for structural damage identification.* Structural Control and Health Monitoring: The Official Journal of the International Association for Structural Control and Monitoring and of the European Association for the Control of Structures, 2006. **13**(4): p. 849-867.

17. Yang, J.N., S. Pan and H. Huang, *An adaptive extended Kalman filter for structural damage identifications II: unknown inputs.* Structural Control and Health Monitoring, 2007. **14**(3): p. 497-521.

18. Bernal, D., *Kalman filter damage detection in the presence of changing process and measurement noise.* Mechanical Systems and Signal Processing, 2013. **39**(1-2): p. 361-371.

19. De Roeck, G., *Model–Based Methods of Damage Identification of Structures Under Seismic Excitation*, in *Seismic Structural Health Monitoring*. 2019, Springer. p. 237-259.

20. Richardson, E.V., S.R. Davis and P.F. Lagasse, *Comprehensive Scour Analysis at Highway Bridges HEC-18*, in *Scour and Erosion*. 2010. p. 1092-1101.

21. CBC-News. *Bonnybrook bridge failure 'unprecedented', TSB probe concludes*. December 17, 2014; Available from: https://tinyurl.com/y4cjmara.

22. Pritchard, J. *I-10 at washed out bridge in California to reopen Friday*. JULY 22, 2015; Available from: https://phys.org/news/2015-07-i-bridge-california-reopen-friday.html.

23. Wu, M. and A.W. Smyth, *Application of the unscented Kalman filter for real-time nonlinear structural system identification.* Structural Control and Health Monitoring, 2007. **14**(7): p. 971-990.

24. Kalman, R.E., *A New Approach to Linear Filtering and Prediction Problems.* Journal of Basic Engineering, 1960. **82**(1): p. 35-45.

25. Chatzi, E.N. and A.W. Smyth, *The unscented Kalman filter and particle filter methods for nonlinear structural system identification with non-collocated heterogeneous sensing.* Structural control and health monitoring, 2009. **16**(1): p. 99-123.

26. Julier, S., J. Uhlmann and H.F. Durrant-Whyte, *A new method for the nonlinear transformation of means and covariances in filters and estimators.* IEEE Transactions on Automatic Control, 2000. **45**(3): p. 477-482.

27. Julier, S.J. and J.K. Uhlmann. *New extension of the Kalman filter to nonlinear systems*. in *Signal processing, sensor fusion, and target recognition VI*. 1997. International Society for Optics and Photonics.

28. Julier, S.J. and J.K. Uhlmann, *Unscented filtering and nonlinear estimation.* Proceedings of the IEEE, 2004. **92**(3): p. 401-422.

29. Arasaratnam, I. and S. Haykin, *Cubature Kalman Filters.* IEEE Transactions on Automatic Control, 2009. **54**(6): p. 1254-1269.

30. Maes, K., A. Smyth, G. De Roeck and G. Lombaert, *Joint input-state estimation in structural dynamics.* Mechanical Systems and Signal Processing, 2016. **70**: p. 445-466.

31. Cole Jr, H.A., *Failure detection of a space shuttle wing flutter model by random decrement.* 1971.

32. Liu, G., Z. Mao and M. Todd, *Damage detection using transient trajectories in phase-space with extended random decrement technique under non-stationary excitations.* Smart Materials and Structures, 2016. **25**(11): p. 115014.

33. Vesterholm, K.K., R. Brincker and A. Brandt. *Detection of nonlinear behavior using the Random Decrement Technique*. in *8th International Operational Modal Analysis Conference, IOMAC 2019*. 2019. IOMAC.

34. Kalman, R.E. *A new approach to linear filtering and prediction problems" transaction of the asme~journal of basic*. 1960.

35. Chen, Z., *Bayesian filtering: From Kalman filters to particle filters, and beyond.* Statistics, 2003. **182**(1): p. 1-69.

36. Rauch, H.E., F. Tung and C.T. Striebel, *Maximum likelihood estimates of linear dynamic systems.* AIAA journal, 1965. **3**(8): p. 1445-1450.

37. Foun, K., *Identification of civil structural parameters using the extended Kalman filter*, in *Civil and Environmental Engineering*. 2010, Massachusetts Institute of Technology.

38. *Structural Identification by Extended Kalman Filter.* Journal of Engineering Mechanics, 1984. **110**(12).

39. Wu, M. and A.W. Smyth, *Application of the unscented Kalman filter for real-time nonlinear structural system identification.* Structural Control and Health Monitoring, 2007. **14**(7): p. 971-990.

40. Huang, Y., J.L. Beck and H. Li, *Bayesian system identification based on hierarchical sparse Bayesian learning and Gibbs sampling with application to structural damage assessment.* Computer Methods in Applied Mechanics and Engineering, 2017. **318**: p. 382-411.

41. Naveau, P., M.G. Genton and X. Shen, *A skewed Kalman filter.* Journal of multivariate Analysis, 2005. **94**(2): p. 382-400.

42. Rezaie, J. and J. Eidsvik, *A skewed unscented Kalman filter.* International Journal of Control, 2016. **89**(12): p. 2572-2583.

43. Kitagawa, G., *Monte Carlo Filter and Smoother for Non-Gaussian Nonlinear State Space Models.* Journal of Computational and Graphical Statistics, 1996. **5**(1): p. 1-25.

44. Mobed, P., S. Munusamy, D. Bhattacharyya and R. Rengaswamy, *State and Parameter Estimation in Distributed Constrained Systems. Part I: Extended Kalman Filtering of a Special Class of DAE Systems.* Industrial & Engineering Chemistry Research, 2016.

45. Sabet, M., A. Fathi and H.M. Daniali, *Optimal design of the Own Ship maneuver in the bearing-only target motion analysis problem using a heuristically supervised Extended Kalman Filter.* Ocean Engineering, 2016. **123**: p. 146-153.

46. Todoran, H.G. and M. Bader, *Extended Kalman Filter (EKF)-Based Local SLAM in Dynamic Environments: A Framework*, in *Advances in Robot Design and Intelligent Control*. 2016, Springer. p. 459-469.

47. Chatzi, E.N. and A.W. Smyth, *Nonlinear System Identification: Particle-Based Methods*, in *Encyclopedia of Earthquake Engineering*, M. Beer, I.A. Kougioumtzoglou, E. Patelli, and I.S.-K. Au, Editors. 2021, Springer Berlin Heidelberg: Berlin, Heidelberg. p. 1-18.

48. Chatzi, E.N. and A.W. Smyth, *Particle filter scheme with mutation for the estimation of time-invariant parameters in structural health monitoring applications.* Structural Control and Health Monitoring, 2013. **20**(7): p. 1081-1095.

49. Sarkka, S., *On unscented Kalman filtering for state estimation of continuous-time nonlinear systems.* IEEE Transactions on automatic control, 2007. **52**(9): p. 1631-1641.

50. Xie, Z. and J. Feng, *Real-time nonlinear structural system identification via iterated unscented Kalman filter.* Mechanical Systems and Signal Processing, 2012. **28**: p. 309-322.

51. Astroza, R., H. Ebrahimian and J.P. Conte, *Material Parameter Identification in Distributed Plasticity FE Models of Frame-Type Structures Using Nonlinear Stochastic Filtering.* Journal of Engineering Mechanics, 2015. **141**(5): p. 04014149.

52. Kontoroupi, T. and A.W. Smyth, *Online Noise Identification for Joint State and Parameter Estimation of Nonlinear Systems.* ASCE-ASME Journal of Risk and Uncertainty in Engineering Systems, Part A: Civil Engineering, 2016. **2**(3): p. B4015006.

53. Eftekhar Azam, S., E. Chatzi and C. Papadimitriou, *A dual Kalman filter approach for state estimation via output-only acceleration measurements.* Mechanical Systems and Signal Processing, 2015. **60-61**(Supplement C): p. 866-886.

54. Al-Hussein, A. and A. Haldar, *Novel unscented Kalman filter for health assessment of structural systems with unknown input.* Journal of Engineering Mechanics, 2015. **141**(7): p. 04015012.

55. Al-Hussein, A. and A. Haldar, *Unscented Kalman filter with unknown input and weighted global iteration for health assessment of large structural systems.* Structural Control and Health Monitoring, 2016. **23**(1): p. 156-175.

56. Azam, S.E., E. Chatzi and C. Papadimitriou, *A dual Kalman filter approach for state estimation via output-only acceleration measurements.* Mechanical Systems and Signal Processing, 2015. **60**: p. 866-886.

57. Azam, S.E., E. Chatzi, C. Papadimitriou and A. Smyth, *Experimental validation of the Kalman-type filters for online and real-time state and input estimation.* Journal of Vibration and Control, 2017. **23**(15): p. 2494-2519.

58. Cha, Y.J., J.G. Chen and O. Büyüköztürk, *Output-only computer vision based damage detection using phase-based optical flow and unscented Kalman filters.* Engineering Structures, 2017. **132**: p. 300-313.

59. Genz, A. and B.D. Keister, *Fully symmetric interpolatory rules for multiple integrals over infinite regions with Gaussian weight.* Journal of Computational and Applied Mathematics, 1996. **71**(2): p. 299-309.

60. Limongelli, M.P., E. Chatzi, M. Döhler, G. Lombaert and E. Reynders. *Towards extraction of vibration-based damage indicators*. in *EWSHM-8th European Workshop on Structural Health Monitoring*. 2016.

61. Magalhaes, F., A. Cunha and E. Caetano, *Online automatic identification of the modal parameters of a long span arch bridge.* Mechanical Systems and Signal Processing, 2009. **23**(2): p. 316-329.

62. Nyssen, F., B. Epureanu and J.C. Golinval, *Experimental modal identification of mistuning in an academic two-stage drum.* Mechanical Systems and Signal Processing, 2017. **88**: p. 428-444.

63. Lin, R.M., *Identification of modal parameters of unmeasured modes using multiple FRF modal analysis method.* Mechanical Systems and Signal Processing, 2011. **25**(1): p. 151-162.

64. Hermans, L. and H. Van der Auweraer, *Modal testing and analysis of structures under operational conditions: industrial applications.* Mechanical systems and signal processing, 1999. **13**(2): p. 193-216.

65. Maes, K., K.V. Nimmen, E. Lourens, A. Rezayat, P. Guillaume, G.D. Roeck, and G. Lombaert, *Verification of joint input-state estimation for force identification by means of in situ measurements on a footbridge.* Mechanical Systems and Signal Processing, 2016. **75**(Supplement C): p. 245-260.

66. Maes, K., A.W. Smyth, G. De Roeck and G. Lombaert, *Joint input-state estimation in structural dynamics.* Mechanical Systems and Signal Processing, 2016. **70-71**(Supplement C): p. 445-466.

67. Lourens, E., E. Reynders, G. De Roeck, G. Degrande and G. Lombaert, *An augmented Kalman filter for force identification in structural dynamics.* Mechanical Systems and Signal Processing, 2012. **27**: p. 446-460.

68. Moireau, P. and D. Chapelle, *Reduced-order Unscented Kalman Filtering with application to parameter identification in large-dimensional systems.* ESAIM: Control, Optimisation and Calculus of Variations, 2011. **17**(2): p. 380-405.

69. Sanchez, J. and H. Benaroya, *Review of force reconstruction techniques.* Journal of Sound and Vibration, 2014. **333**(14): p. 2999-3018.

70. Masjedian, M. and M. Keshmiri, *A review on operational modal analysis researches: classification of methods and applications.* J Proc. of the 3rd IOMAC, 2009: p. 707-718.

71. Allen, M.S., M.W. Sracic, S. Chauhan and M.H. Hansen, *Output-only modal analysis of linear time-periodic systems with application to wind turbine simulation data.* Mechanical Systems and Signal Processing, 2011. **25**(4): p. 1174-1191.

72. Erazo, K. and S. Nagarajaiah, *An offline approach for output-only Bayesian identification of stochastic nonlinear systems using unscented Kalman filtering.* Journal of Sound and Vibration, 2017. **397**: p. 222-240.

73. Chatzi, E.N. and A.W. Smyth, *The unscented Kalman filter and particle filter methods for nonlinear structural system identification with non-collocated heterogeneous sensing.* Structural Control and Health Monitoring: The Official Journal of the International Association for Structural Control and Monitoring and of the European Association for the Control of Structures, 2009. **16**(1): p. 99-123.

74. Adeli, H. and X. Jiang, *Intelligent infrastructure: neural networks, wavelets, and chaos theory for intelligent transportation systems and smart structures*. 2008: Crc Press.

75. Liu, A., L. Wang, L. Bornn and C. Farrar, *Robust structural health monitoring under environmental and operational uncertainty with switching state-space autoregressive models.* Structural Health Monitoring, 2018: p. 1475921718757721.

76. Padilla, L.E. and C.W. Rowley. *An adaptive-covariance-rank algorithm for the unscented Kalman filter*. in *Decision and Control (CDC), 2010 49th IEEE Conference on*. 2010. IEEE.

77. Ghorbani, E. and Y.-J. Cha, *An iterated cubature unscented Kalman filter for large-DoF systems identification with noisy data.* Journal of Sound and Vibration, 2018. **420**: p. 21-34.

78. Rao, S.S. and F.F. Yap, *Mechanical vibrations*. Vol. 4. 2011: Prentice Hall Upper Saddle River.

79. Brincker, R. *Application of the random decrement technique in operational modal analysis*.

80. Ewing, M. and H. Dande, *Panel Damping Loss Factor Estimation Using the Random Decrement Technique*, in *51st AIAA/ASME/ASCE/AHS/ASC Structures, Structural Dynamics, and Materials Conference*.

81. Ibrahim, S.R., J.C. Asmussen and R. Brincker, *Vector Triggering Random Decrement for High Identification Accuracy.* Journal of Vibration and Acoustics, 1998. **120**(4): p. 970-975.

82. James, G., T.G. Carne, J.P.J.M.A.-t.I.J.o.A. Lauffer and E.M. Analysis, *The natural excitation technique (NExT) for modal parameter extraction from operating structures.* 1995. **10**(4): p. 260.

83. Sim, S.-H., B. Spencer, H. Jo and J.F. Carbonell-Márquez. *Decentralized random decrement technique for data aggregation and system identification in wireless smart sensor networks*. in *IUTAM Symposium on Nonlinear Stochastic Dynamics and Control*. 2011. Springer.

84. Cha, Y.-J., J. Chen and O. Büyüköztürk, *Output-only computer vision based damage detection using phase-based optical flow and unscented Kalman filters.* Engineering Structures, 2017. **132**: p. 300-313.

85. Asayesh, M., B. Khodabandeloo and A. Siami, *A random decrement technique for operational modal analysis in the presence of periodic excitations.* Proceedings of the Institution of Mechanical Engineers, Part C: Journal of Mechanical Engineering Science, 2009. **223**(7): p. 1525-1534.

86. Modak, S., C. Rawal and T. Kundra, *Harmonics elimination algorithm for operational modal analysis using random decrement technique.* Mechanical Systems and Signal Processing, 2010. **24**(4): p. 922-944.

87. Wu, Y., D. Hu, M. Wu and X. Hu, *A numerical-integration perspective on Gaussian filters.* IEEE Transactions on Signal Processing, 2006. **54**(8): p. 2910-2921.

88. Foun, K., *Identification of civil structural parameters using the extended Kalman filter*. 2009, Massachusetts Institute of Technology.

89. Moaveni, B., X. He, J.P. Conte and J.I. Restrepo, *Damage identification study of a seven-story full-scale building slice tested on the UCSD-NEES shake table.* Structural Safety, 2010. **32**(5): p. 347-356.

90. Panagiotou, M., *Seismic design, testing and analysis of reinforced concrete wall buildings*. 2008, UC San Diego.

91. Moaveni, B., X. He, J.P. Conte, J.I. Restrepo and M. Panagiotou, *System identification study of a 7-story full-scale building slice tested on the UCSD-NEES shake table.* Journal of Structural Engineering, 2011. **137**(6): p. 705-717.

92. Moaveni, B., X. He, J.P. Conte, J.I. Restrepo and M. Panagiotou, *System identification study of a 7-story full-scale building slice tested on the UCSD-NEES shake table.* Journal of Structural Engineering, 2010. **137**(6): p. 705-717.

93. Van Overschee, P. and B. De Moor, *Subspace identification for linear systems: Theory—Implementation—Applications*. 2012: Springer Science & Business Media.

94. He, X., B. Moaveni, J.P. Conte, A. Elgamal and S.F.J.J.o.S.E. Masri, *System identification of Alfred Zampa Memorial Bridge using dynamic field test data.* Structural Engineering, 2009. **135**(1): p. 54-66.

95. Akhlaghi, S., N. Zhou and Z. Huang. *Adaptive adjustment of noise covariance in Kalman filter for dynamic state estimation*. in *IEEE Power & Energy Society General Meeting*. 2017. IEEE.

96. Ghorbani, E., O. Buyukozturk and Y.-J. Cha, *Hybrid output-only structural system identification using random decrement and Kalman filter.* Mechanical Systems and Signal Processing, 2020. **144**: p. 106977.

97. Ghorbani, E. and Y.-J. Cha. *Identification of large-scale systems with noisy data using an iterated cubature unscented Kalman filter*. in *Sensors and Smart Structures Technologies for Civil, Mechanical, and Aerospace Systems 2018*. 2018. International Society for Optics and Photonics.

98. Cha, Y.-J., J.G. Chen and O. Büyüköztürk, *Motion magnification based damage detection using high speed video.* Structural Health Monitoring 2015, 2015.

99. Zarafshan, A., A. Iranmanesh and F. Ansari, *Vibration-based method and sensor for monitoring of bridge scour.* Journal of bridge engineering, 2012. **17**(6): p. 829-838.

100. Deng, L. and C. Cai, *Bridge scour: Prediction, modeling, monitoring, and countermeasures.* Practice periodical on structural design and construction, 2010. **15**(2): p. 125-134.

101. Briaud, J.-L., S. Hurlebaus, K.-A. Chang, C. Yao, H. Sharma, O.-Y. Yu, C. Darby, B.E. Hunt, and G.R. Price, *Realtime monitoring of bridge scour using remote monitoring technology*. 2011, Texas Transportation Institute.

102. Yu, X. and X. Yu, *Time domain reflectometry automatic bridge scour measurement system: principles and potentials.* Structural Health Monitoring, 2009. **8**(6): p. 463-476.

103. Azhari, F. and K.J. Loh, *Laboratory validation of buried piezoelectric scour sensing rods.* Structural Control and Health Monitoring, 2017. **24**(9): p. e1969.

104. Hunt, B.E., *Monitoring scour critical bridges*. Vol. 396. 2009: Transportation Research Board.

105. Lin, Y.B., J.S. Lai, K.C. Chang and L.S. Li, *Flood scour monitoring system using fiber Bragg grating sensors.* Smart materials and Structures, 2006. **15**(6): p. 1950.

106. Wang, C.-Y., H.-L. Wang and C.-C. Ho, *A Piezoelectric Film Type Scour Monitoring System for Bridge Pier.* Advances in Structural Engineering, 2012. **15**(6): p. 897-905.

107. Anderson, N.L., A.M. Ismael and T. Thitimakorn, *Ground-penetrating radar: a tool for monitoring bridge scour.* Environmental and Engineering Geoscience, 2007. **13**(1): p. 1-10.

108. Michalis, P., A. Tarantino, C. Tachtatzis and M.D. Judd, *Wireless monitoring of scour and re-deposited sediment evolution at bridge foundations based on soil electromagnetic properties.* Smart Materials and Structures, 2015. **24**(12): p. 125029.

109. Maroni, A., E. Tubaldi, N. Ferguson, A. Tarantino, H. McDonald, and D. Zonta, *Electromagnetic sensors for underwater scour monitoring.* Sensors, 2020. **20**(15): p. 4096.

110. Tritech. *Available online: https://www.tritech.co.uk/media/case-studies/bridgecat-bridge-inspection-with.pdf*. May 2019.

111. RAIB, *Structural failure caused by scour at Lamington viaduct, South Lanarkshire 31 December 2015*. 2016, Rail Accident Investigation Branch, Department for Transport: Derby, UK.

112. Bao, T. and Z. Liu, *Vibration-based bridge scour detection: a review.* Structural Control and Health Monitoring, 2017. **24**(7): p. e1937.

113. Fisher, M., S. Atamturktur and A.A. Khan, *A novel vibration-based monitoring technique for bridge pier and abutment scour*. Structural health monitoring, 2013. **12**(2): p. 114-125.

114. Foti, S. and D. Sabia, *Influence of Foundation Scour on the Dynamic Response of an Existing Bridge.* Journal of Bridge Engineering, 2011. **16**(2): p. 295-304.

115. Prendergast, L.J. and K. Gavin, *A review of bridge scour monitoring techniques.* Journal of Rock Mechanics and Geotechnical Engineering, 2014. **6**(2): p. 138-149.

116. Prendergast, L.J., D. Hester, K. Gavin and J.J. O'Sullivan, *An investigation of the changes in the natural frequency of a pile affected by scour.* Journal of Sound and Vibration, 2013. **332**(25): p. 6685-6702.

117. Elsaid, A. and R. Seracino, *Rapid assessment of foundation scour using the dynamic features of bridge superstructure.* Construction and Building Materials, 2014. **50**: p. 42-49.

118. Prendergast, L.J., D. Hester and K.J.J.o.B.E. Gavin, *Determining the presence of scour around bridge foundations using vehicle-induced vibrations.* 2016. **21**(10): p. 04016065.

119. Wu, W., L. Prendergast and K. Gavin, *An iterative method to infer distributed mass and stiffness profiles for use in reference dynamic beam-Winkler models of*

foundation piles from frequency response functions. Journal of Sound and Vibration, 2018. **431**: p. 1-19.

120. Xiong, W., C. Cai, B. Kong, P. Tang and J. Ye, *Identification of bridge scour depth by tracing dynamic behaviors of superstructures.* KSCE Journal of Civil Engineering, 2018. **22**(4): p. 1316-1327.

121. Fan, W. and P. Qiao, *Vibration-based Damage Identification Methods: A Review and Comparative Study.* Structural Health Monitoring, 2011. **10**(1): p. 83-111.

122. Choudhury, M.S.I., Y. Matsumoto and A.F.M.S. Amin, *Scour depth estimation in a balanced cantilever bridge with deteriorated central hinges based on natural frequencies: field measurements, methodology for estimation and verification.* Journal of Civil Structural Health Monitoring, 2018. **8**(4): p. 617-634.

123. Palanisamy, R.P. and S.-H. Sim. *Bridge scour monitoring using extended Kalman filter*. in *6th International Conference on Advances in Experimental Structural Engineering, 11th International Workshop on Advanced Smart Material and Smart Structures Technology*. 2015.

124. Brincker, R. and J. Rodrigues. *Application of the random decrement technique in operational modal analysis*. in *Proceedings of the 1st International Operational Modal Analysis Conference (IOMAC), Aalborg Universitet, Aalborg, Denmark*. 2005.

125. Ibrahim, S., *Random decrement technique for modal identification of structures.* Journal of Spacecraft and Rockets, 1977. **14**(11): p. 696-700.

126. Meirovitch, L., *Fundamentals of vibrations*. 2010: Waveland Press.

127. Cha, P.D. and T. Ha Park, *Improved modal convergence using the assumed modes method for rods carrying various lumped elements.* International Journal of Mechanical Engineering Education, 2018. **46**(1): p. 3-30.

128. Welch, G. and G. Bishop, *An introduction to the Kalman filter*. 1995, Citeseer.

129. Hoshiya, M. and E. Saito, *Structural identification by extended Kalman filter*. Journal of engineering mechanics, 1984. **110**(12): p. 1757-1770.

130. Wu, M. and A.W. Smyth, *Application of the unscented Kalman filter for real-time nonlinear structural system identification.* Structural Control and Health Monitoring: The Official Journal of the International Association for Structural Control and Monitoring and of the European Association for the Control of Structures, 2007. **14**(7): p. 971-990.

131. Cha, Y.-J., J.G. Chen and O. Büyüköztürk, *Output-only computer vision based damage detection using phase-based optical flow and unscented Kalman filters.* Engineering Structures, 2017. **132**: p. 300-313.

132. MATLAB, *version 9.5.0 (R2018b)*. 2018, Natick, Massachusetts: The MathWorks Inc.

133. Pan, Y., A.K. Agrawal, M. Ghosn and S. Alampalli, *Seismic fragility of multispan simply supported steel highway bridges in New York State. I: Bridge modeling, parametric analysis, and retrofit design.* Journal of Bridge Engineering, 2010. **15**(5): p. 448-461.

134. API, *Recommended practice for planning, designing and constructing offshore platforms—Working stress design.*, in *API Offshore Structure Standards Set*. API RP 2A-WSD (2014): Washington, DC. p. 310.

135. Prendergast, L.J., K. Gavin and D. Hester, *Isolating the location of scour-induced stiffness loss in bridges using local modal behaviour.* Journal of Civil Structural Health Monitoring, 2017. **7**(4): p. 483-503.

136. Karbhari, V. and D. Eckel, *Effect of cold regions climate on composite jacketed concrete columns.* Journal of cold regions engineering, 1994. **8**(3): p. 73-86.

137. Gonzales, I., M. Ülker-Kaustell and R. Karoumi, *Seasonal effects on the stiffness properties of a ballasted railway bridge.* Engineering structures, 2013. **57**: p. 63-72.

138. Véronneau, M. and J. Huang, *The Canadian Geodetic Vertical Datum of 2013 (CGVD2013).* GEOMATICA, 2016. **70**(1): p. 9-19.

Appendix A

The initial values and tuning parameters for the 10 DoF system are as follows:

Initial values: $\left[\mathbf{X} \quad \dot{\mathbf{X}} \quad \mathbf{K} \quad \mathbf{C}\right]$

$\mathbf{X} = \text{zeros}\,(10,1),\ \dot{\mathbf{X}} = \text{zeros}\,(10,1)$

$\mathbf{K} = 30000 \times \text{ones}\,(10,1)$, $\mathbf{C} = 200 \times \text{ones}\ (10,1)$

Initial state covariance matrix for the UKF: $\text{diag}\left[\mathbf{P}_{\text{x}} \quad \mathbf{P}_{\dot{\text{x}}} \quad \mathbf{P}_{\text{k}} \quad \mathbf{P}_{\text{c}}\right]$

Initial state covariance matrix for the CKF: $\text{diag}\left[\mathbf{P}_{\text{x}} \quad \mathbf{P}_{\dot{\text{x}}} \quad \mathbf{P}_{\text{k}} \quad \mathbf{P}_{\text{c}}\right]$

$\mathbf{P}_{\text{x}} = \mathbf{P}_{\dot{\text{x}}} = \text{ones}\ (10,1)$

$\mathbf{P}_{\text{k}} = \mathbf{P}_{\text{c}} = 10^{7} \times \text{ones}\ (10,1)$

Initial states covariance matric for the IMUKF: $\text{diag}\left[\mathbf{P}'_{\text{x}} \quad \mathbf{P}'_{\dot{\text{x}}} \quad \mathbf{P}'_{\text{k}} \quad \mathbf{P}'_{\text{c}}\right]$

$\mathbf{P}'_{\text{x}} = \mathbf{P}'_{\dot{\text{x}}} = \text{ones}\ (10,1)$

$\mathbf{P}'_{\text{k}} = 10^{9} \times \text{ones}\ (10,1)$, $\mathbf{P}'_{\text{c}} = 10^{7} \times \text{ones}\ (10,1)$

Constant parameters:

Process noise covariance: $10^{-14}\ \mathbf{I}_{40}$

Measurement noise covariance: $10^{-2}\ \mathbf{I}_{3}$

UKF: scaling parameter $(\gamma) = 0$

IMUKF: $\gamma_1 = 3$ and $\gamma_2 = -5$

Number of iterations= 80

Reduce rate $(\eta) = 0.04$

Appendix B

In order to promote better understanding of the mathematical meaning of the RD method, the dynamic motion equation of a linear *l*-DoF system with stationary random zero-mean excitation is reintroduced:

$$[\mathbf{M}]\{\ddot{\mathbf{X}}(t)\}+[\mathbf{C}]\{\ddot{\mathbf{X}}(t)\}+[\mathbf{K}]\{\mathbf{X}(t)\}=\{\mathbf{f}(t)\}\,, \tag{B-1}$$

where **M**, **C**, **K**, and **f** are the mass, damping, stiffness, and external force matrices, respectively, and t, **X**, $\dot{\mathbf{X}}$, and $\ddot{\mathbf{X}}$ are also time, displacement, velocity, and acceleration vectors, respectively. We define an operator $\tilde{p}_{ij}$ as:

$$\tilde{p}_{ij}(x)=m_{ij}\frac{d^2x_j}{dt^2}+c_{ij}\frac{dx_j}{dt}+k_{ij}x_j\,, \tag{B-2}$$

where i, and j both start from 1 to number of DoF, and m_{ij}, c_{ij}, and k_{ij} are components of the mass, damping, and stiffness matrices, respectively. Using this operator, the Eq.B-1 is rearranged as:

$$\begin{bmatrix}\tilde{p}_{11} & \tilde{p}_{12} & \cdots & \tilde{p}_{1l}\\ \tilde{p}_{21} & \tilde{p}_{22} & \cdots & \tilde{p}_{2l}\\ \vdots & \vdots & \vdots & \vdots\\ \tilde{p}_{l1} & \tilde{p}_{l2} & \cdots & \tilde{p}_{ll}\end{bmatrix}\begin{Bmatrix}x_1\\ x_2\\ \vdots\\ x_l\end{Bmatrix}=\begin{Bmatrix}f_1\\ f_2\\ \vdots\\ f_l\end{Bmatrix}\,, \tag{B-3}$$

where f_j is a component of the force vector.

In systems with more than one DoF, users have to define a trigger point for the response of one specific DoF. Based on this specific DoF response within a system and the defined trigger point, the segments for all the other responses of the system will be automatically extracted without considering whether the other responses reach the trigger point or not. Since the trigger point was applied to only one specific response, an equal number of segments from all responses will be extracted. An averaging of all the *N* segments of all the DoFs will form:

$$\frac{1}{N}\sum_{r=1}^{N}\begin{bmatrix}\tilde{p}_{11} & \tilde{p}_{12} & \cdots & \tilde{p}_{1l}\\ \tilde{p}_{21} & \tilde{p}_{22} & \cdots & \tilde{p}_{2l}\\ \vdots & \vdots & \vdots & \vdots\\ \tilde{p}_{l1} & \tilde{p}_{l2} & \cdots & \tilde{p}_{ll}\end{bmatrix}\begin{Bmatrix}x_{1r}(\tau)\\ x_{2r}(\tau)\\ \vdots\\ x_{lr}(\tau)\end{Bmatrix}=\frac{1}{N}\sum_{r=1}^{N}\begin{Bmatrix}f_{1r}(\tau)\\ f_{2r}(\tau)\\ \vdots\\ f_{lr}(\tau)\end{Bmatrix}, \tag{B-4}$$

The right-hand side of Eq. B-4 is equal to zero because the force is a random zero-mean signal. For the left-hand side of the equation, the operator and summation can swap. Then, based on what has heretofore been explained, what remains is the free vibration response of the system by an initial virtual displacement as described below:

$$\begin{bmatrix}\tilde{p}_{11} & \tilde{p}_{12} & \cdots & \tilde{p}_{1l}\\ \tilde{p}_{21} & \tilde{p}_{22} & \cdots & \tilde{p}_{2l}\\ \vdots & \vdots & \vdots & \vdots\\ \tilde{p}_{l1} & \tilde{p}_{l2} & \cdots & \tilde{p}_{ll}\end{bmatrix}\begin{Bmatrix}\boldsymbol{\delta}_1(\tau)\\ \boldsymbol{\delta}_2(\tau)\\ \vdots\\ \boldsymbol{\delta}_l(\tau)\end{Bmatrix}=\begin{Bmatrix}0\\ 0\\ \vdots\\ 0\end{Bmatrix}. \tag{B-5}$$

The Eq. B-5 shows that $\boldsymbol{\delta}_j(\tau)(j=1,2,\ldots,l)$ is the free response of the system due to initial virtual displacement.

Appendix C

The free vibration response of each floor under different damage scenarios (D1-D4) are shown here.

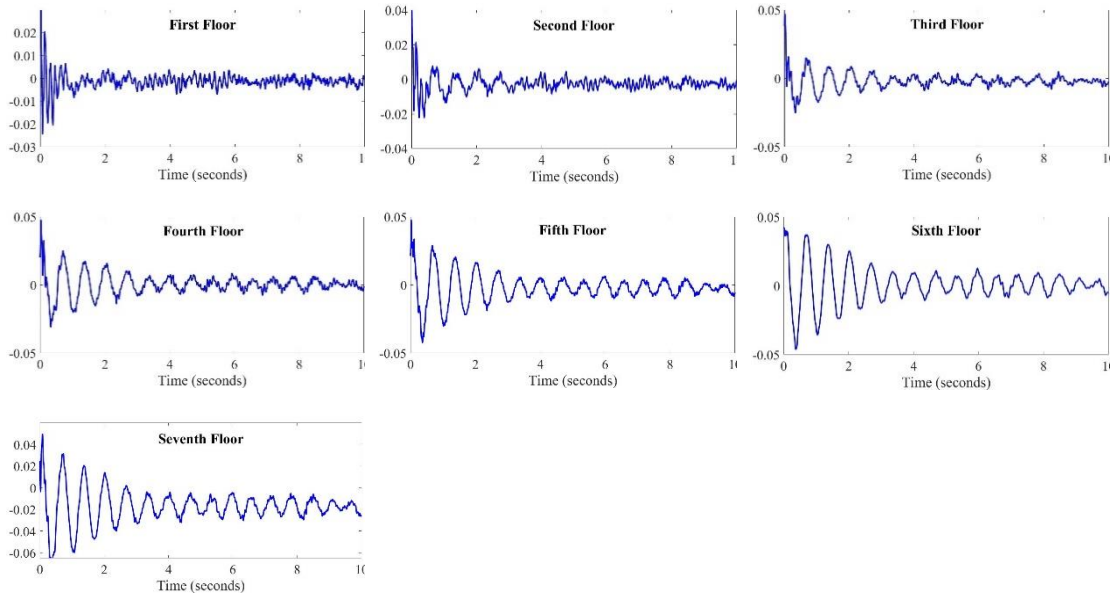

Figure C-1: The free vibration response of the building within the damage state one (D1)

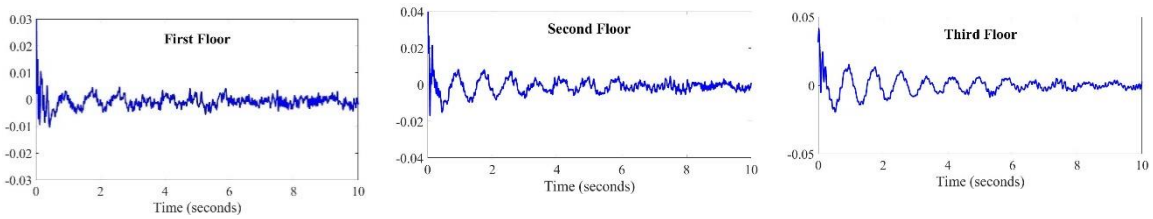

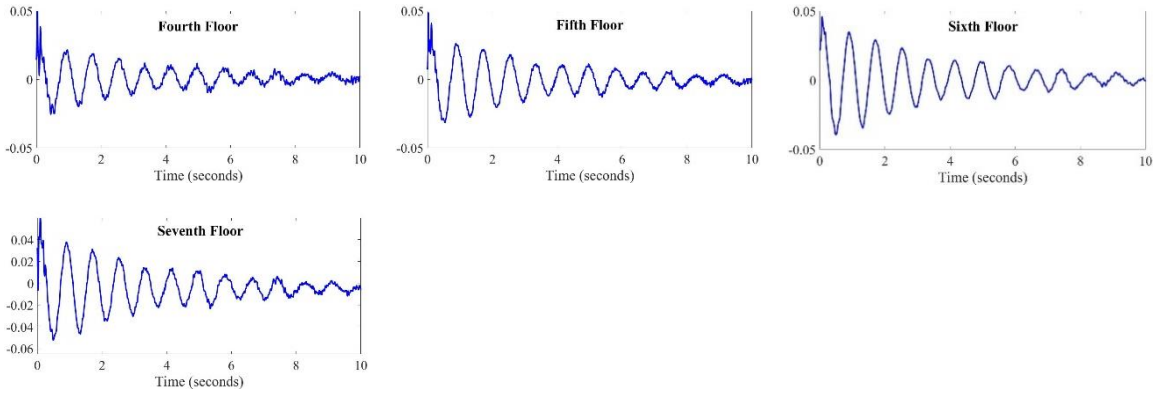

Figure C-2: The free vibration response of the building within the damage state two (D2)

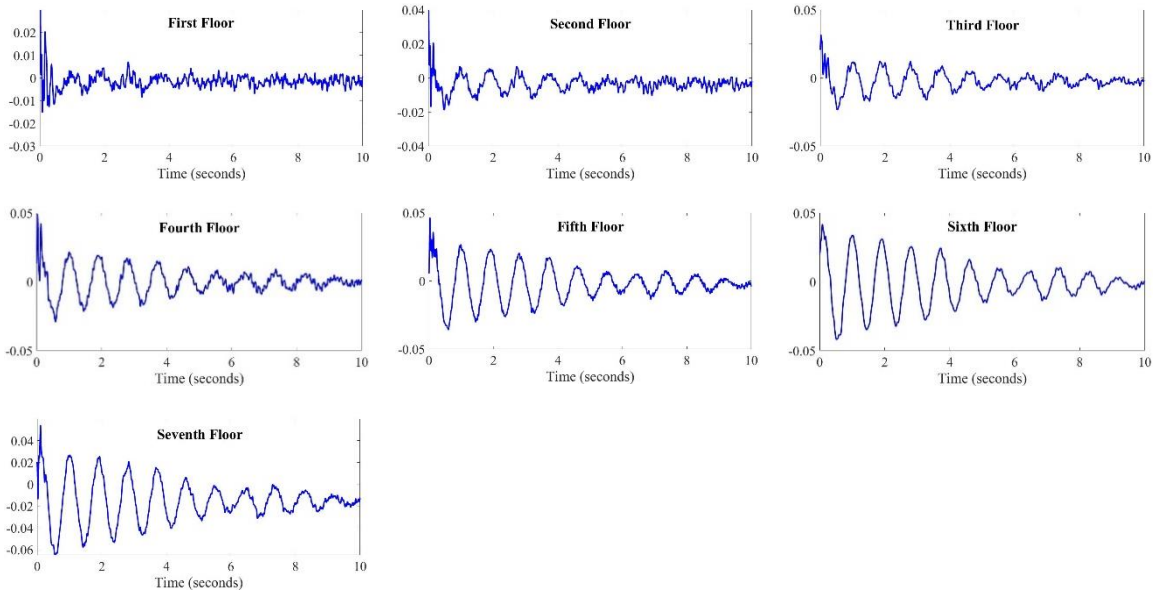

Figure C-3: The free vibration response of the building within the damage state three (D3-1)

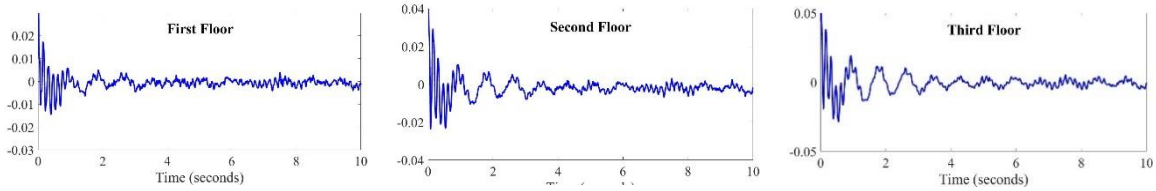

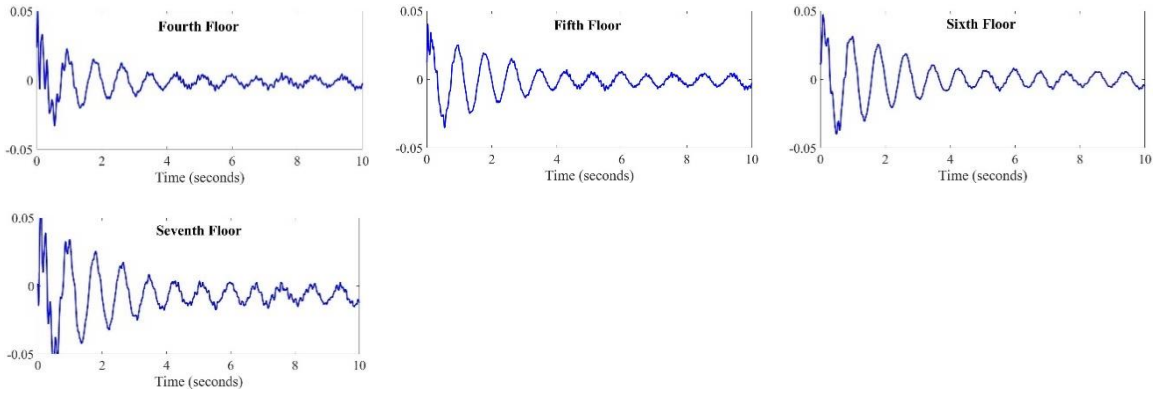

Figure C-4: The free vibration response of the building within the damage state four (D3-2)

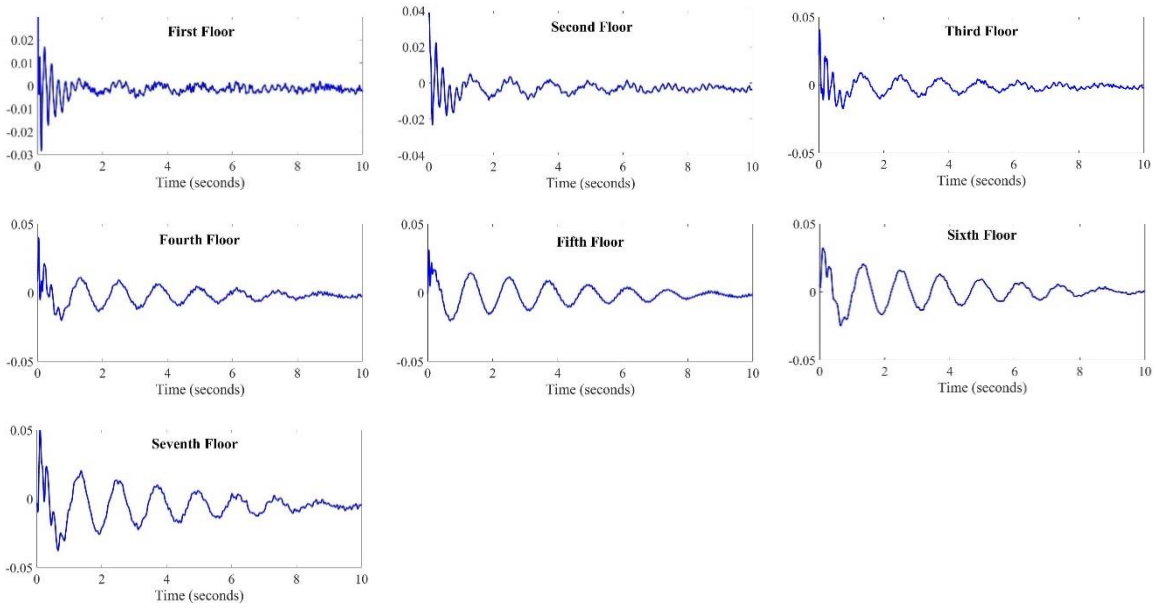

Figure C-5: The free vibration response of the building within the damage state five (D4)

Appendix D

The partial differential equation of a Euler beam under external excitation presents by:

$$EI\frac{\partial^4\omega(x,t)}{\partial x^4}+\rho A\frac{\partial^2\omega(x,t)}{\partial t^2}+P\frac{\partial^2\omega(x,t)}{\partial x^2}=F(x,t), \tag{D.1}$$

where the external force is:

$$\begin{aligned}F(x,t)&=f_{water}(x,t)[H(x-a)-H(x-b)]\\&-k_s\omega(x,t)[H(x)-H(x-a)]-c_s\frac{\partial\omega(x,t)}{\partial t}[H(x)-H(x-a)]\\&-k_b\omega(x,t)\delta(x-L)-c_b\frac{\partial\omega(x,t)}{\partial t}\delta(x-L)-M_D\frac{\partial^2\omega(x,t)}{\partial t^2}\delta(x-L).\end{aligned} \tag{D.2}$$

In order to solve a continuous model, different techniques are mentioned in advance vibration books [126]. In this study, the assumed mode method is used to solve the equation. Based on the assumed mode approach,

$$\omega(x,t)=\sum_{n=1}^{N}X_n(x)q_n(t), \tag{D.3}$$

$X_n(x)$: is an admissible function

$q_n(t)$: is s generalized coordinate

By substituting Eq. (D.3) into Eq. (D.2) and Eq. (D.1), and rewriting the equation:

$$
\begin{aligned}
&EI(\sum_{n=1}^{N}\frac{d^4X_n(x)}{dx^4}q_n(t)) + \rho A(\sum_{n=1}^{N}X_n(x)\frac{d^2q_n(t)}{dt^2}) + P(\sum_{n=1}^{N}\frac{d^2X_n(x)}{dx^2}q_n(t)) \\
&+k_s(\sum_{n=1}^{N}X_n(x)q_n(t))[H(x)-H(x-a)] + c_s(\sum_{n=1}^{N}\frac{dq_n(t)}{dt}X_n(x))[H(x)-H(x-a)] \\
&+k_b(\sum_{n=1}^{N}X_n(x)q_n(t))\delta(x-L) + c_b(\sum_{n=1}^{N}\frac{q_n(t)}{dt}X_n(x))\delta(x-L) \\
&+M_D(\sum_{n=1}^{N}\frac{q^2{}_n(t)}{dt^2}X_n(x))\delta(x-L) = f_{water}(x,t)[H(x-a)-H(x-b)].
\end{aligned}
\tag{D.4}
$$

Considering the orthogonality of the mode shapes $\int X_n(x)X_m(x)dx = \delta_{nm}$ while: $\delta_{nm} = \begin{cases} 1 & n = m \\ 0 & n \neq m \end{cases}$, both sides of the Eq (D.4) are multiplied to $X_m(x)$ and integrate the whole equation over the length of the beam $\int_0^L dx$

$$
\begin{aligned}
&\int_0^L (EI\sum_{n=1}^{N}X_m(x)X^4_{\ n}(x)q_n(t))dx + \int_0^L (\rho A\sum_{n=1}^{N}X_m(x)X_n(x)\ddot{q}_n(t))dx \\
&+P\int_0^L (\sum_{n=1}^{N}X_m(x)X''_n(x)q_n(t))dx \\
&+\int_0^L k_s(\sum_{n=1}^{N}X_n(x)X_m(x)q_n(t))[H(x)-H(x-a)]dx + \int_0^L k_b(\sum_{n=1}^{N}X_n(x)X_m(x)q_n(t))\delta(x-l)dx \\
&+\int_0^L c_s(\sum_{n=1}^{N}X_n(x)X_m(x)\dot{q}_n(t))[H(x)-H(x-a)]dx + \int_0^L c_b(\sum_{n=1}^{N}X_n(x)X_m(x)\dot{q}_n(t))\delta(x-l)dx \\
&+\int_0^L (M_D\sum_{n=1}^{N}X_m(x)X_n(x)\ddot{q}_n(t))\delta(x-l)dx = \int_0^L f_{water}(x,t)X_m(x)[H(x-a)-H(x-b)]dx,
\end{aligned}
\tag{D.5}
$$

Rearranging the equation:

$$
\begin{aligned}
&EI\sum_{n=1}^{N} q_n(t)\int_0^L X_m(x)X_n^4(x)dx) + \rho A\sum_{n=1}^{N}\ddot{q}_n(t)\int_0^L X_m(x)X_n(x)dx \\
&+ P\sum_{n=1}^{N} q_n(t)\int_0^L X_m(x)X_n''(x)dx + k_s\sum_{n=1}^{N} q_n(t)\int_0^L X_n(x)X_m(x)[H(x)-H(x-a)]dx \\
&+ c_s\dot{q}_n(t)(\sum_{n=1}^{N}\int_0^L X_n(x)X_m(x)[H(x)-H(x-a)]dx + k_b q_n(t)\int_0^L(\sum_{n=1}^{N} X_n(x)X_m(x))\delta(x-l)dx \\
&+ c_b\dot{q}_n(t)\int_0^L(\sum_{n=1}^{N} X_n(x)X_m(x))\delta(x-l)dx + M_D\ddot{q}_n(t)\int_0^L(\sum_{n=1}^{N} X_m(x)X_n(x))\delta(x-l)dx \\
&= \int_0^L f_{water}(x,t)X_m(x)[H(x-a)-H(x-b)]dx,
\end{aligned}
\tag{D.6}
$$

where H is Heaviside function: $H(x-a)=\begin{cases}1 & x\ge a\\ 0 & x<a\end{cases}$, then: $\int_0^L f(x)H(x-a)dx=\int_a^L f(x)dx$. Based on the mode shapes orthogonality, each component will be nonzero, when $m=n$, then the summation will disappear, and will have:

$$
\begin{aligned}
&EI[\int_0^L X_m(x)X_n^4(x)dx]q_n(t) + \rho A[\int_0^L X_m(x)X_n(x)dx]\ddot{q}_n(t) \\
&+ P[\int_0^L X_m(x)X_n''(x)dx]q_n(t) + k_s[\int_0^a X_n(x)X_m(x)\,dx]q_n(t) \\
&+ c_s[\int_0^a X_n(x)X_m(x)dx]\dot{q}_n(t) + k_b[\int_0^L X_n(x)X_m(x)\delta(x-L)\,dx]q_n(t) \\
&+ c_b[\int_0^L X_n(x)X_m(x)\delta(x-L)dx]\dot{q}_n(t) + M_D[\int_0^L X_m(x)X_n(x)\delta(x-L)dx]\ddot{q}_n(t) \\
&= \int_a^b f_{water}(x,t)X_m(x)\,dx.
\end{aligned}
\tag{D.7}
$$

Defining some constant values:

$$
\begin{aligned}
&V_{mn} = \int_0^L X_m(x)X_n^4(x)dx, \quad B_{mn} = \int_0^L X_m(x)X_n(x)dx, \\
&Q_{mn} = \int_0^L X_m(x)X_n''(x)dx, \quad D_{nm} = \int_0^a X_n(x)X_m(x)\,dx.
\end{aligned}
\tag{D.8}
$$

The equation can be written as below:

$$\begin{aligned} &EI\,V_{mn}\,q_n(t)+\rho B_{mn}\,\ddot{q}_n(t)+PQ_{mn}\,q_n(t)+k_s\,D_{nm}\;q_n(t)+c_s\,D_{nm}\;\dot{q}_n(t)\\ &+k_b\,X^2{}_m(x=L)q_n(t)+c_b\,X^2{}_m(x=L)\dot{q}_n(t)+M_D\,X^2{}_m(x=L)\ddot{q}_n(t)\\ &=\int_a^b f_{water}(x,t)X_m(x)\,dx, \end{aligned} \tag{D.9}$$

and rearranged as:

$$\begin{aligned} &(\rho A\,B_{mn}+M_D\,X^2{}_m(x=L))\ddot{q}_n(t)+(c_s\,D_{nm}+c_b\,X^2{}_m(x=L))\;\dot{q}_n(t)\\ &+[EI\,V_{mn}\;+PQ_{mn}\;+k_s\,D_{nm}+k_b\,X^2{}_m(x=L)]q_n(t)=\int_a^b f_{water}(x,t)X_m(x)\,dx. \end{aligned} \tag{D.10}$$

The following equation has the form of a standard vibrating equation and can be transformed to state-space domain for Kalman filtering estimation purposes.

$$M_{mn}\ddot{q}_n(t)+C_{mn}\dot{q}_n(t)+K_{mn}q_n(t)=F_m(t)$$

$$\begin{aligned} M_{mn}&=\rho A\,B_{mn}+M_D\,X^2{}_m(x=L)\\ C_{mn}&=c_s\,D_{nm}+c_b\,X^2{}_m(x=L)\\ K_{mn}&=EI\,V_{mn}\;+PQ_{mn}\;+k_s\,D_{nm}+k_b\,X^2{}_m(x=L)\\ F_m(t)&=\int_a^b f_{water}(x,t)X_m(x)\,dx \end{aligned} \tag{D.11}$$

Appendix E

The new form of Eq. (6.23) and Eq. (6.24) are rearranged as follows. $f_{k_s}(x_7)$ and $f_{c_s}(x_7)$ define the soil stiffness and damping functions as dependent on the soil height.

$$\mathbf{x}_{k+1|k} = \begin{bmatrix} x_1 + \Delta t\, x_4, \\ x_2 + \Delta t\, x_5, \\ x_3 + \Delta t\, x_6, \\ x_4 + \frac{\Delta t}{M_{11}}[-(f_{c_s}(x_7)D_{11} + \tilde{C}_{11})x_4 - (f_{c_s}(x_7)D_{12} + \tilde{C}_{12})x_5 - (f_{c_s}(x_7)D_{13} + \tilde{C}_{13})x_6 \\ -(\tilde{K}_{11} + D_{11} f_{k_s}(x_7))x_1 - (\tilde{K}_{12} + D_{12} f_{k_s}(x_7))x_2 - (\tilde{K}_{13} + D_{13} f_{k_s}(x_7))x_3], \\ x_5 + \frac{\Delta t}{M_{22}}[-(f_{c_s}(x_7)D_{21} + \tilde{C}_{21})x_4 - (f_{c_s}(x_7)D_{22} + \tilde{C}_{22})x_5 - (f_{c_s}(x_7)D_{23} + \tilde{C}_{23})x_6 \\ -(\tilde{K}_{21} + D_{21} f_{k_s}(x_7))x_1 - (\tilde{K}_{22} + D_{22} f_{k_s}(x_7))x_2 - (\tilde{K}_{23} + D_{23} f_{k_s}(x_7))x_3], \\ x_6 + \frac{\Delta t}{M_{33}}[-(f_{c_s}(x_7)D_{31} + \tilde{C}_{31})x_4 - (f_{c_s}(x_7)D_{32} + \tilde{C}_{32})x_5 - (f_{c_s}(x_7)D_{33} + \tilde{C}_{33})x_6 \\ -(\tilde{K}_{31} + D_{31} f_{k_s}(x_7))x_1 - (\tilde{K}_{32} + D_{32} f_{k_s}(x_7))x_2 - (\tilde{K}_{33} + D_{33} f_{k_s}(x_7))x_3], \\ x_7 \end{bmatrix} \tag{E.1}$$

$$= F(\mathbf{X}_k, \Delta t),$$

$$
\mathbf{Y}_k = \begin{bmatrix}
\frac{1}{M_{11}}[-(f_{c_s}(x_7)D_{11}+\tilde{C}_{11})x_4-(f_{c_s}(x_7)D_{12}+\tilde{C}_{12})x_5-(f_{c_s}(x_7)D_{13}+\tilde{C}_{13})x_6 \\
-(\tilde{K}_{11}+D_{11}f_{k_s}(x_7))x_1-(\tilde{K}_{12}+D_{12}f_{k_s}(x_7))x_2-(\tilde{K}_{13}+D_{13}f_{k_s}(x_7))x_3], \\
\frac{1}{M_{22}}[-(f_{c_s}(x_7)D_{21}+\tilde{C}_{21})x_4-(f_{c_s}(x_7)D_{22}+\tilde{C}_{22})x_5-(f_{c_s}(x_7)D_{23}+\tilde{C}_{23})x_6 \\
-(\tilde{K}_{21}+D_{21}f_{k_s}(x_7))x_1-(\tilde{K}_{22}+D_{22}f_{k_s}(x_7))x_2-(\tilde{K}_{23}+D_{23}f_{k_s}(x_7))x_3], \\
\frac{1}{M_{33}}[-(f_{c_s}(x_7)D_{31}+\tilde{C}_{31})x_4-(f_{c_s}(x_7)D_{32}+\tilde{C}_{32})x_5-(f_{c_s}(x_7)D_{33}+\tilde{C}_{33})x_6 \\
-(\tilde{K}_{31}+D_{31}f_{k_s}(x_7))x_1-(\tilde{K}_{32}+D_{32}f_{k_s}(x_7))x_2-(\tilde{K}_{33}+D_{33}f_{k_s}(x_7))x_3]
\end{bmatrix} \qquad \text{(E.2)}
$$

$$
= H(\mathbf{X}_{k+1|k}, \Delta t).
$$